

TEMPERATURE ESTIMATION USING MAGNETIC NANOPARTICLES:
A SIMULATION STUDY

A THESIS SUBMITTED TO
THE GRADUATE SCHOOL OF NATURAL AND APPLIED SCIENCES
OF
MIDDLE EAST TECHNICAL UNIVERSITY

BY

GAMZE ONUKER

IN PARTIAL FULFILLMENT OF THE REQUIREMENTS
FOR
THE DEGREE OF MASTER OF SCIENCE
IN
ELECTRICAL AND ELECTRONICS ENG.

DECEMBER 2019

Approval of the thesis:

**TEMPERATURE ESTIMATION USING MAGNETIC NANOPARTICLES:
A SIMULATION STUDY**

submitted by **GAMZE ONUKER** in partial fulfillment of the requirements for the degree of **Master of Science in Electrical and Electronics Eng. Department, Middle East Technical University** by,

Prof. Dr. Halil Kalıpçılar
Dean, Graduate School of **Natural and Applied Sciences**

Prof. Dr. İlkay Ulusoy
Head of Department, **Electrical and Electronics Eng.**

Prof. Dr. Nevzat G. Gençer
Supervisor, **Electrical and Electronics Engineering, METU**

Dr. Can Barış Top
Co-supervisor, **ASELSAN Research Center, ASELSAN A.Ş**

Examining Committee Members:

Prof. Dr. Murat Eyüboğlu
Electrical and Electronics Engineering, METU

Prof. Dr. Nevzat G. Gençer
Electrical and Electronics Engineering, METU

Prof. Dr. İlkay Ulusoy
Electrical and Electronics Engineering, METU

Assoc. Prof. Dr. Yeşim Serinağaoğlu
Electrical and Electronics Engineering, METU

Assist. Prof. Dr. Emine Ülkü Sarıtaş
Electrical and Electronics Engineering, Bilkent University

Date: 26.12.2019

I hereby declare that all information in this document has been obtained and presented in accordance with academic rules and ethical conduct. I also declare that, as required by these rules and conduct, I have fully cited and referenced all material and results that are not original to this work.

Name, Last Name: GAMZE ONUKER

Signature :

ABSTRACT

TEMPERATURE ESTIMATION USING MAGNETIC NANOPARTICLES: A SIMULATION STUDY

Onuker, Gamze

M.S., Department of Electrical and Electronics Eng.

Supervisor : Prof. Dr. Nevzat G. Gençer

Co-Supervisor : Dr. Can Barış Top

December 2019, 97 pages

Lately, in biomedical imaging systems, algorithms for providing the temperature data became more important both for diagnosis and for treatment. Aiming to serve this purpose, in this thesis study, it is planned to estimate the temperature data using magnetic nanoparticles; which are actually imaging tracers used in a new medical imaging modality, Magnetic Particle Imaging (MPI). Since the introduction of MPI, the effect of temperature changes on magnetic nanoparticles (MNPs) and their magnetic behavior, is being investigated and the results show that there is a non-linear relation between the temperature and the particle magnetization. For this reason, as the starting point of this study, a detailed MPI system was modelled using MATLAB with its main components, which are the Selection Field, Drive Field and Receiver coil pairs. All coils were modelled to have a circular shape, the Selection and Drive field coils have 25cm radius whereas the receive coils have 10cm radius. Scanning sequence was chosen to be 'Lissajous Trajectory' with sufficient density in order to provide a good spatial resolution. After determining the geometrical setup, a system matrix was obtained, which describes the magnetization signal, induced by the

MNPs, as a function of the imaging space. In order to reconstruct images by the use of the system matrix, Algebraic Reconstruction Technique (ART), Selective Singular Value Decomposition (SSVD) Method and Truncated Singular Value Decomposition (TSVD) Method were applied to solve the matrix equation. Reconstructed images have resolution ranged in sub-millimeter level. In order to examine the effect of temperature changes in the model, a thermal solver was implemented using Pennes' Bioheat Equations. Energy of a focused ultrasound beam was used as the heat source and the equation was solved both in time and space, using the Finite Difference Time Domain Method (FDTD) in 2-Dimensional space. As a result, a realistic time-varying temperature data was included in the MPI model. Previous studies show that it is possible to estimate the temperature by utilizing a calibration curve that is acquired from the ratio of the fifth and the third harmonics of the magnetization signal, generated by MNPs, under different strength of applied sinusoidal field. But this was showed only for spectroscopic (0-D) data acquisition systems. In this thesis study two different methods were proposed for temperature distribution and applied for noise free case. For the first method, the algorithm is based on pixel-wise scanning and using a calibration curve obtained from 1D line scanning. The resolution and the maximum relative error was found to be 0.01°K and 0.003 per cent, respectively. Secondly, a linearization method for temperature estimation was proposed and the resolution and the maximum relative error was found to be 0.001°K and 0.063 per cent, respectively.

Keywords: Biomedical, Imaging, Magnetic, Nanoparticle, Temperature, Estimation, Ultrasound, Heating, Thermal, Therapy, Linearization, Calibration, Curve

ÖZ

MANYETİK NANOPARÇACIKLAR KULLANARAK SICAKLIK ÖLÇÜMÜ TAHMİNİ YAPILMASI: BENZETİM ÇALIŞMASI

Onuker, Gamze

Yüksek Lisans, Elektrik ve Elektronik Mühendisliği Bölümü

Tez Yöneticisi : Prof. Dr. Nevzat G. Gençer

Ortak Tez Yöneticisi : Dr. Can Barış Top

Aralık 2019, 97 sayfa

Biyomedikal görüntüleme sistemlerinde, sıcaklık dağılımı bilgisinin verilmesini sağlayan algortirmalar, teşhis ve tedavi yöntemlerinde kullanılmak üzere önem kazanmıştır. Bundan yola çıkılarak, bu tez çalışmasında, manyetik nano parçacıklar kullanarak sıcaklık dağılımı tahmini yapılması amaçlanmıştır. Manyetik nano parçacıklar (MNP), Manyetik Parçacık Görüntüleme (MPG) isimli, yeni bir biyomedikal görüntüleme tekniğinde görüntü izleyicisi olarak kullanılırlar. MPG'nin bulunuşundan beri, sıcaklık değişimlerinin, MNP'lar ve manyetik davranışlarına olan etkileri araştırılmaktadır. Bu araştırmalar şu zamana kadar göstermiştir ki, sıcaklık ve MNP davranışı arasında doğrusal olmayan bir ilişki vardır. Bu tez çalışmasının ilk adımı olarak, detaylı bir MPG sisteminin, simülasyon ortamında modellenmesi amaçlanmıştır. MATLAB ortamında, MPG sisteminin temel ögeleri olan 'Seçici', 'RF' ve 'Alıcı' bobin çiftleri modellenmiştir. Seçici ve RF bobin yarıçapları 25cm ve Alıcı bobin yarıçapı ise 10cm olarak ayarlanmıştır, bobinler tek sarımlı ve dairesel şekildedir. Tarama yöntemi olarak 'Lissajous Eğrileri' seçilmiştir. Geometrik kurulumun modellenmesi

sonrasında, manyetik alan üretimi de modellenmiş ve görüntü geri çatımında kullanılmak üzere bir sistem matrisi oluşturulmuştur. Bu sistem matrisi, MNP'ler tarafından manyetik alana maruz kaldıklarında üretilen manyetizasyon sinyali ve görüntüleme sistemi arasındaki ilişkiyi tarif eder. Görüntü geri çatımında 'Algebraic Reconstruction Technique (ART)', 'Selective Singular Value Decomposition(SSVD)' ve 'Truncated Singular Value Decomposition (TSVD)' yöntemleri kullanılmıştır. Geri çatım yapılan görüntüler, milimetre seviyesinde çözünürlüğe sahiptir. Bu sistemin yanı sıra, sıcaklık değişimlerinin MNP davranışı ve MPG sistemine olan etkisinin incelenmesi için ilk adım olarak gerçekçi bir sıcaklık dağılım haritası modellenmiştir. Bu modelde Pennes Bioheat denklemleri kullanılmış ve simülasyon ortamında 'odaklı ultrason' enerjisi kullanılarak bir takım sıcaklık dağılımları elde edilmiştir. Denklemlerin çözümlenmesinde 2 boyutu ele alan 'Zamanda Sonlu Farklar Metodu (FDTD)' kullanılmıştır. Sonuç olarak, gerçekçi bir sıcaklık dağılım modeli oluşturulmuş ve MPG modeline eklenmiştir. Daha önce yapılan çalışmalarda görülmektedir ki farklı genlik ve frekansta sinüsoidal manyetik alanla uyarılan MNP'lerin ürettiği sinyalin, beşinci ve üçüncü harmoniklerinin oranları kaydedilerek bir kalibrasyon eğrisi elde edilebilir ve bu eğri sıcaklık tahmininde kullanılabilir. Ancak bu çalışma yalnızca spektroskopik veri toplama sistemleri için geçerlidir. Bu tez çalışmasında, sıcaklık tahmini için iki farklı yöntem önerisinde bulunulmuştur ve bu yöntemler gürültüsüz durum için uygulanmıştır. İlk yöntemde, sıcaklık tahmin algoritması, görüntüleme alanını piksel – piksel taramaya dayalıdır. Çizgisel tarama yöntemi ile elde edilmiş bir kalibrasyon eğrisi kullanarak her pikseldeki sıcaklık tahmin edilmektedir. Bu yöntem sonuçları 0.01°K çözünürlüğe ve yüzde 0.003 hata payına sahiptir. İkinci yöntem ise bir lineerizasyon algoritmasıdır. Sıcaklık ve manyetizasyon arasındaki ilişki lineerize edilerek çözülmüştür. Bu yöntemin sonuçları ise 0.001°K çözünürlüğe ve yüzde 0.063 hata payına sahiptir.

Anahtar Kelimeler: Biyomedikal, Görüntüleme, Manyetik, Nanoparçacık, Sıcaklık, Tahmini, Ultrason, Isıtma, Termal, Terapi, Lineerizasyon, Kalibrasyon, Eğrisi

To my beloved mother and father ...

ACKNOWLEDGMENTS

I would like to thank;

To Prof. Dr. Nevzat G. Gençer for being the advisor in this thesis study and for his endless guidance and support.

To Dr. Can Barış Top for being the coadvisor in this thesis study and for his endless patience, guidance and support.

To my undergraduate research supervisor, Assist. Prof. Dr. Emine Ülkü Sarıtaş for her never ending guidance and support.

To all facilities of TUBITAK as this study was made possible by the grant of The Scientific and Technological Research Council of Turkey (TUBITAK) through the project number 117E246.

To the ones that are closest to my heart; my *cocodrillo*, Kubilay Serhat Elüstü; *canımın yarısı*, Yazgülü Sezer Yağlıcı; Özgür Umut Fikret Yağlıcı; Damla Alptekin; Deniz Özdamar; Burak Demirel for being patient with me and giving their endless love and support until the end, which made every problem easier to solve.

To my best friends; my *babies*, Çıtır, Mavi, Calamity and my soul mate *Zeus the Cat* for always accompanying me through the long sleepless nights and loving me in return for nothing.

To my mother, my most precious, Ferhan İclal Onuker for being my best friend, my truthful counselor, my shoulder to cry on, my laughing-crisis partner and my lodestar. And to my father, the love of my life, Coşkun Onuker for being my invincible hero, my guardian angel and my biggest fan and supporter. Their way of parenting made me the person I am proud to be, and I feel so grateful to have them. I treasure every memory we share.

TABLE OF CONTENTS

ABSTRACT	v
ÖZ	vii
ACKNOWLEDGMENTS	x
TABLE OF CONTENTS	xi
LIST OF TABLES	xiv
LIST OF FIGURES	xv
LIST OF ABBREVIATIONS	xxiv
CHAPTERS	
1 INTRODUCTION	1
1.1 Overview	1
1.2 Scope of the Thesis	4
1.3 The Outline of the Thesis	4
2 SIMULATIONS ON MAGNETIC PARTICLE IMAGING	5
2.1 Introduction	5
2.2 Detailed Numerical Simulations for Magnetic Particle Imaging	9
2.3 Coil Designs	11
2.3.1 Selection Field Coils	14
2.3.2 Drive Field Coils	16

2.3.3	Receive Coils	16
2.3.4	Scanning Sequences	22
2.3.5	System Acquisition and System Matrix	25
2.3.5.1	Time Domain System Matrix	25
2.3.5.2	Frequency Domain System Matrix	33
2.4	Image Reconstruction	44
2.4.1	Introduction	44
2.4.2	Reconstruction Techniques	44
2.4.2.1	Algebraic Reconstruction Technique	44
2.4.2.2	Least Squares Approach	46
2.5	Results and Conclusions	48
3	SIMULATIONS ON TEMPERATURE DISTRIBUTION FOR HARMONIC MOTION MICROWAVE DOPPLER IMAGING AND TEMPERATURE MAPPING USING MPI	56
3.1	Introduction	56
3.2	Finite Difference Time Domain Solution for Pennes Bioheat Equations	56
3.3	Realistic Numerical Simulations for Focused Ultrasound Heating	59
3.3.1	Introduction	59
3.3.2	Temperature Distribution Results of the Pennes Bioheat Model	63
3.4	Temperature Estimation Method Using Magnetic Nanoparticles	64
3.4.1	Introduction	64
3.4.2	Calibration Curves Obtained from MPI Relaxometer and 1D Scanning	65

3.4.3	Results and Conclusions	69
3.5	Linearization Method for Temperature Estimation Using Magnetic Nanoparticles	74
3.5.1	Introduction	74
3.5.2	Linearization Method	74
3.5.3	Results and Conclusions	79
4	CONCLUSION AND FUTURE WORK	87
4.1	Magnetic Particle Imaging Simulations	89
4.1.1	System Matrix Analysis	90
4.1.2	Image Reconstruction Analysis	91
4.2	Thermal Simulations	91
4.3	Novel MPI Temperature Imaging Methods	92
4.3.1	Pixel - Wise Linear Scanning (PWLS)	92
4.3.2	Model Based Linearization (MBL)	93
4.4	Future Work	94
	REFERENCES	95

LIST OF TABLES

TABLES

Table 2.1	Example of numerical values used in Biot-Savart equation.	13
Table 3.1	Numerical values used for Bioheat Equation.	60
Table 3.2	Slopes of calibration curves, obtained by using different parameters for the applied field strength and frequency.	68

LIST OF FIGURES

FIGURES

- Figure 1.1 Illustration of the HMMDI system [1]. Local vibrations that cause the harmonic motion are generated by the focused ultrasound probe. RF/Microwave Transmitter and Receiver Circuit basically generates microwave signals and detects the backscattered signal amplitude at the Doppler frequency. 3
- Figure 2.1 Schematic drawing of a typical magnetic nanoparticle. The diameter D_{core} of the magnetic core ranges between 1 - 100 nm. When the diameter of the nonmagnetic coating is thick enough, the nanoparticle shows 'superparamagnetic' behaviour, having single magnetic domain and a high magnetic moment. This provides a better tracking of magnetization of the MNPs. 5
- Figure 2.2 Stages of the magnetic behaviour that MNPs show, under externally applied magnetic field H . [2]. Each small sphere represents a nanoparticle and the small arrow on the spheres are basically the individual magnetic moments. Total Magnetization is shown as \mathbf{M} , and the applied field is shown as \mathbf{H} . Initially, both the Magnetization and the applied field are zero. As the applied field strength increased, net Magnetization vector starts to grow and MNPs start to align in the direction of applied magnetic field. 6

Figure 2.3 Normalized Magnetization Curve. (a) Change in Magnetization of a single superparamagnetic ironoxide nanoparticle is shown with respect to the applied magnetic field. The dynamic region is shown as the blue shaded area in the graph. (b) The Magnetization Curve versus the position is given. The nanoparticle, shown with a small, red circle is placed at $x=0$ position. 8

Figure 2.4 Positional change of the FFP in 2D cross-section. [2]. The first column represents the Selection Field. In each row of the second column, different instances of the alternating magnetic field is shown which is generated by the Drive Field coils. The third column is the superposition of the Drive and Selection Fields. Darker regions representing the FFP, change position in each row. 10

Figure 2.5 Steps for the realistic MPI simulation. Scheme shows the inputs and outputs of the first and second step blocks. The outputs for the first step is a realistic Magnetization signal data and a System Matrix that will both be used in the second step, while reconstructing the image. 11

Figure 2.6 Schematic illustration for single circular coil, showing the parameters used in Biot Savart equation that calculates the magnetic field. 12

Figure 2.7 Field generating coils. Selection Field coil pair (black) is placed in the z-direction and Drive Field coil pairs (red) are placed in both y and z directions. Small circle in the middle represents a volume of nanoparticles. The shape of the scanning trajectory is represented with the Lissajous Curve lines. The dimensions in this schematic is only for visualization, not reflecting the actual size. 13

Figure 2.8 3-Dimensional plot, showing the Magnetic Field vector lines for a Selection Field coil pair. In this illustration, both coils are placed in the x-y plane but one of them has a center at $z = 0.4$ m and the other is at $z = 1.4$ m and the current through the coils are in the opposite direction, in order to produce inhomogenous magnetic field. Currents going through each coil have opposite direction therefore, generated magnetic fields are identical but have opposite direction. This produces a FFP, residing in the high symmetric point between Selection Field coils, at $x = 0.4$, $y = 0.4$ and $z = 0.9$ 14

Figure 2.9 Compared B-field values for analytical and discrete computations. As the coil center was set to be at $z = 0.9$ meter, the B field reaches its maximum value around $z = 0.9$. The maximum relative error calculated between the analytical and the discrete solutions was approximately 0.6 percent. 15

Figure 2.10 Complete coil configuration that was used in the MPI simulation. Drive and Selection field coils placed on the x-y plane have the same position, therefore they are not *visually* distinguishable, but the pairs are represented with dark blue and red circles in the figure. Drive Field coil pair of the y-channel is represented with purple and yellow circles. Lastly, the y-sensitive and z-sensitive Receive coils are represented with light blue and green circles, respectively. 17

Figure 2.11 Visualization of the concepts that was described in equations (2.11), (2.12) and (2.13). E is the Electric Field through the circular coil, $\frac{\partial B}{\partial t}$ is the Magnetic Flux Density and $u(t)$ is the voltage signal induced at the ends of the coil. 19

Figure 2.12 Schematic presentation for the Cartesian Trajectory [2]. 23

Figure 2.13 Schematic presentation for the Lissajous Trajectory [2]. 24

Figure 2.14 Sorted singular values for the system matrix that obtained from Lissajous Trajectory. Maximum and minimum values are 1.133×10^{-7} and 3.729×10^{-9} respectively. The condition number is then found to be approximately 30.38. 29

Figure 2.15 Sorted singular values for the system matrix that obtained from Cartesian Trajectory. Maximum and minimum values are 8.588×10^{-10} and 1.342×10^{-13} respectively. The condition number is then found to be 6.3979×10^3 30

Figure 2.16 Image basis vectors transformed to 2D image that correspond maximum (upper) and minimum (lower) singular values that are obtained from Lissajous Scanning. 31

Figure 2.17 Image basis vectors transformed to 2D image that correspond maximum (upper) and minimum (lower) singular values that are obtained from Cartesian Scanning. 32

Figure 2.18 Schematic illustration explaining the frequency domain conversion of a system matrix. 33

Figure 2.19 Energy distribution of y and z- channel system functions for frequencies between 0 to 1000 kHz, that was obtained from Lissajous Scanning. It can be seen that the energy is dominant at harmonic frequencies. 34

Figure 2.20 Energy distribution of y and z- channel system functions for frequencies between 0 to 4000 kHz, that was obtained from Cartesian Scanning. It can be seen that the energy is dominant at harmonic frequencies. 35

Figure 2.21 Sorted singular values for the system matrix that obtained from Lissajous Trajectory. Maximum and minimum values are 1.057×10^{-8} and 6.24×10^{-12} respectively. The condition number is then found to be approximately 1.69×10^3 36

Figure 2.22 Sorted singular values for the system matrix that obtained from Cartesian Trajectory. Maximum and minimum values are 4.196×10^{-8} and 6.121×10^{-14} respectively. The condition number is then found to be approximately 6.855×10^5	37
Figure 2.23 Image basis vectors transformed to 2D image that correspond maximum (upper) and minimum (lower) singular values that are obtained from Lissajous Scanning.	38
Figure 2.24 Image basis vectors transformed to 2D image that correspond maximum (upper) and minimum (lower) singular values that are obtained from Cartesian Scanning.	39
Figure 2.25 Spatial Frequencies for y-channel System Matrix that is obtained from Lissajous Trajectory scan.	40
Figure 2.26 Spatial Frequencies for z-channel System Matrix that is obtained from Lissajous Trajectory scan.	41
Figure 2.27 Spatial Frequencies for y-channel System Matrix that is obtained from Cartesian Trajectory scan.	42
Figure 2.28 Spatial Frequencies for z-channel System Matrix that is obtained from Cartesian Trajectory scan.	43
Figure 2.29 Illustrative explanation for the idea behind ART. c_0 is the initial guess and c_i are the projections on the line equations of the system, which are updated by using equation (2.50). c is the actual particle distribution that is aimed to be approximated by using this method.	45
Figure 2.30 2D cross-section of the particle distribution that had been used as the <i>phantom</i> in this simulation. For simplicity, magnetic core concentration for all nanoparticles in this distribution of the phantom was chosen to be equal.	48

Figure 2.31 Results for Cartesian Scanning Trajectory, without any additional noise. PSNR values for ART, SSVD and TSVD are 9.23, 54.31, 47.68 respectively.	49
Figure 2.32 Results for Lissajous Scanning Trajectory, without any additional noise. PSNR values for ART, SSVD and TSVD are 8.38, 283.55, 57.95 respectively.	50
Figure 2.33 SNR values for different frequencies. Maximum SNR value is found to be approximately 34 dB and it can be seen that SNR value increases at signal harmonics. Comparing these results with experimental data given in [3], it can be concluded that 34 dB SNR level is acceptable as 40dB SNR was observed experimentally for 200 averages.	51
Figure 2.34 Results for Cartesian Scanning Trajectory, with $SNR = 50dB$ additional noise. PSNR values for ART, SSVD and TSVD are 8.07, 19.3686, 19.5740 respectively.	52
Figure 2.35 Results for Lissajous Scanning Trajectory, with $SNR = 50dB$ additional noise. PSNR values for ART, SSVD and TSVD are 8.07, 21.2961, 21.3319 respectively.	53
Figure 2.36 Results for Cartesian Scanning Trajectory, with $SNR = 34dB$ additional noise. PSNR values for ART, SSVD and TSVD are 7.13, 17.2133, 16.0055 respectively.	54
Figure 2.37 Results for Lissajous Scanning Trajectory, with $SNR = 34dB$ additional noise. PSNR values for ART, SSVD and TSVD are 8.07, 17.2133, 17.4243 respectively.	55
Figure 3.1 Schematical illustration for the setup that has been modelled in this study. Focused ultrasound was modelled to be applied in y-direction in the imaging plane.	59

Figure 3.2	Illustration of the 3-D setup. The limits of FOV is shown with blue solid lines that forms a rectangular volume. Focused Ultrasound Transducer is modelled such that it excites along y-direction and the focus point is set to be at the center of the volume. The cross section area is shown with the dashed, blue lines.	61
Figure 3.3	Illustration that shows the boundary condition and heat distributions. Q_m is uniform everywhere in the area.	61
Figure 3.4	Cross section of the actual 3-D focused ultrasound intensity distribution.	62
Figure 3.5	Change in temperature distribution when focused ultrasound applied in the imaging area for different durations between 10 ms and 2 seconds, along y-direction.	63
Figure 3.6	Plots showing changes in the Ratio of Harmonics with respect to H_0/T . All of the three plots were obtained from 0-D simulations with only one excitation field with frequency 1470Hz. From upper to the lower graphs, the amplitude of the applied field increases.	66
Figure 3.7	Calibration Curve obtained from MPI relaxometer by changing the temperature from 310 to 320 Kelvin, under applied magnetic field with 1mT strength and 20kHz frequency.	67
Figure 3.8	Calibration Curve obtained from 1D Line scanning by changing the temperature from 310 to 320 Kelvin, under applied magnetic field with 1mT strength and 20kHz frequency and an additional 2 T/m Selection Field.	68
Figure 3.9	Estimated temperature distribution around the ultrasound focus area (limits were marked with red lines) and the actual temperature distribution in the imaging space, after the ultrasound was applied for 3 seconds. Maximum relative error was calculated as 0.003%, approximately.	69
Figure 3.10	Error Distribution between the original temperature distribution and the estimated temperature distribution.	70

Figure 3.11 Four different calibration curve data, obtained for noise free case and noise added cases when SNR is 80, 60 and 40 dB, respectively. It can be seen that as SNR decreases, data become more dispersed and lose the linear structure. For this reason, one can conclude that the error in temperature estimation would increase as SNR decreases. 71

Figure 3.12 Difference between the calibration curve data, obtained for noise free case and noise added cases when SNR is 80, 60 and 40 dB, respectively. 72

Figure 3.13 Difference data in the signal spectrum. It can be seen that the signal levels at the 3rd and 5th harmonics changes about -40 dB, for 1 K alteration in the ambient temperature. 73

Figure 3.14 Estimated temperature distribution and the actual temperature distribution in the imaging space for the noise free case, after the ultrasound was applied for 2 seconds. For simplicity, it was assumed that the FOV is fully covered with uniform particle distribution. Maximum relative error is calculated approximately as 0.063% 79

Figure 3.15 Temperature estimation results for noise added case. SNR is set to be 80 dB and FUS was applied for 2 seconds. Maximum relative error is calculated approximately as 0.0706% 80

Figure 3.16 Temperature estimation results for noise added case. SNR is set to be 60 dB and FUS was applied for 2 seconds. Maximum relative error is calculated approximately as 0.9805% 81

Figure 3.17 Temperature estimation results for noise added case. SNR is set to be 40 dB and FUS was applied for 2 seconds. Maximum relative error is calculated approximately as 11.5240% 82

Figure 3.18 Error Distribution between the original temperature distribution and the estimated temperature distribution for the noise free case. 83

Figure 3.19 Error Distribution between the original temperature distribution and the estimated temperature distribution when SNR is 80 dB. 84

Figure 3.20 Error Distribution between the original temperature distribution and the estimated temperature distribution when SNR is 60 dB.	85
Figure 3.21 Error Distribution between the original temperature distribution and the estimated temperature distribution when SNR is 40 dB.	86

LIST OF ABBREVIATIONS

2D	2 Dimensional
3D	3 Dimensional
ART	Algebraic Reconstruction Technique
CT	Computed Tomography
FDTD	Finite Difference Time Domain
FFP	Field Free Point
FOV	Field Of View
HMMDI	Harmonic Motion Microwave Doppler Imaging
MNP	Magnetic Nanoparticle
MPI	Magnetic Particle Imaging
MRI	Magnetic Resonance Imaging
MRI-HIFU	MRI-guided High Intensity Focused Ultrasound
MSE	Mean Square Error
PAM	Passive Acousting Mapping
PSNR	Peak Signal to Noise Ratio
SVD	Singular Value Decomposition
SSVD	Selective Singular Value Decomposition
TSVD	Truncated Singular Value Decomposition
SNR	Signal to Noise Ratio

CHAPTER 1

INTRODUCTION

1.1 Overview

The effect of heating processes on living tissues is an important research topic for medical applications, especially for cancer and tumor treatments. The procedure of raising the temperature of a part of, or the whole body above normal for a defined period of time is called *Hyperthermia* [4] and clinical treatments that use this procedure are generally called *Thermal Therapies*.

During thermal therapies, providing an accurate estimation of temperature distribution is crucial, in terms of avoiding undesirable thermal damage. Therefore during the therapy, mapping the spatial temperature distribution is very important. Image-guided thermal therapies are now routinely applied in a variety of clinical settings [5]. RF heating, Microwave Hyperthermia, Laser therapies and Focused Ultrasound are some of the methods that has been proposed.

Methods for monitoring the in-vivo temperature can both be invasive and non-invasive. The gold standard for in vivo temperature measurement is the utilisation of invasive temperature sensing probes as it would not modulate the thermal therapy field and would be insensitive to strains due to thermal expansion and/or patient motion [5]. However, the use of invasive temperature probs, conflicts with the idea of avoiding damage to the living tissue.

Computed Tomography based thermometry is another method for temperature monitoring. This method is recommended as it allows avoiding unintended damage of the healthy tissues during the procedure by providing a detailed tissue temperature dis-

tribution [6]. Unfortunately, the thermal sensitivity coefficient for CT thermometry is in the order of -0.5 Hounsfield units (HU) per Celcius, which limits the thermal resolution [5], thus this technique fails to provide detail and clarity of a thermal image.

In several methods, ultrasound acquisitions are being used in temperature mapping. For instance, Passive Acousting Mapping (PAM) technique uses focused ultrasound transducer as a sensor to receive acoustic emissions generated in the treatment zone [7]. However, using this methods provides detection of non-thermal signals such as cavitation, and since the passive acoustic signals from cavitation and thermal strain are also affected by temperature dependent changes in speed of sound (SOS) and attenuation, only relative temperature changes can be estimated [5]. Pulse-echo is the most common focused ultrasound method employed for temperature estimation, which uses a single transducer to transmit acoustic signals and receives acoustic wave responses generated by the tissue interaction. In this method, temperature can ideally be estimated only if the tissue interaction is temperature independent [5].

MRI monitoring is currently clinical standard for non-invasive temperature mapping [5]. MRI-guided High Intensity Focused Ultrasound (MRI-HIFU) therapy and MRI-guided Microwave Hyperthermia are two examples of most commonly used techniques in thermal therapy. MRI-monitoring is preferable as it is non-invasive and provides detailed and accurate temperature estimation, without using any a priori calibration in the target tissue [5]. Nevertheless, it is disadvantageous in terms of cost issues and portability.

In this thesis study, the motivation is to develop a temperature estimation method that is non-invasive and practical, provides good thermal resolution and accurate mapping, and is portable. In order to achieve this goal, it is proposed to use Magnetic Nanoparticles (MNP) and take the advantage of their temperature-dependent magnetic behavior [8]. With this temperature estimation method, specifically, it is aimed to obtain spatial temperature distributions in order to monitor temperature changes that may occur during the process of Harmonic Motion Microwave Doppler Imaging (HMMDI) [9].

In HMMDI method, in order to obtain information on tissue elastic and dielectric properties, a focused ultrasound induces local vibrations, combined with the transmission of microwave signals. Backscattered and received microwave signal is a phase and amplitude modulated due to the effect of vibration [9]. The illustration of an HMMDI system is given in Fig.1.1.

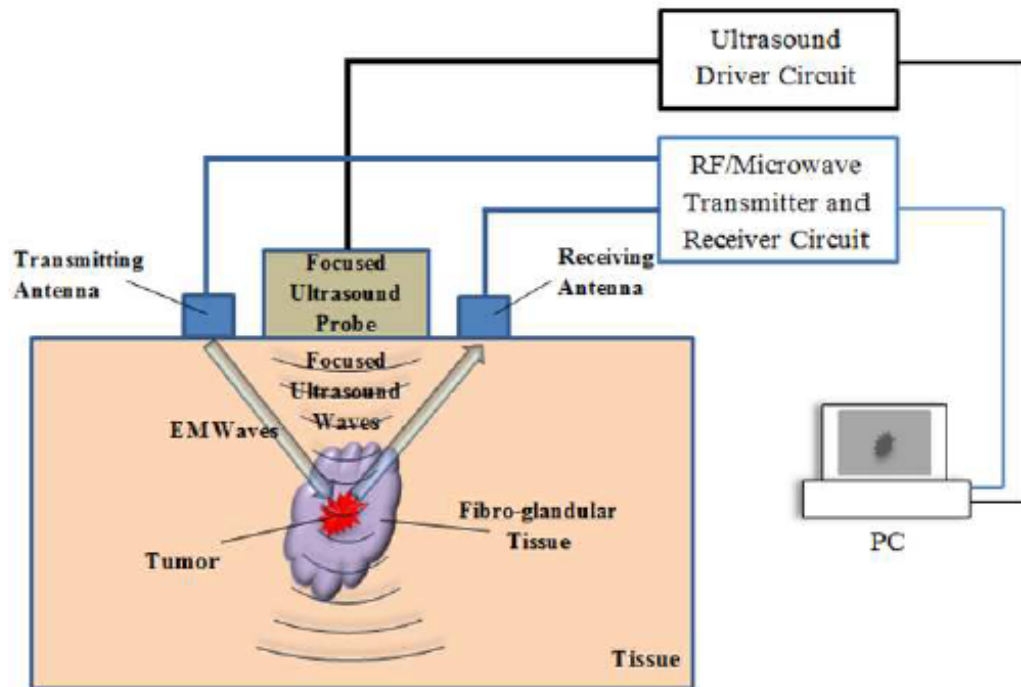


Figure 1.1: Illustration of the HMMDI system [1]. Local vibrations that cause the harmonic motion are generated by the focused ultrasound probe. RF/Microwave Transmitter and Receiver Circuit basically generates microwave signals and detects the backscattered signal amplitude at the Doppler frequency.

Although HMMDI is an imaging method, the use of focused ultrasound and waves may result in temperature rises inside the tissue. In terms of safety issues, it is important to monitor the temperature distribution. In this thesis study, the aim is to achieve temperature mapping using MNPs, in a simulation environment. Although, the initial motivation of this study is to apply this method during HMMDI, proposed method is applicable in other imaging or thermal therapy methods.

1.2 Scope of the Thesis

In the scope of this thesis, we

- Developed a simulation model of a Magnetic Particle Imaging system by considering all input parameters that can effect the results,
- Obtained system matrices and examine their characteristics.
- Simulated image reconstruction for MPI and thermal imaging, using different approaches.
- Developed a 2D temperature distribution model by using FDTD on Pennes' Bioheat Equations, examine the effect of the energy of a focused ultrasound beam as the heating source.
- Used state-of-the-art methods to estimate of temperature in 0-D.
- Proposed two methods to estimate of temperature distribution in 2-D and simulated their performance assuming infinite SNR.

1.3 The Outline of the Thesis

In Chapter 2, characteristics of an MPI system and the parameters that are important for obtaining a detailed numerical simulation are discussed. The system components are verified, system matrices are examined, and image reconstruction techniques are explained. Lastly image reconstruction results are given.

In Chapter 3, a temperature distribution model for HMMDI is defined by utilizing Pennes' Bioheat Equations. The effect of a focused ultrasound in the simulation medium is examined and 2D temperature variations is obtained. Two different methods were proposed for temperature estimation using MNPs and results were presented.

In Chapter 4, conclusions of the study are discussed with its limitations, and possible subjects for the future studies are given.

CHAPTER 2

SIMULATIONS ON MAGNETIC PARTICLE IMAGING

2.1 Introduction

Magnetic Particle Imaging (MPI) is a relatively new medical imaging technique, which was invented by Bernhard Gleich in 2005. It is proposed as a promising imaging modality characterized by both high spatial resolution and high sensitivity [8]. This technique determines the spatial distribution of Magnetic Nanoparticles (MNP), schematically given in Fig. 2.1, injected into the body, using them as imaging tracers [10][11]. Iron oxide is a commonly used magnetic material, which consists of a magnetic core and a nonmagnetic coating that prevents agglomeration¹.

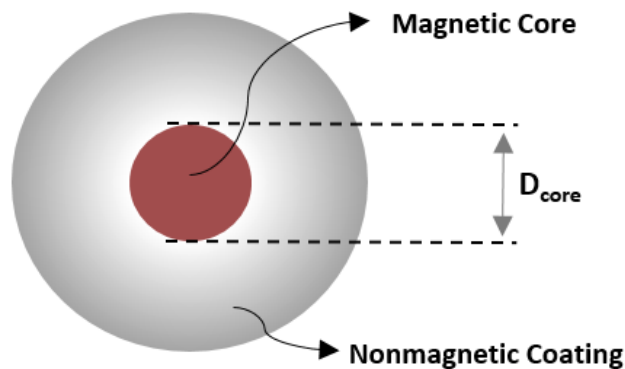


Figure 2.1: Schematic drawing of a typical magnetic nanoparticle. The diameter D_{core} of the magnetic core ranges between 1 - 100 nm. When the diameter of the nonmagnetic coating is thick enough, the nanoparticle shows 'superparamagnetic' behaviour, having single magnetic domain and a high magnetic moment. This provides a better tracking of magnetization of the MNPs.

¹ The action of MNPs collecting together in a mass.

MPI uses the nonlinear magnetization characteristics of magnetic materials, as they give a characteristic response when exposed to an external magnetic field [8]. Magnetization signal M , is described as the sum of all magnetic moments of nanoparticles:

$$\vec{M} = \frac{1}{dV} \sum_{j=0}^N \vec{m}_j \quad (2.1)$$

Magnetization is initially zero due to Brownian motion, as directions of each magnetic moment of particles are initially randomly distributed. With an external magnetic field applied, directions of magnetic moments start to align in the same direction with the applied field, causing a *net magnetization signal in the direction of the applied field*. The importance of the term 'superparamagnetic behaviour' appears here, as nanoparticles with *high magnetic moments* means higher Magnetization signal and in MPI the aim is to collect this Magnetization signal. Change in magnetization is given in Fig. 2.2.

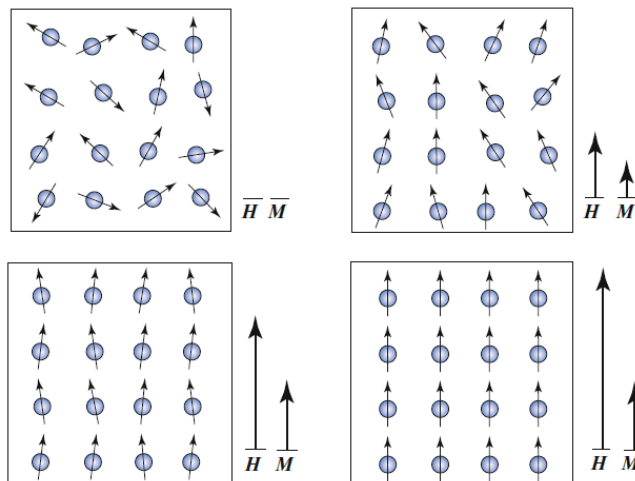


Figure 2.2: Stages of the magnetic behaviour that MNPs show, under externally applied magnetic field H . [2]. Each small sphere represents a nanoparticle and the small arrow on the spheres are basically the individual magnetic moments. Total Magnetization is shown as \mathbf{M} , and the applied field is shown as \mathbf{H} . Initially, both the Magnetization and the applied field are zero. As the applied field strength increased, net Magnetization vector starts to grow and MNPs start to align in the direction of applied magnetic field.

Magnetization signal can be modelled using the Langevin Function. The mathematical

expression for the Langevin Function, L is given as

$$L(\xi) = \begin{cases} \coth(\xi) - \frac{1}{\xi}, & \xi \neq 0 \\ 0, & \xi = 0 \end{cases} \quad (2.2)$$

And the Magnetization, M is described as

$$M(B) = cmL(\beta B) \quad (2.3)$$

where

$$\beta = \frac{\mu_0 m}{k_B T} \quad (2.4)$$

In equation (2.4), k_B is the Boltzmann constant, T is the ambient temperature, μ_0 denotes the permeability of free space and m is the modulus of the magnetic moment of single particle, given with

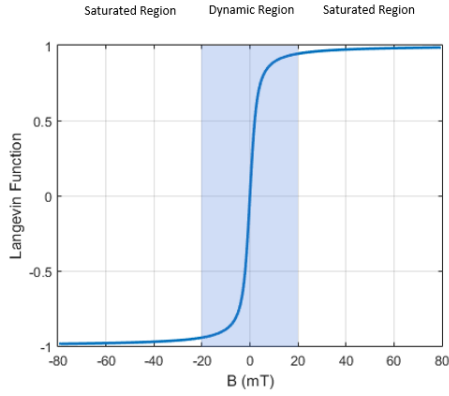
$$m = V_{\text{particle}} M_{\text{SAT}} \quad (2.5)$$

where

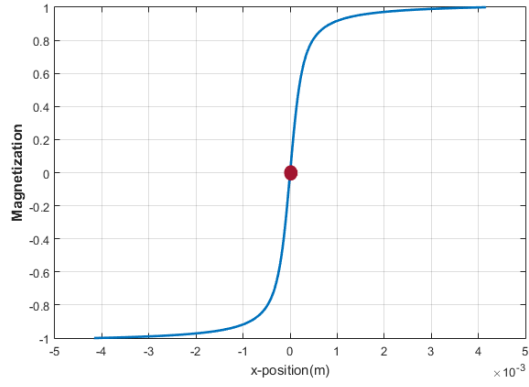
$$V_{\text{particle}} = \frac{1}{6} \pi D_{\text{core}}^3 \quad (2.6)$$

In equation (2.3), magnetic moment m , is multiplied with the particle core concentration, c . Magnetic moment of a particle depends on the particle core volume, V_{particle} and the saturation magnetization, M_{SAT} , of the material that is the particle core is made of.

It can be seen that nanoparticles are available to respond to an interval of applied field strength (between -20 and 20 mT for the precise example in Fig. 2.3a) and at a certain point, all of them remain aligned in the direction of the applied field, i.e., being *saturated*. The spatial encoding in MPI takes the advantage of this fact that the particle magnetization saturates. Consequently, for a known distribution of magnetic field strength in a medium, the particles that are available to respond are also known. This can further be explained by examining a typical magnetization curve given in Fig. 2.3a.



(a) Magnetization w.r.t. applied field strength.



(b) Magnetization w.r.t position.

Figure 2.3: Normalized Magnetization Curve. (a) Change in Magnetization of a single superparamagnetic ironoxide nanoparticle is shown with respect to the applied magnetic field. The dynamic region is shown as the blue shaded area in the graph. (b) The Magnetization Curve versus the position is given. The nanoparticle, shown with a small, red circle is placed at $x=0$ position.

In Fig. 2.3a, the relation between the particle magnetization and the externally applied magnetic field is shown. For the dynamic region, nanoparticles are available to respond to field changes. The magnetization shows a sharp increase and decrease around 0 mT external field. When an alternating magnetic field applied on MNPs, they produce an alternating Magnetization Signal, flipping back and forward in the dynamic region. This signal can be collected using coils. As the strength of the applied magnetic field increases, MNPs goes into saturation and MNPs are no longer available to respond changes in the external magnetic field. Therefore, it is only possible to collect signals from MNPs that are in the dynamic region.

In order to collect spatial data during the scanning process in MPI, dynamic and saturated regions in imaging space are being changed by the help of field generating coils. Selected 'dynamic region' is called the 'Field Free Point (FFP)' [8] where the applied magnetic field is adjusted accordingly such that particles in the FFP are available to generate Magnetization signal.

In this chapter, a 2D scanning MPI system is simulated. The model presented in [12] was followed for the coil geometries, scanning sequence, and MNP characteristics. The simulation was implemented using MATLAB (The MathWorks, Inc., MA, USA)[13], creating a 3-Dimensional MPI system model.

2.2 Detailed Numerical Simulations for Magnetic Particle Imaging

In order to model a simulation system, one should consider all inputs and parameters that could effect the results of the system in real life. In this particular case of an MPI system; characteristics of the applied fields, coil geometries and sensitivities, shape and volume of MNPs and data acquisition sequence were considered as the main effective parameters. The purpose is to mimic an imaging system that can be used for clinical purposes, hence, parameters were chosen to represent conditions expected for clinical applications; allowing for a fast image acquisition with a spatial resolution in the millimeter range [12].

The simulation system has two main steps starting with generating data, in other words obtaining the Magnetization signal. Second step is then, spatially encoding this data to reconstruct images.

A basic MPI system consists of *Selection Field coils*, *Drive Field coils* and *Receive coils*. Selection Field coils generate static magnetic field whereas the Drive Field coils generate an alternating magnetic field. During the scanning process, the total magnetic field in the medium spatially changes in order to move the so called '*Field Free Point (FFP)*'. This process is schematically explained in Fig. 2.4. The result of this scanning process is a **spatially dependent** Magnetization signal.

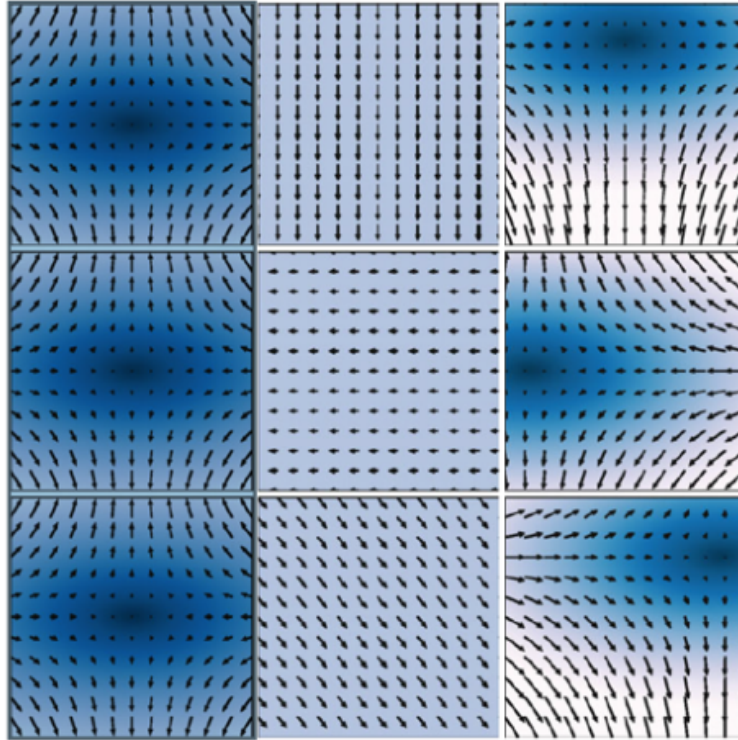


Figure 2.4: Positional change of the FFP in 2D cross-section. [2]. The first column represents the Selection Field. In each row of the second column, different instances of the alternating magnetic field is shown which is generated by the Drive Field coils. The third column is the superposition of the Drive and Selection Fields. Darker regions representing the FFP, change position in each row.

In this simulation, the aim was to define coil geometries, obtain a 3D setup, generate the desired total magnetic field, B , and adjust the scanning sequence so that the FFP moves along a certain trajectory. This trajectory was chosen as the 'Lissajous Trajectory' for this particular study. The shape of this trajectory was adjusted accordingly to cover the whole scanning space with a sufficient density in order to provide a good spatial resolution.

As it was shown in the schematic in Fig. 2.5 the first step was to define a 3D medium in order to place the coil geometries. After generating the fields, a phantom was defined in this medium, including the MNP characteristics.

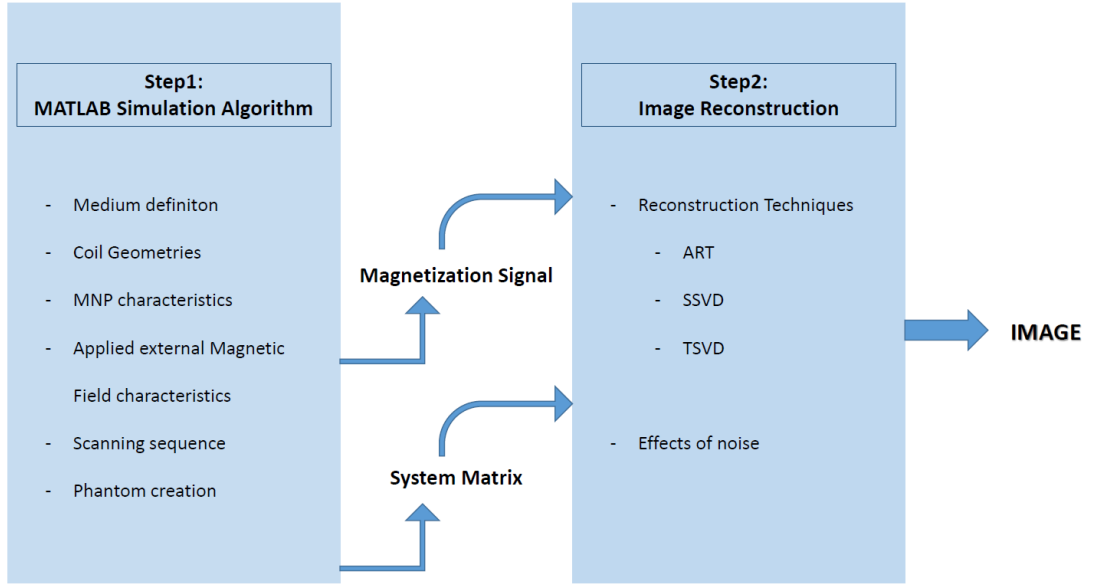


Figure 2.5: Steps for the realistic MPI simulation. Scheme shows the inputs and outputs of the first and second step blocks. The outputs for the first step is a realistic Magnetization signal data and a System Matrix that will both be used in the second step, while reconstructing the image.

2.3 Coil Designs

In MATLAB environment, it is important to chose a suitable step-size in discretization of the continuous variables. Coil models were assumed to be circular conductors with single turn, and they were represented with 360 infinitely thin segments and all fields were assumed to be generated by the coils [12]. Magnetic Fields were computed, using the Biot-Savart Law given below in equation (2.7), with the numerical values given in table (2.1).

$$\vec{B}(\vec{r}) = \frac{\mu_0 I}{4\pi} \int d\vec{L} \times \frac{(\vec{r} - \vec{r}')}{|\vec{r} - \vec{r}'|^3} \quad (2.7)$$

This equation calculates the magnetic field vector $\vec{B}(\vec{r})$ for every position \vec{r} in the imaging space. μ_0 is the free space permeability, I is the amplitude of the current going through the coil and \vec{r}' is the source point. without changing the notation, the

discretized equation that is used to calculate the magnetic field can be written as

$$\vec{B}(\vec{r}) = \frac{\mu_0 I}{4\pi} \sum_{i=1}^{360} d\vec{L}_i \times \frac{(\vec{r} - \vec{r}'_i)}{|\vec{r} - \vec{r}'_i|^3} \quad (2.8)$$

The geometry that describes the variables in the discretized Biot Savart equation is simply illustrated in Fig. 2.6.

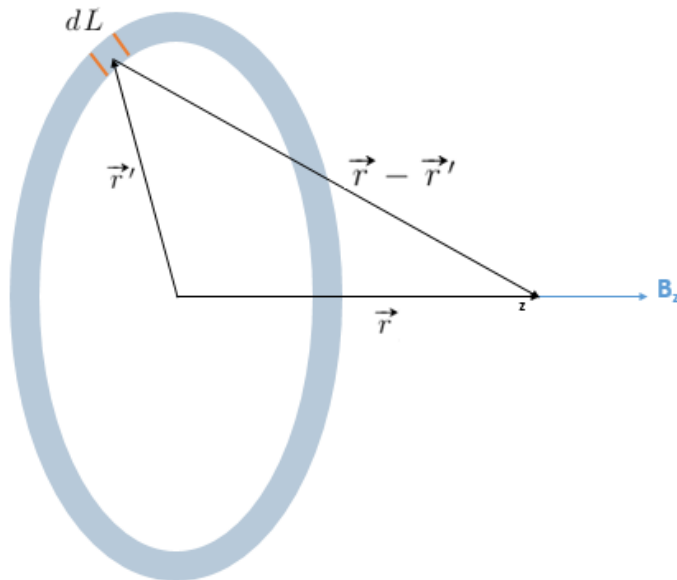


Figure 2.6: Schematic illustration for single circular coil, showing the parameters used in Biot Savart equation that calculates the magnetic field.

Drive and Selection Field coils were described with the same shape and radius, and for each pair, coils were placed to be one meter apart from each other. The coil simulation geometry is shown in Fig. 2.7. Imaging center was chosen to be at the position $x= 0.4$, $y= 0.7$ and $z= 0.9$ meters. Numerical values that were used in this simulation are given in Table 2.1. I_z and f_z describe the amplitude and frequency values for sinusoidal currents flowing through the Drive Field coil pair that is placed on x-y plane and I_y and f_y describe the coil pair placed on x-z plane.

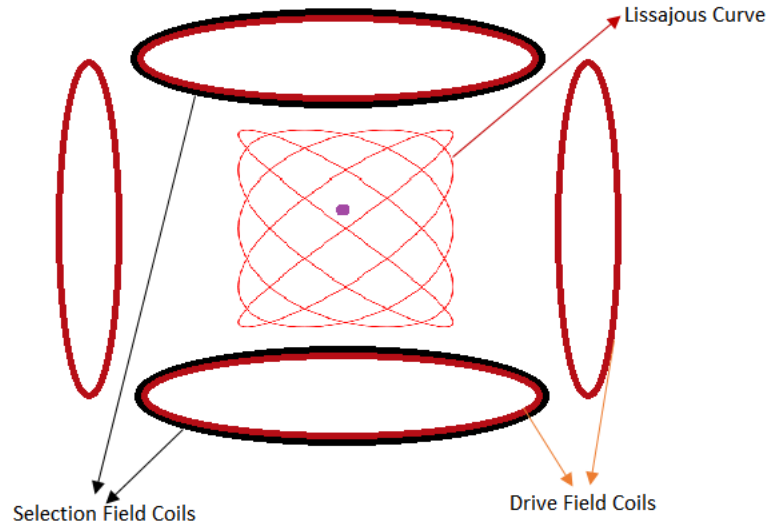


Figure 2.7: Field generating coils. Selection Field coil pair (black) is placed in the z-direction and Drive Field coil pairs (red) are placed in both y and z directions. Small circle in the middle represents a volume of nanoparticles. The shape of the scanning trajectory is represented with the Lissajous Curve lines. The dimensions in this schematic is only for visualization, not reflecting the actual size.

	Selection Field Coils	Drive Field Coils
$I_z(A)$	1.4549	0.0571
$I_y(A)$	-	0.0571
$f_z(kHz)$	-	25.25
$f_y(kHz)$	-	25.508
$R(m)$	0.25	0.25

Table 2.1: Example of numerical values used in Biot-Savart equation.

2.3.1 Selection Field Coils

In MPI, Selection Field coils are responsible from generating an inhomogenous, static magnetic field in the imaging medium, as it is illustrated in Fig. 2.8. For this simulation, the current passing through coils were set such that an FFP was produced at the center of this inhomogenous field. The gradient strength in the z-direction, $\frac{\partial B_z}{\partial z}$, was set to be $2.5 T/m$ and for x and y directions it was the half of the $\frac{\partial B_z}{\partial z}$, meaning that $\frac{\partial B_y}{\partial y} = \frac{\partial B_x}{\partial x} = 1.25 T/m$.

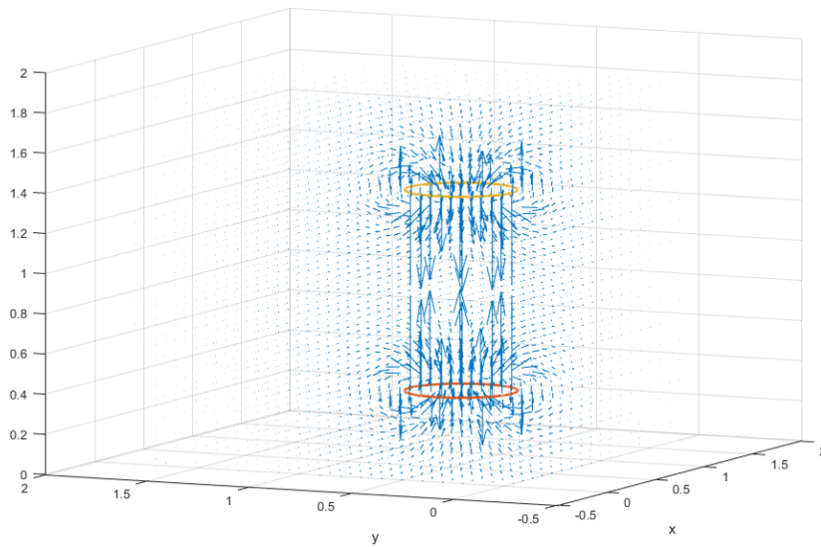


Figure 2.8: 3-Dimensional plot, showing the Magnetic Field vector lines for a Selection Field coil pair. In this illustration, both coils are placed in the x-y plane but one of them has a center at $z = 0.4$ m and the other is at $z = 1.4$ m and the current through the coils are in the opposite direction, in order to produce inhomogenous magnetic field. Currents going through each coil have opposite direction therefore, generated magnetic fields are identical but have opposite direction. This produces a FFP, residing in the high symmetric point between Selection Field coils, at $x = 0.4$, $y = 0.4$ and $z = 0.9$.

It is important to test the accuracy of the numerical model, in order to decide discretization parameters. Using the Biot-Savart Law, field on the axis of a circular coil can be found using equation (2.9). Using this equation, z-component of the static Magnetic Field was calculated on the axis (z-axis) of single Selection Field coil and they were compared with the numerical solution that was computed in the simulation. The results are shown in Fig. 2.9.

$$B_z = \frac{\mu_0}{4\pi} \frac{2\pi R^2 I}{(z^2 + R^2)} \quad (2.9)$$

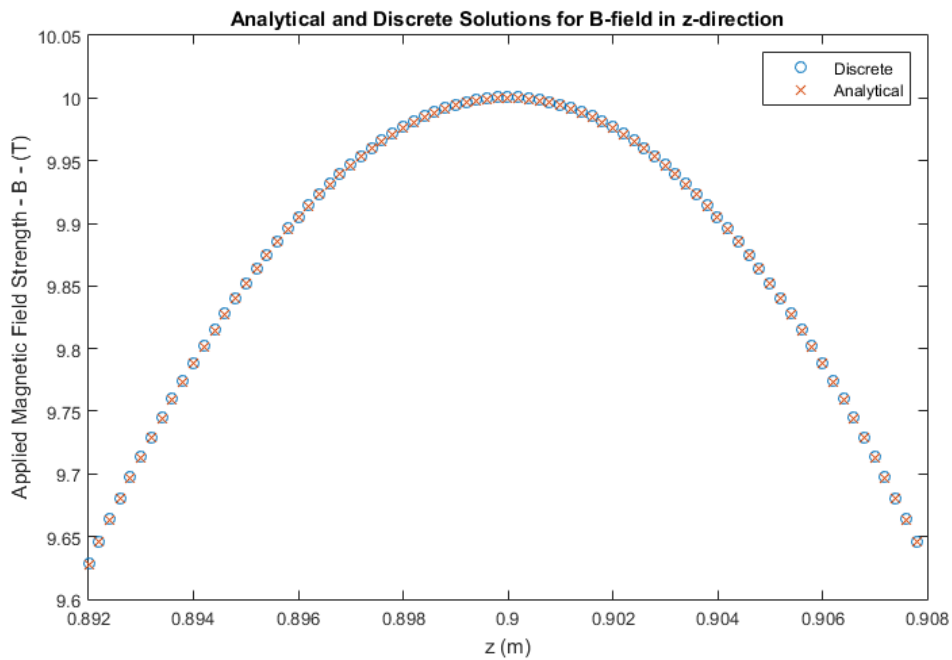


Figure 2.9: Compared B-field values for analytical and discrete computations. As the coil center was set to be at $z = 0.9$ meter, the B field reaches its maximum value around $z = 0.9$. The maximum relative error calculated between the analytical and the discrete solutions was approximately 0.6 percent.

2.3.2 Drive Field Coils

It is possible to move the FFP around a certain trajectory in the imaging medium by the help of the Drive Field. In this MPI simulation, two Drive Field coil pairs were used, placed on x-y and x-z planes, moving the FFP along z - axis and y - axis, respectively. This provides a 2-D imaging area on y-z plane of the 3-D simulation system.

Coils were described identically, having circular shape and 50 cm diameter with a single turn. Coils in each pair were placed 1 meter apart from each other, and the currents going through each coil in a pair have the same direction. This produces an oscillating but relatively homogenous magnetic field. The current amplitudes given in Table (2.1) was set to generate a Magnetic Field strength of $20 \text{ mT}\mu_0^{-1}$ both in z and y direction. With these characteristics, Field of View (FOV) covers 16 mm in z-direction and 32 mm in y-direction.

2.3.3 Receive Coils

Simulated MPI system consists of two Receive Coils with circular shape and 10 cm radius. One of them is placed on the x-y plane and sensitive to field changes in the z-direction. And the second coil is placed on the x-z plane, meaning that it is sensitive to field changes in the y-direction.

The Drive Field and Selection Field coils had centers that were 50 cm away from the imaging center. Receive coils have centers that are 15 cm away from the imaging center. Complete coil configuration that was used for this study is given in Fig. 2.10.

In order to collect the Magnetization Signal via Receive Coils, the *Reciprocity Theorem* describing the relation between the magnetic flux through a coil and the corresponding induced voltage was used.

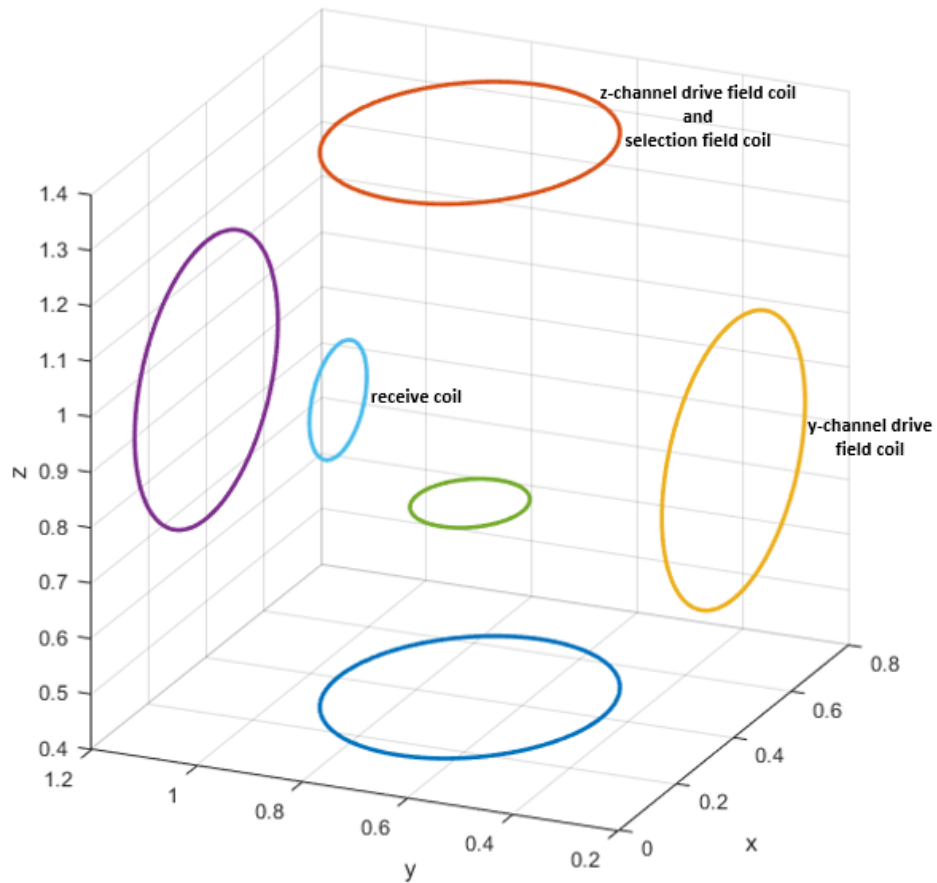


Figure 2.10: Complete coil configuration that was used in the MPI simulation. Drive and Selection field coils placed on the x-y plane have the same position, therefore they are not *visually* distinguishable, but the pairs are represented with dark blue and red circles in the figure. Drive Field coil pair of the y-channel is represented with purple and yellow circles. Lastly, the y-sensitive and z-sensitive Receive coils are represented with light blue and green circles, respectively.

Considering a single Receive Coil, a circular conductor loop, enclosing a surface S , the voltage at the end points can be described as the integration of the electric field strength along the coil:

$$u(t) = \oint \vec{E}(l, t) \cdot dl \quad (2.10)$$

Here, $u(t)$ is the induced signal, $\vec{E}(l, t)$ is the electric field strength and l represents the position on the coil.

Using the Faraday's law of induction, the line integral for the Electric Field strength, which is the right hand side of the equation (2.10), can also be described using the time derivative of the Magnetic Flux, ϕ_s , as follows:

$$\oint \vec{E}(l, t) \cdot d\vec{l} = -\frac{d}{dt}\phi_s \quad (2.11)$$

The integral equation describing the Magnetic Flux through the surface enclosed by the coil is

$$\phi_s = \int \vec{B}(r, t) \cdot d\vec{S} \quad (2.12)$$

Inserting the equation (2.12) in equation (2.11), and combining with equation (2.10), one can obtain

$$u(t) = -\frac{d}{dt} \int \vec{B}(r, t) \cdot d\vec{S} \quad (2.13)$$

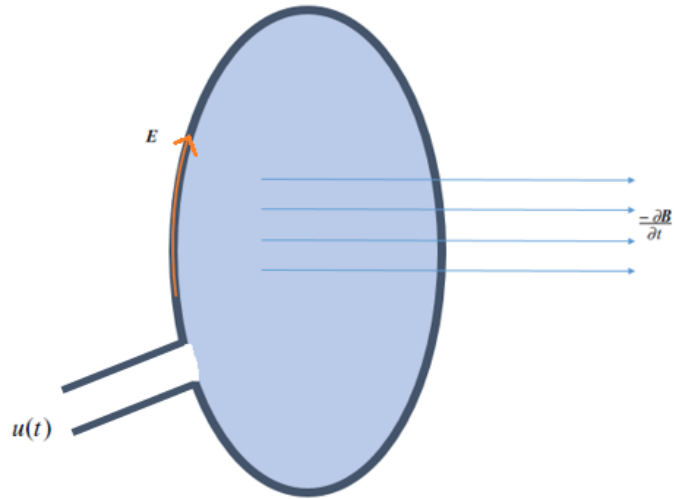


Figure 2.11: Visualization of the concepts that was described in equations (2.11), (2.12) and (2.13). E is the Electric Field through the circular coil, $\frac{\partial B}{\partial t}$ is the Magnetic Flux Density and $u(t)$ is the voltage signal induced at the ends of the coil.

In order to find the relation between the Magnetization \vec{M} and the induced signal $u(t)$, consider the fact that the magnetic flux is the curl of the magnetic vector potential, \vec{A} as given in equation (2.14).

$$\vec{B}(\vec{r}, t) = \nabla \times \vec{A}(\vec{r}, t) \quad (2.14)$$

Inserting (2.14) into (2.13) one obtains,

$$u(t) = -\frac{d}{dt} \int (\nabla \times \vec{A}(\vec{r}, t)) \cdot d\vec{S} \quad (2.15)$$

By applying the Stoke's theorem, the surface integral becomes,

$$u(t) = -\frac{d}{dt} \oint (\vec{A}(l, t)) \cdot d\vec{l} \quad (2.16)$$

Integration of (2.16) over the cross-section of a Receive coil with volume V_{coil} gives,

$$u(t) = -\frac{d}{dt} \int_{V_{coil}} \vec{A}(\vec{r}, t) \cdot \hat{j}(\vec{r}) dV_{coil} \quad (2.17)$$

where $\hat{j}(\vec{r})$ is the unit current density of the Receive coil.

Next, recalling the fact that a magnetic dipole, \vec{m}_{dipole} , would create a magnetic vector potential with the following mathematical expression,

$$\vec{A}(\vec{r}, t) = \frac{\mu_0}{4\pi} \frac{\vec{m}_{dipole}(\vec{r}, t) \times (\vec{r} - \vec{r}')}{|\vec{r} - \vec{r}'|^3} \quad (2.18)$$

Using equation (2.1), one can obtain the magnetic dipole for a small volume dV , which is

$$\vec{m}_{dipole}(\vec{r}, t) = \vec{M}_{dipole}(\vec{r}, t) dV \quad (2.19)$$

Inserting this into equation (2.18), one can find a mathematical expression that describes the total magnetic vector potential, which is created by a volume of MNPs with magnetization $\vec{M}_{dipole}(\vec{r}, t)$ as given in

$$\vec{A}(\vec{r}, t) = \frac{\mu_0}{4\pi} \int_{V_M} \frac{\vec{M}(\vec{r}, t) \times (\vec{r} - \vec{r}')}{|\vec{r} - \vec{r}'|^3} dV_M \quad (2.20)$$

where V_M is the volume of magnetic material, in other words the volume of MNPs that create the Magnetization.

Inserting (2.20) into (2.17), one should obtain

$$u(t) = -\frac{d}{dt} \int_{V_{coil}} \frac{\mu_0}{4\pi} \int_{V_M} \frac{\vec{M}(\vec{r}, t) \times (\vec{r} - \vec{r}')}{|\vec{r} - \vec{r}'|^3} dV_M \cdot \hat{j}(\vec{r}') dV_{coil} \quad (2.21)$$

Lastly, using the vector identity $\vec{A} \times \vec{B} \cdot \vec{C} = \vec{A} \cdot \vec{B} \times \vec{C}$ in equation (2.21) one should obtain

$$u(t) = -\frac{d}{dt} \mu_0 \int_{V_M} \vec{M}(\vec{r}, t) \cdot \left(\int_{V_{coil}} \frac{(\vec{r} - \vec{r}')}{4\pi|\vec{r} - \vec{r}'|^3} \times \hat{j}(\vec{r}') dV_{coil} \right) dV_M \quad (2.22)$$

Using the fact that the sensitivity $\rho(\vec{r})$ of a Receive coil with the unit current density, $\hat{j}(\vec{r})$, can be mathematically expressed as

$$\rho(\vec{r}) = \int_{V_{coil}} \frac{(\vec{r} - \vec{r}')}{4\pi|\vec{r} - \vec{r}'|^3} \times \hat{j}(\vec{r}') dV_{coil} \quad (2.23)$$

and inserting the term $\rho(\vec{r})$, into the equation (2.22) the mathematical expression that describes the relation between the induced signal and the magnetization takes the form

$$u(t) = -\frac{d}{dt} \mu_0 \int_{object} \vec{M}(\vec{r}, t) \cdot \vec{\rho}(\vec{r}) d^3r \quad (2.24)$$

2.3.4 Scanning Sequences

Choosing the convenient scanning sequence with sufficient density is important in terms of providing a good spatial resolution. In this study, two sequences were used for system acquisition and image reconstruction in a rectangular 2D FOV: Cartesian and Lissajous. FOV was planned to cover 16 mm in the z-direction and 32 mm in the y-direction, for each scanning trajectory.

The *Cartesian Trajectory* was obtained, using two drive fields in the z- and y- directions, considering to move FFP along the z-y plane. This sampling pattern requires two different sinusoidal currents with frequencies such that

$$f_y \gg \gg f_z \quad (2.25)$$

Mathematical expressions for the sinusoidal currents in each drive-coil channel can be expressed as

$$I_y(t) = I \sin(2\pi f_y t) \quad (2.26)$$

$$I_z(t) = I \sin(2\pi f_z t) \quad (2.27)$$

Here, I is the amplitude of the currents, and f_y and f_z are the channel frequencies. This sequence moves FFP rapidly in the y direction and slowly in the z direction. Illustrations for the shape of the Cartesian Trajectory and the drive field currents are given in Fig. 2.12. For this simulation, f_z was chosen to be 2.525 kHz and f_y was chosen to be fifty times bigger than of the z-direction, meaning 126.250 kHz. This means, for this simulation N_c in equation (2.28) is equal to 50.

$$\frac{f_z}{f_y} = \frac{1}{N_c} \quad (2.28)$$

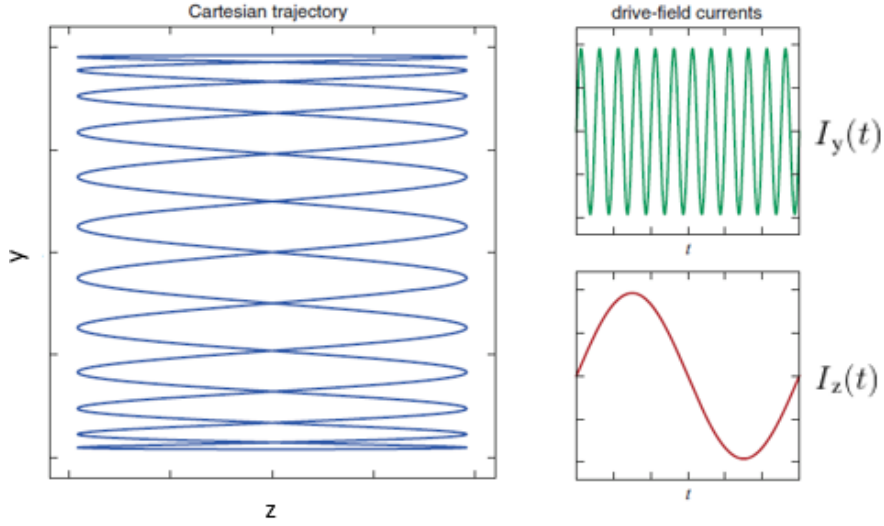


Figure 2.12: Schematic presentation for the Cartesian Trajectory [2].

Lissajous Trajectory was the second sampling pattern that was used in this study. This imaging sequence also uses sinusoidal currents with two different frequencies, but this time chosen to be similar

$$f_y \approx f_z \quad (2.29)$$

Mathematical expressions for currents are the same as given in equations (2.26) and (2.27). Generally the frequencies are chosen as

$$\frac{f_z}{f_y} = \frac{N}{N+1} \quad (2.30)$$

For this simulation the ratio between the frequencies were set to be $\frac{f_y}{f_z} = \frac{99}{98}$. For the z-direction, a frequency of $f_z = 25.25 \text{ kHz}$ was assigned and for the y-direction the resulting frequency was $f_y = 25.51 \text{ kHz}$ [12]. Illustrations for the shape of the Lissajous Trajectory and the drive field currents are given in Fig. 2.13.

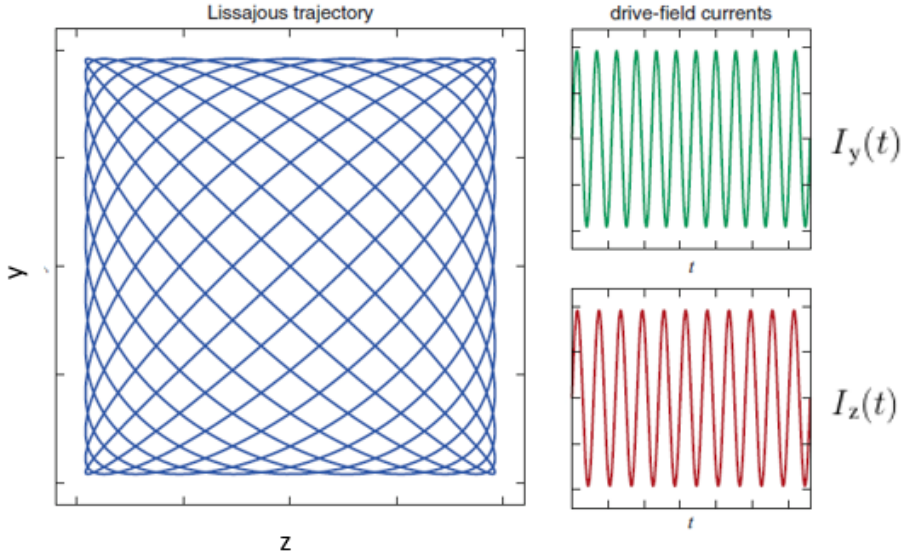


Figure 2.13: Schematic presentation for the Lissajous Trajectory [2].

In order to collect data with sufficient sampling, it is important to set the scanning duration, lasting at least one Repetition Time, T^R . Repetition Time is the interval between two complete scanning sequences, therefore one should calculate the duration for FFP to move along the whole FFP in a certain trajectory. The repetition time calculation for Cartesian and Lissajous Trajectory patterns are given below.

$$T^R_{\text{cartesian}} = \frac{N_c}{f_y} = 0.39 \text{ msec.} \quad (2.31)$$

$$T^R_{\text{lissajous}} = \frac{N + 1}{f_y} = 3.9 \text{ msec.} \quad (2.32)$$

2.3.5 System Acquisition and System Matrix

The nanoparticles that are used in this simulation were characterized with a circular shape and unit concentration. The radius for a single nanoparticle was taken as 30 nm.

2.3.5.1 Time Domain System Matrix

As the aim of the MPI is to map the distribution of MNPs in the imaging space, it can roughly be said that the 'system function' is a description of the relation between the particle distribution and the induced signal. Recalling the mathematical formulation for the Magnetization signal, which is

$$\vec{M}(\vec{r}, t) = c(\vec{r}) \vec{m}(\vec{r}, t) \quad (2.33)$$

and inserting this representation in equation (2.24), one can obtain

$$u(t) = -\mu_0 \int_{object} \vec{\rho}(\vec{r}) \cdot \frac{c(\vec{r}) \partial \vec{m}(\vec{r}, t)}{\partial t} d^3r \quad (2.34)$$

Instead of using dV_M in equation (2.24), here, d^3r is used. Without the loss of generality, in MPI systems the integral kernel of the imaging signal equation, which is the induced signal equation, is called the *System Function*. Therefore, as the last version of the equation (2.34), the signal can be expressed as

$$u(t) = \int_{object} s(\vec{r}, t) c(\vec{r}) d^3r \quad (2.35)$$

where the system function in time domain is described as

$$s(\vec{r}, t) = -\mu_0 \vec{\rho}(\vec{r}) \cdot \frac{\partial \vec{m}(\vec{r}, t)}{\partial t} \quad (2.36)$$

In this case, \vec{r} is the position vector in the imaging space, representing an arbitrary pixel, defined in FOV.

In this study, above equations (2.35) and (2.36) were discretized to obtain a 2-D simulation model. The FOV was set to cover 16mm in the z-direction and 32 mm in the y-direction and this range was defined with $64 \times 32 = 2048$ pixels in the simulation. The discretized equation for the induced signal can be written as follows:

$$u_t = \sum_{j=1}^{64} \sum_{k=1}^{32} s_{t,j,k} c_{j,k} \quad (2.37)$$

Where u_t is the discretized form of induced signal, $s_{t,j,k}$ is the discretized form of system function and $c_{j,k}$ is the discretized form of particle concentration. In this equation, t represents the index for the time instance, j represents the index of the y-position and k represents the index of the z-position in FOV. This equation can also be written using single summation as

$$u_t = \sum_{i=1}^{2048} s_{t,i} c_i \quad (2.38)$$

where i denotes the pixel number in the FOV. Therefore, in discrete form, one can obtain a set of linear equations in the form:

$$\begin{aligned} u_1 &= s_{1,1} c_1 + s_{1,2} c_2 + \cdots + s_{1,2048} c_{2048} \\ u_2 &= s_{2,1} c_1 + s_{2,2} c_2 + \cdots + s_{2,2048} c_{2048} \\ &\vdots \\ u_n &= s_{n,1} c_1 + s_{n,2} c_2 + \cdots + s_{n,2048} c_{2048} \end{aligned} \quad (2.39)$$

This set of linear equations can be represented by using the following matrix equation form:

$$\begin{bmatrix} s_{1,1} & s_{1,2} & \cdots & \cdots & s_{1,2048} \\ s_{2,1} & \cdots & \cdots & \cdots & s_{2,2048} \\ s_{3,1} & \cdots & \cdots & \cdots & s_{3,2048} \\ \vdots & \vdots & \vdots & \vdots & \vdots \\ s_{k,1} & \cdots & \cdots & \cdots & s_{k,2048} \end{bmatrix} \times \begin{bmatrix} c_1 \\ c_2 \\ c_3 \\ \vdots \\ c_{2048} \end{bmatrix} = \begin{bmatrix} u_1 \\ u_2 \\ u_3 \\ \vdots \\ u_k \end{bmatrix} \quad (2.40)$$

which can also be written as

$$\underline{\underline{S}} \underline{c} = \underline{u} \quad (2.41)$$

In equation (2.41), $\underline{\underline{S}}$ is the system matrix that defines the relation between the system excitations and tracer behaviour. In the simulation, it was obtained by changing the position of a single volume element with unit concentration, pixel by pixel, until the whole imaging area was scanned and each pixel-response was stored in a matrix. The imaging area was defined with 2048 pixels in total, hence, acquisition was done by processing a complete scan for 2048 pixels separately. In this study, the system matrix has the following form:

$$S = \begin{bmatrix} s_{1,1} & s_{1,2} & s_{1,3} & \dots & s_{1,2048} \\ s_{2,1} & \dots & \dots & \dots & s_{2,2048} \\ s_{3,1} & \dots & \dots & \dots & s_{3,2048} \\ \vdots & \vdots & \vdots & \vdots & \vdots \\ s_{77601,1} & \dots & \dots & \dots & s_{77601,2048} \end{bmatrix} \quad (2.42)$$

In (2.42), columns of S represent the pixels and rows represent each time instance in a complete scan. This means that, system response of each pixel was stored as a column vector while obtaining the system matrix. Scanning duration was chosen to be $T_{scan} = 3.9$ msec and $f_s = 20$ MHz sampling frequency was used. Both for Lissajous and Cartesian Trajectory, the number of data points, N_{data} , in one scan for each pixel can be found as:

$$N_{data} = T_{scan} \cdot f_s = 77601 \quad (2.43)$$

As there were 2048 pixels in the image frame in this simulation, the dimension of the system matrix is 77601×2048 .

For further analysis of the System Matrix, Singular Value Decomposition (SVD) can be applied in order to obtain a factorization of the $\underline{\underline{S}}$ matrix, in the form

$$\underline{\underline{S}} = \underline{\underline{M}} \underline{\underline{\Sigma}} \underline{\underline{V}}^T = \sum_{i=1}^{2048} m_i \sigma_i v_i^T \quad (2.44)$$

In this decomposition, $\underline{\underline{M}}$ matrix consists of 2048 orthonormalized eigenvectors associated with the 2048 largest eigenvalues of $\underline{\underline{S}}^T \underline{\underline{S}}$, and $\underline{\underline{V}}$ matrix consists the same information of $\underline{\underline{S}} \underline{\underline{S}}^T$ [14]. Additionally, m_i are the column vectors of the matrix $\underline{\underline{M}}$ and v_i are the same for $\underline{\underline{V}}$. The columns of $\underline{\underline{M}}$ are called the left singular vectors and the columns of $\underline{\underline{V}}$ are called the right singular vectors. In equation (2.44), $\underline{\underline{\Sigma}}$ is a diagonal matrix with diagonal entries

$$\sigma_1 \geq \sigma_2 \geq \dots \geq \sigma_{2048} \geq 0 \quad (2.45)$$

which are the non-negative square roots of the eigenvalues of $\underline{\underline{S}}^T \underline{\underline{S}}$ and are called *singular values*.

It was explained that the aim of MPI is to map the MNP distribution in the imaging space and the system is defined with the matrix equation given in equation (2.41). This equation can be solved as an inverse matrix problem. The MNP distribution, which is vector $\underline{\underline{c}}$, can be found with the classical approach, which is the left-multiplication of each side with the equation inverse of $\underline{\underline{S}}$ in (2.41). If the system matrix was full rank, square matrix, then it could also be invertible. Here in this case, $\underline{\underline{S}}$ is not invertible. Therefore, SVD analysis was performed to solve the equation (2.41) in the form

$$\underline{\underline{c}} = \underline{\underline{S}}^{-1} \underline{\underline{u}} \quad (2.46)$$

Inserting (2.44) into (2.46) would give

$$\underline{\underline{c}} = \sum_{i=1}^{2048} \frac{m_i^T \underline{\underline{u}}}{\sigma_i} v_i \quad (2.47)$$

While doing the SVD analysis, one can obtain information about the sensitivity distribution of the system. It can be said that, in equation (2.47), \underline{v}_i are image basis vectors, each corresponding to a singular value σ_i . Image basis vectors that correspond to higher singular values would show areas where the imaging system is more sensitive. The sorted singular values are given in figures 2.14 and 2.15.

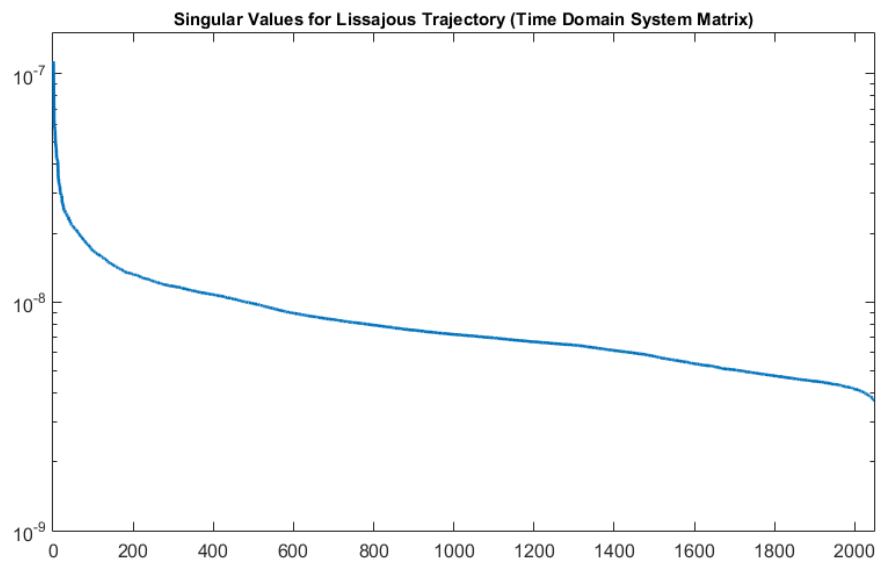


Figure 2.14: Sorted singular values for the system matrix that obtained from Lissajous Trajectory. Maximum and minimum values are 1.133×10^{-7} and 3.729×10^{-9} respectively. The condition number is then found to be approximately 30.38.

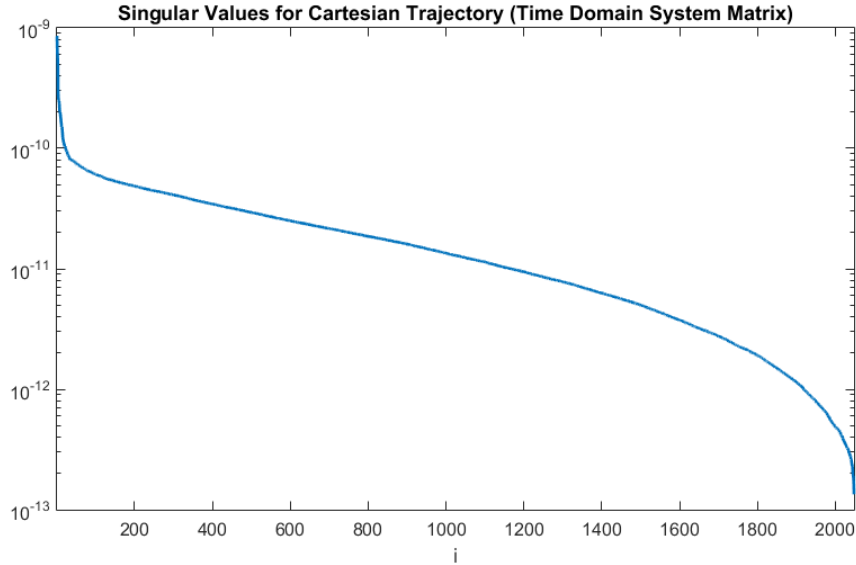


Figure 2.15: Sorted singular values for the system matrix that obtained from Cartesian Trajectory. Maximum and minimum values are 8.588×10^{-10} and 1.342×10^{-13} respectively. The condition number is then found to be 6.3979×10^3 .

The condition number measures the sensitivity of the solution of a problem to perturbations in the data. It can also be used to predict the convergence of iterative methods [15]. The higher condition number a matrix has, the more ill-conditioned it gets. Therefore, an ill-conditioned matrix can generate huge errors while approximating the solution. Examining the condition numbers found for this imaging system, it can be seen that especially for Cartesian Trajectory, if no regulations were applied, iterative image reconstruction methods would give large errors. This could be a result of the characteristics of the Cartesian Trajectory, as one drive field frequency is much more larger than the other one, scanning in the direction of the lower frequency is much more slower. Therefore, information gathered in one direction during one scan is always less than the information gathered in the other direction. This may result in a more ill-conditioned system matrix with a higher condition number.

While performing the SVD analysis for the imaging system, both for Lissajous and the Cartesian Trajectories, a combination of two system matrices that were obtained from the Drive Field channels z and y were combined. Aiming to provide computational simplicity, matrix entries were decomposed to their real and imaginary parts, and sorted as real and imaginary parts in the system matrix. Then, without changing

this structure, two matrices from the z and y channels were combined together, end-wise, resulting in a single System Matrix. SVD analysis was made to the resultant System Matrices. Figures 2.16 and 2.17 show SVD analysis results for Lissajous and Cartesian Trajectories, respectively.

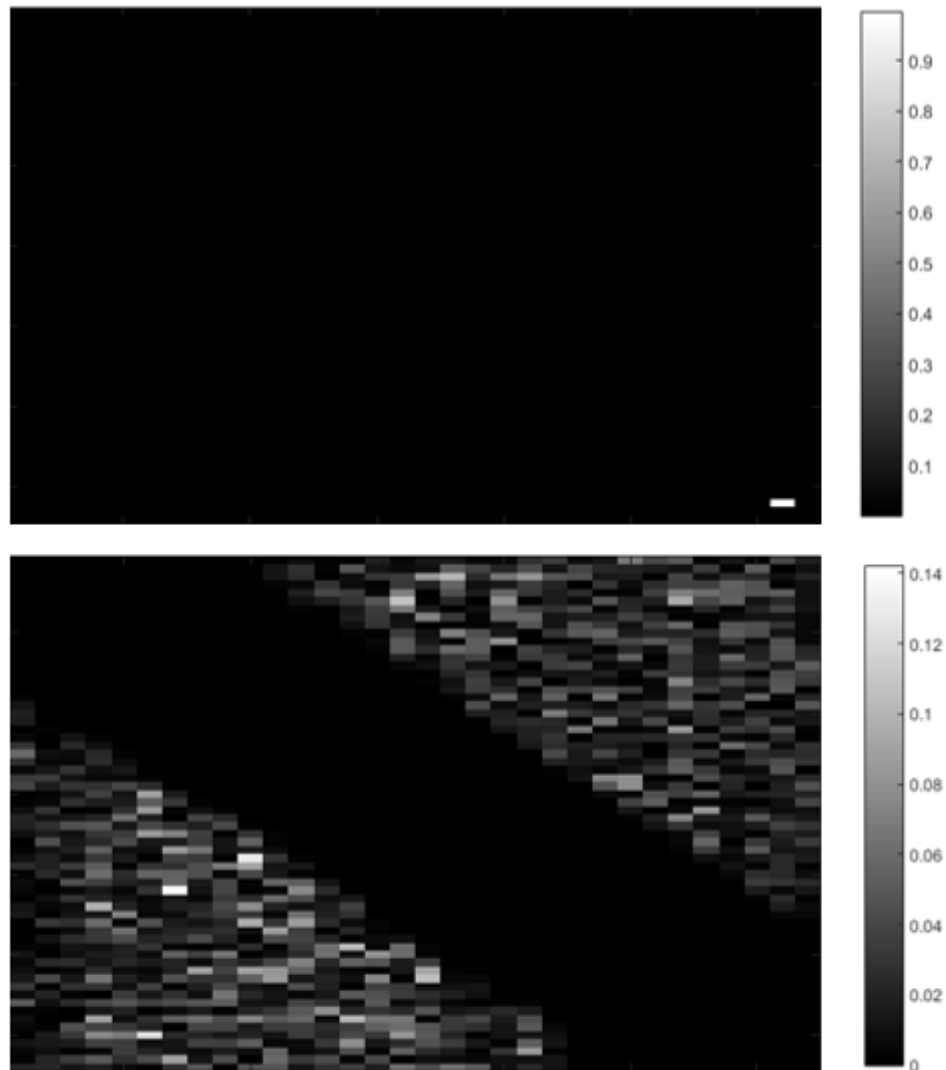


Figure 2.16: Image basis vectors transformed to 2D image that correspond maximum (upper) and minimum (lower) singular values that are obtained from Lissajous Scanning.

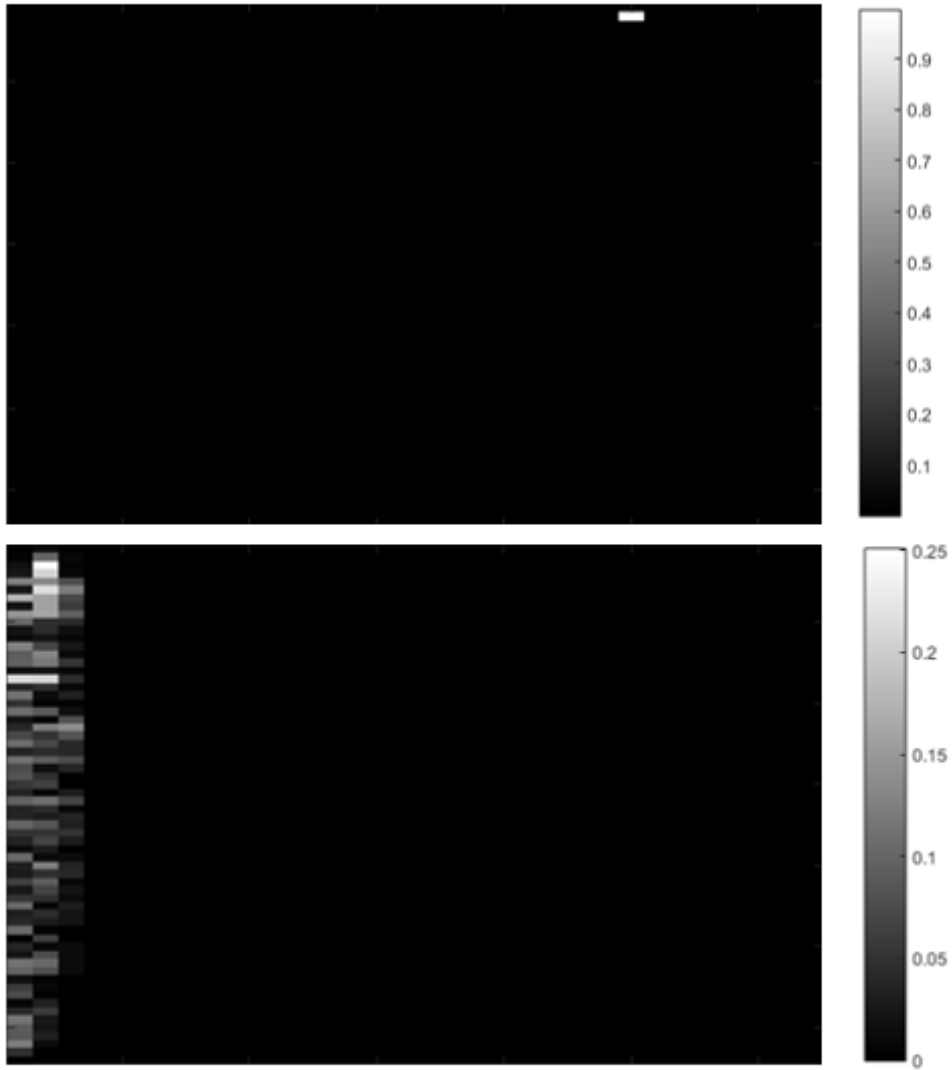


Figure 2.17: Image basis vectors transformed to 2D image that correspond maximum (upper) and minimum (lower) singular values that are obtained from Cartesian Scanning.

2.3.5.2 Frequency Domain System Matrix

Reminding that there were two different receiver channels, z and y receive coils, in this system, one can conclude that there will be two separate system matrices with 77601×2048 dimension and two different signals that are recorded. In computational basis, it would be hard and inefficient to work with such big matrices. Luckily, when the system is examined in frequency domain it can be seen that the energy of the signals are accumulated at certain frequencies, mostly at the harmonics, and it decreases with the increasing frequency [16] as it can be seen in figures 2.19 and 2.20. Consequently, one can convert the time-domain system matrix into frequency domain and filter out the frequency components that have energy values below average. Aiming this, the time domain signals for each position of the sample, which are actually columns of the system matrix, are converted to frequency domain, using fast fourier transform and frequencies that correspond to lower energy values were filtered out, like it is illustrated in Fig. 2.18.

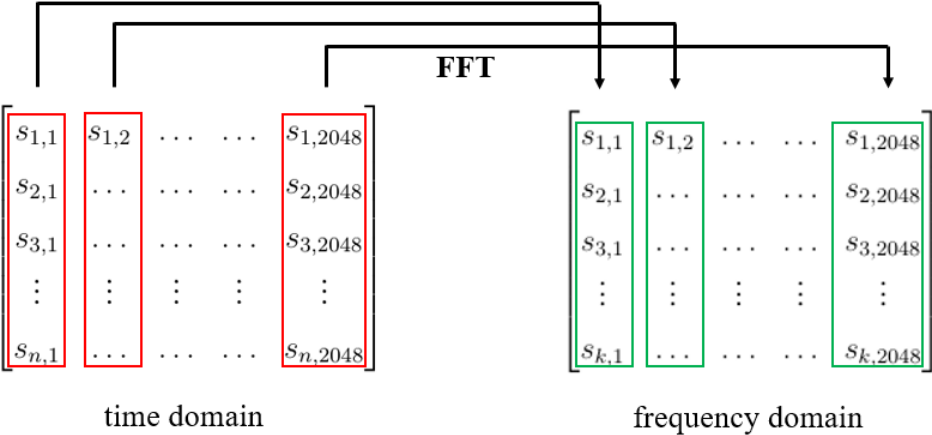


Figure 2.18: Schematic illustration explaining the frequency domain conversion of a system matrix.

The mathematical expression for the energy of the system function in frequency-domain, $s_k(r)$, is given as:

$$w_k := \sqrt{\int_{object} |s_k(r)|^2 d^3r} \quad (2.48)$$

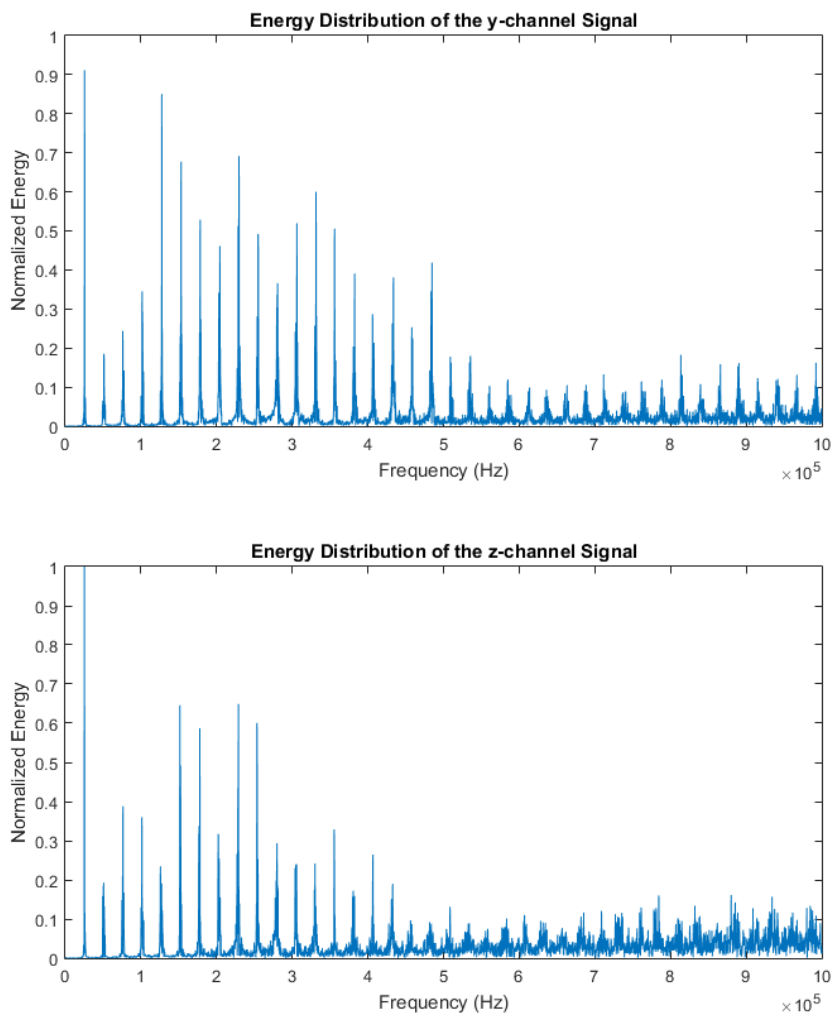


Figure 2.19: Energy distribution of y and z- channel system functions for frequencies between 0 to 1000 kHz, that was obtained from Lissajous Scanning. It can be seen that the energy is dominant at harmonic frequencies.

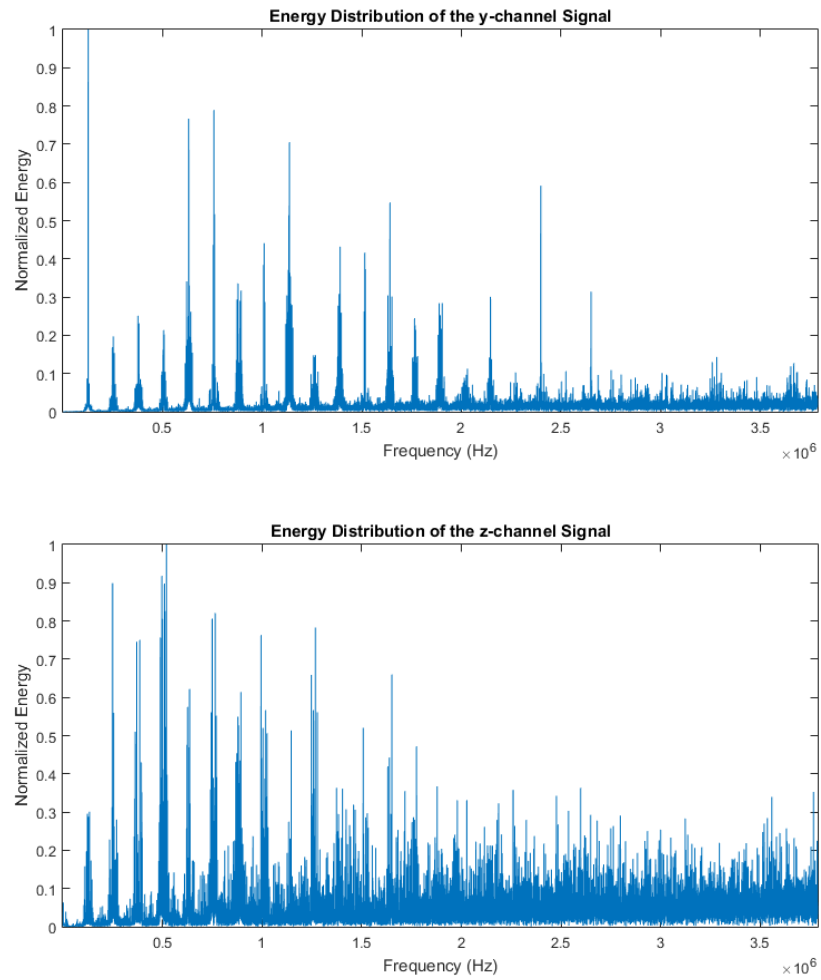


Figure 2.20: Energy distribution of y and z- channel system functions for frequencies between 0 to 4000 kHz, that was obtained from Cartesian Scanning. It can be seen that the energy is dominant at harmonic frequencies.

SVD analysis in frequency domain has the same steps as in time domain except that after obtaining system matrices in frequency domain and examining the energy distribution, a 'cut frequency' was chosen to downsize each matrix by truncating it and filter out the low energy part of the system matrix, as it was explained before. Figures 2.21 and 2.22 show sorted singular values, and 2.23 and 2.24 show SVD analysis results for Lissajous and Cartesian Trajectories, respectively. The matrix condition numbers differ from those were obtained in the time-domain case, as the matrices are downsized in frequency domain.

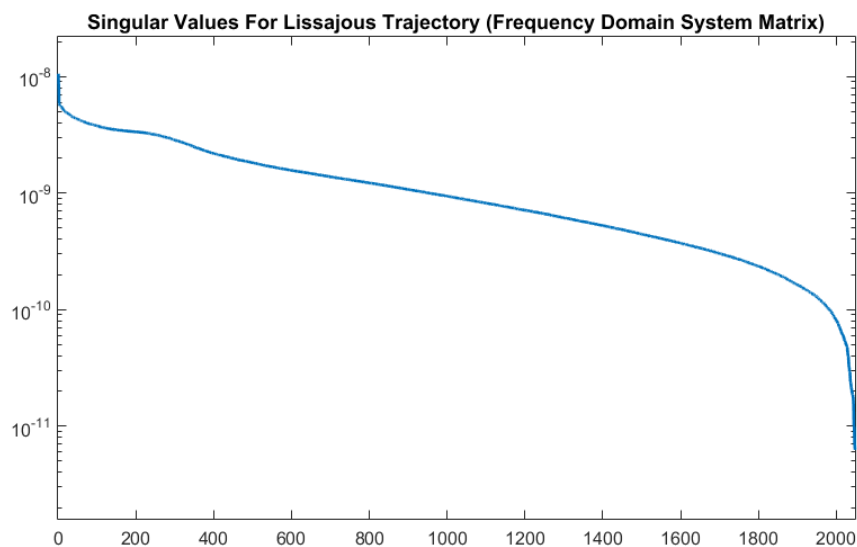


Figure 2.21: Sorted singular values for the system matrix that obtained from Lissajous Trajectory. Maximum and minimum values are 1.057×10^{-8} and 6.24×10^{-12} respectively. The condition number is then found to be approximately 1.69×10^3 .

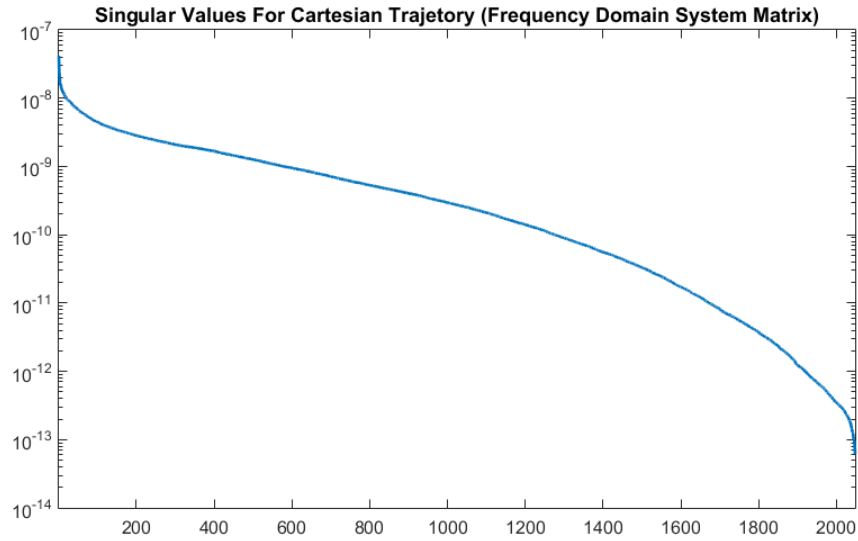


Figure 2.22: Sorted singular values for the system matrix that obtained from Cartesian Trajectory. Maximum and minimum values are 4.196×10^{-8} and 6.121×10^{-14} respectively. The condition number is then found to be approximately 6.855×10^5 .

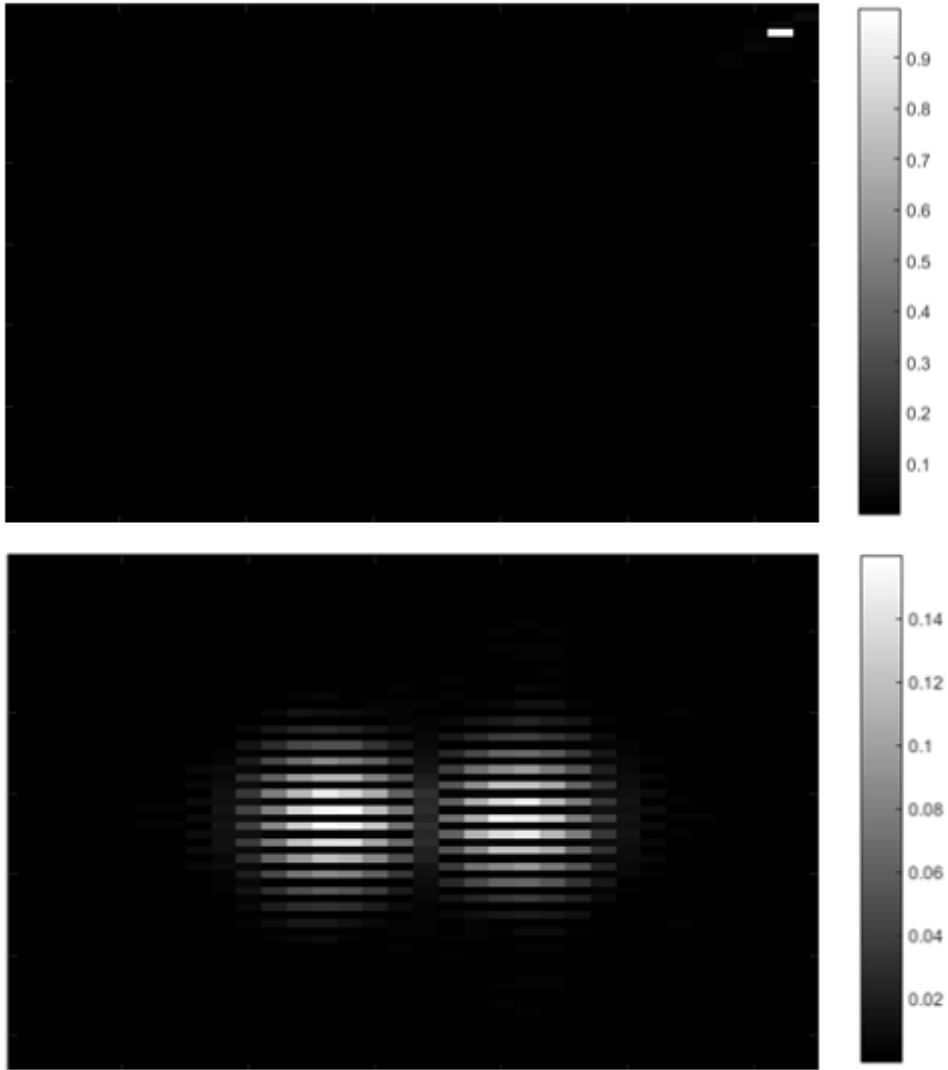


Figure 2.23: Image basis vectors transformed to 2D image that correspond maximum (upper) and minimum (lower) singular values that are obtained from Lissajous Scanning.

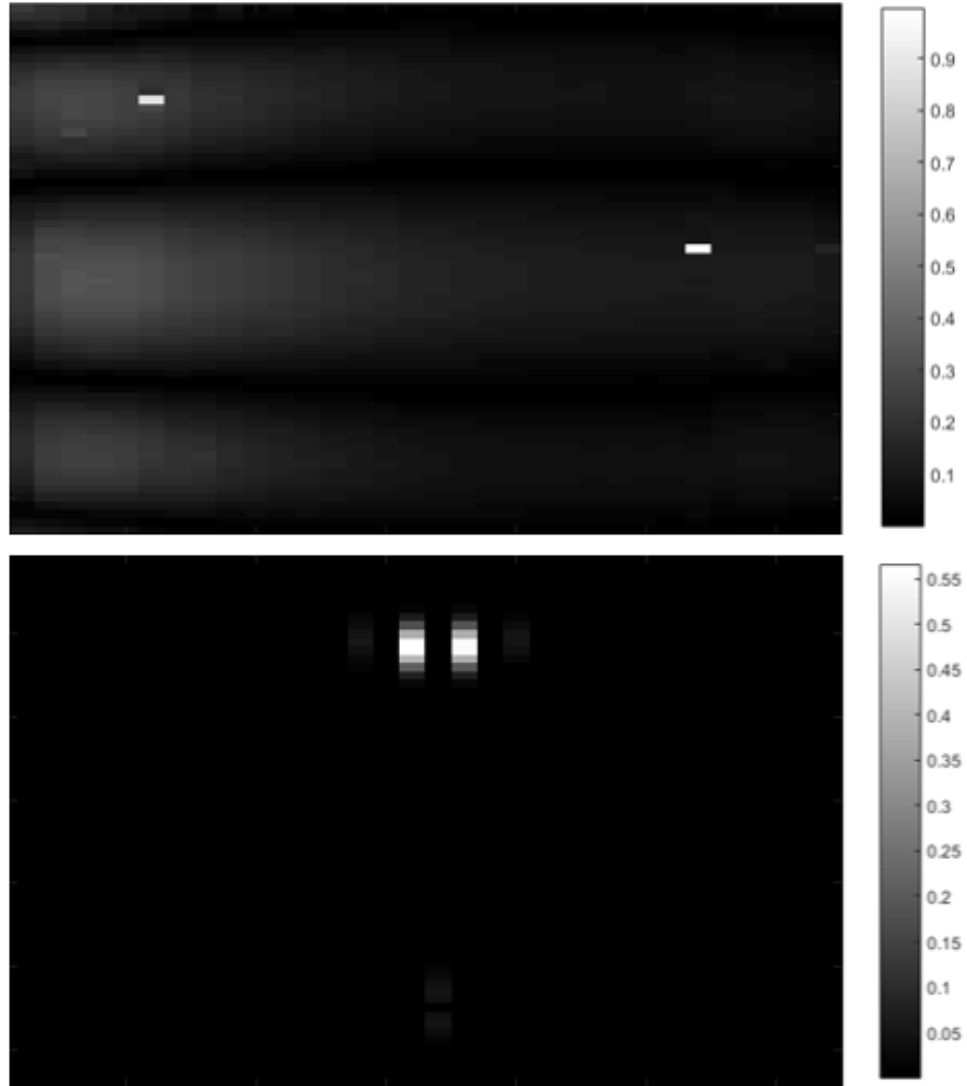


Figure 2.24: Image basis vectors transformed to 2D image that correspond maximum (upper) and minimum (lower) singular values that are obtained from Cartesian Scanning.

For further analysis on the system, spatial structure of the System Matrix can be interpreted for each scanning trajectory. Following figures, 2.25, 2.26, 2.27 and 2.28 show six different harmonic frequency components for each of 2D system functions, one coming from the y-direction Drive Field Channel and the other is from the z-direction Drive Field Channel. Spatial Frequency components were sorted according to their frequency values, f_t , which can be represented as $f_t = k\Delta f$. In this simulation, Δf was set to be approximately 257.7 Hz. The aim of analyzing the spatial

frequency pattern of system matrices is to understand the spatial sensitivity distribution of a specific frequency component. In each figure, first six harmonic components were shown and lighter areas indicate higher sensitivity. It can also be seen that the resolution increases with the increase in the order of the harmonics. This information provides the intuition that the more harmonics included in the system matrix the higher the resolution of the reconstructed image is.

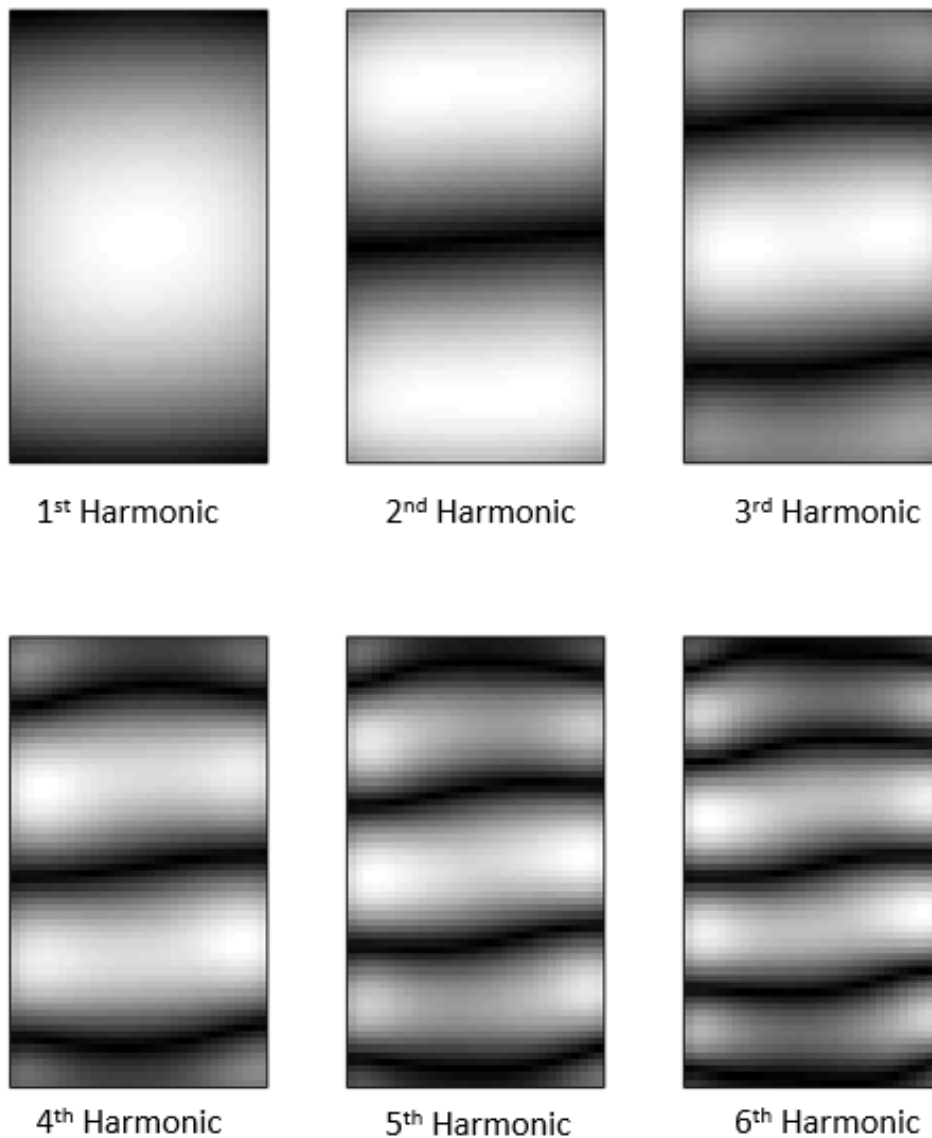


Figure 2.25: Spatial Frequencies for y-channel System Matrix that is obtained from Lissajous Trajectory scan.

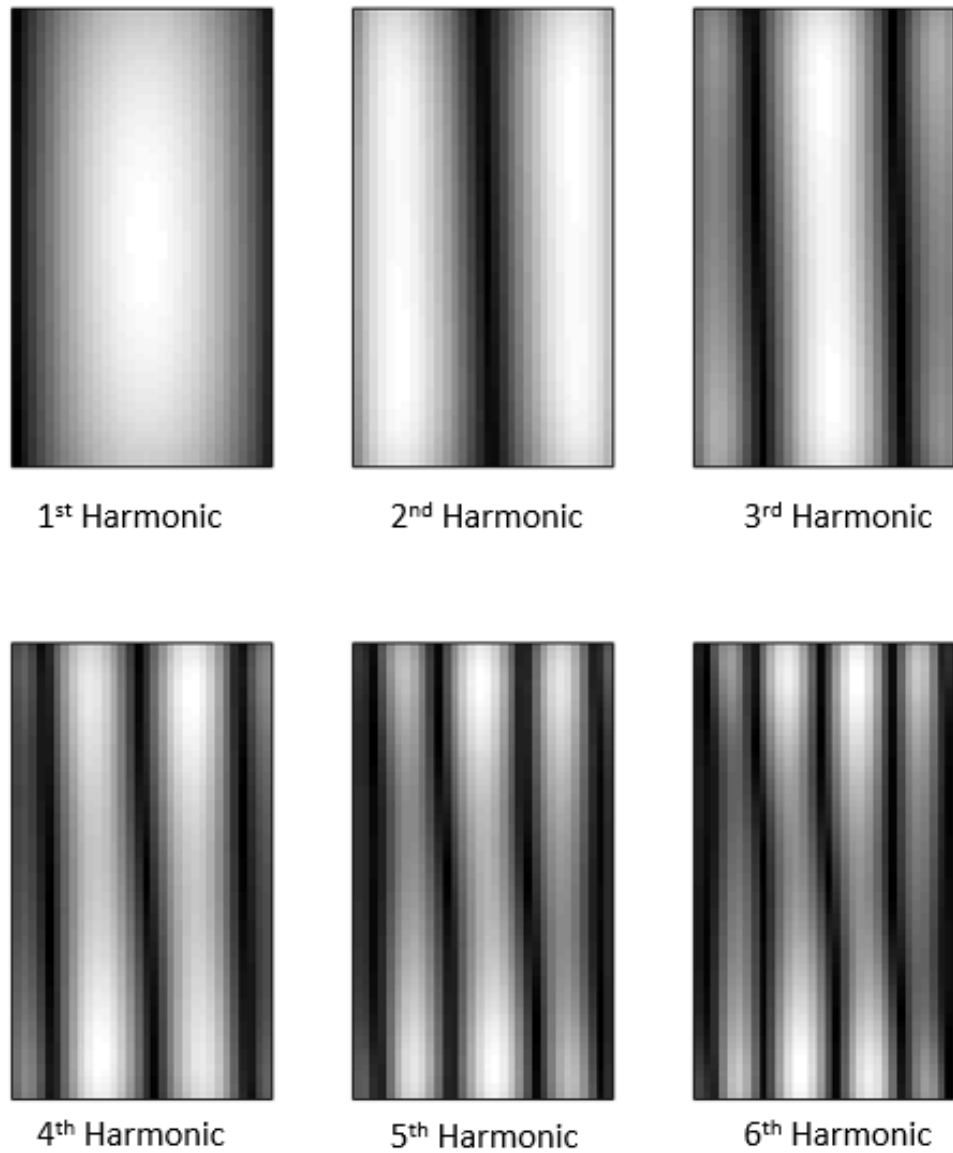


Figure 2.26: Spatial Frequencies for z-channel System Matrix that is obtained from Lissajous Trajectory scan.

In reconstruction, using higher harmonics of the system matrices and the recorded signals should provide higher resolutions. The trade off between the computational simplicity and good resolution can be optimized using the frequency domain energy distribution, as it was explained previously in this section. One can decide on a truncation harmonic frequency by examining the energy distributions, and downsizing the system matrices and the recorded signals. Spatial Frequency distributions of Cartesian Trajectory are further given below.

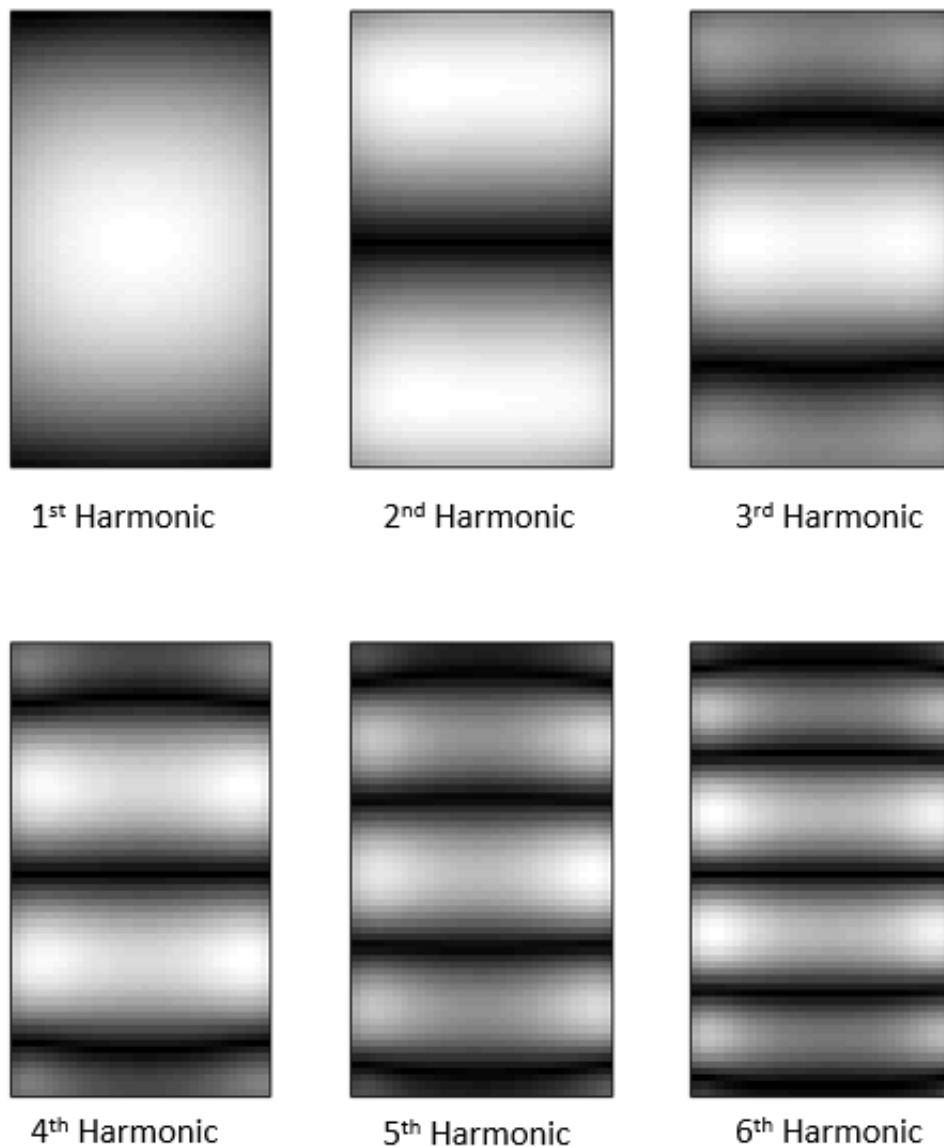


Figure 2.27: Spatial Frequencies for y-channel System Matrix that is obtained from Cartesian Trajectory scan.

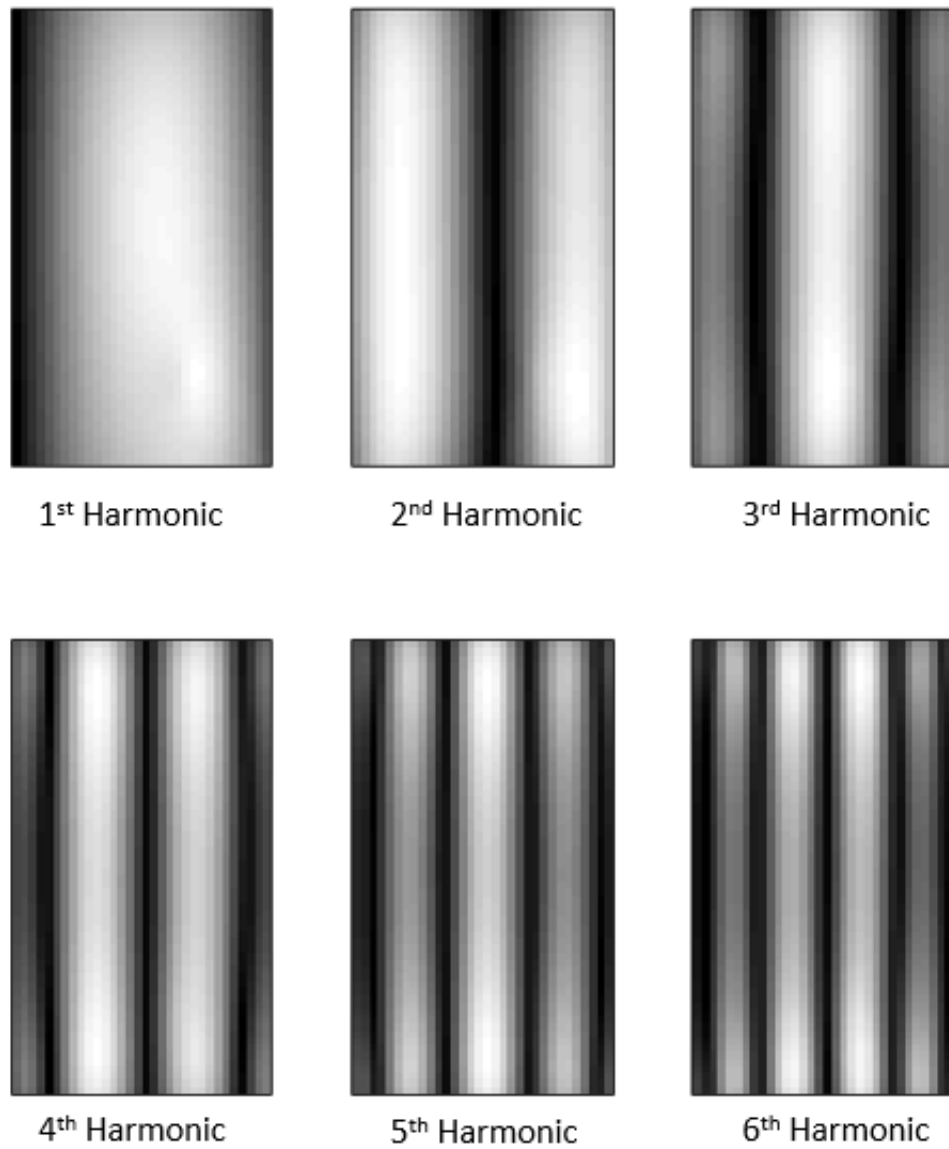


Figure 2.28: Spatial Frequencies for z-channel System Matrix that is obtained from Cartesian Trajectory scan.

2.4 Image Reconstruction

2.4.1 Introduction

One of the MPI techniques that had been presented in literature is the x-space MPI. This technique enables the reconstruction of a *native* MPI image, without using a system function, harmonics, or pre-characterization of the nanoparticles or imager [10]. X-space reconstruction method uses the fact that if the Selection Field has a constant spatial distribution and Drive Field is uniform in the imaging space, then the concentric distribution of MNP inside the FFP is proportional to the induced signal over the FFP scanning velocity. This method is accepted to be a simpler method than the *system matrix reconstruction* method, but it but it requires the knowledge of the FFP exact position and velocity at each time step of the scanning process [17].

Iterative methods are also commonly used in System Matrix image reconstruction for MPI. Likewise for choosing the scanning trajectory, utilization of the effective reconstruction technique is crucial. In this study, three different image reconstruction algorithms were used: Algebraic Reconstruction Technique, Selective Singular Value Decomposition Method and Truncated Singular Value Decomposition Method.

The following matrix notation was used for 2D image reconstruction:

$$\underline{S} \underline{c} = \underline{u} \quad (2.49)$$

2.4.2 Reconstruction Techniques

2.4.2.1 Algebraic Reconstruction Technique

Algebraic Reconstruction Technique is an iterative algorithm that was introduced by Gordon et al. [18] for solving the problem of three dimensional reconstruction from projections in electron microscopy and radiology [19][20]. In 2.49, the values of the each pixel, meaning the particle distribution data, were stored in the vector \underline{c} , \underline{S} is the System Matrix and \underline{u} is the signal received.

The computational procedure in ART starts with assigning an initial guess to the unknown, which was the particle distribution in the simulation. Then, by using the following update equation, the algorithm computes an approximate solution for the system, in order to find \underline{c} .

$$c^{l+1} = c^l + \frac{u_j - s_j \cdot c^l}{\|s_j\|^2} \tag{2.50}$$

where $j = l \bmod (M + 1)$, s_j is the j^{th} row of the matrix S and u_j is the j^{th} entry of the signal vector, u . As an index for iteration, l was used in the notation. The idea behind this technique can be explained as illustrated in Fig. 2.29.

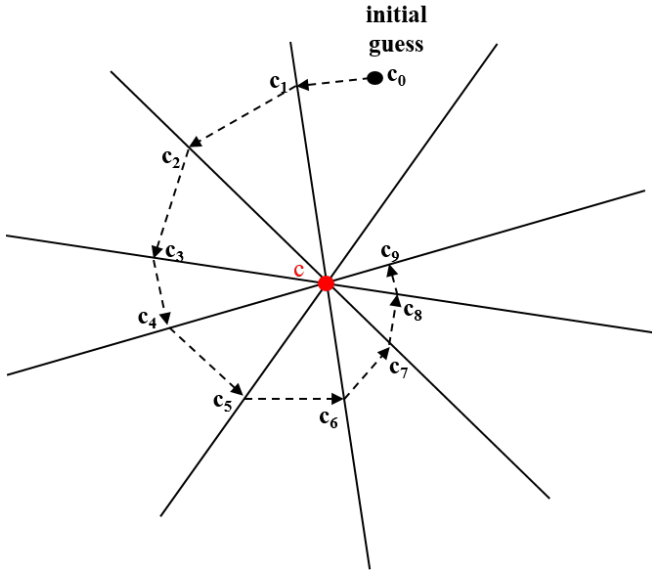


Figure 2.29: Illustrative explanation for the idea behind ART. c_0 is the initial guess and c_i are the projections on the line equations of the system, which are updated by using equation (2.50). c is the actual particle distribution that is aimed to be approximated by using this method.

2.4.2.2 Least Squares Approach

This method aims to solve the system matrix equation by left-multiplication of each-side with the inverse of the system matrix. In order to obtain an invertible matrix out of the system matrix, $\underline{\underline{S}}$ was multiplied with its Hermitian which is the conjugate transpose of itself. Therefore, the system equation takes the form

$$\underline{\underline{S}}^H \underline{\underline{S}} \underline{\underline{c}} = \underline{\underline{S}}^H \underline{\underline{u}} \quad (2.51)$$

For simplicity, a new notation can be used for the above equation

$$\underline{\underline{A}} \underline{\underline{c}} = \underline{\underline{b}} \quad (2.52)$$

where $\underline{\underline{A}} = \underline{\underline{S}}^H \underline{\underline{S}}$ and $\underline{\underline{b}} = \underline{\underline{S}}^H \underline{\underline{u}}$. Obtained new equation, (2.52), can now be solved as an inverse matrix problem, where $\underline{\underline{A}}$ becomes the new system matrix that can be decomposed as follows

$$\underline{\underline{A}} = \underline{\underline{U}} \underline{\underline{\Sigma}} \underline{\underline{V}}^T = \sum_{i=1}^{2048} \underline{\underline{u}}_i \sigma_i \underline{\underline{v}}_i^T \quad (2.53)$$

Here, $\underline{\underline{u}}_i$ are the column vectors of the matrix $\underline{\underline{U}}$ and $\underline{\underline{v}}_i$ are the same for $\underline{\underline{V}}$. Inserting equation (2.53) into (2.52) will give

$$\underline{\underline{c}} = \underline{\underline{A}}^{-1} \underline{\underline{b}} = \sum_{i=1}^{2048} \frac{\underline{\underline{u}}_i^T \underline{\underline{b}}}{\sigma_i} \underline{\underline{v}}_i \quad (2.54)$$

which gives $\underline{\underline{c}}$, the MNP concentration distribution in the imaging space. Examining the summation in the right hand side of the equation, one can conclude that $\underline{\underline{v}}_i$ vectors can be considered as the image basis vectors, each correspond to a different singular value σ_i . The basis vectors that correspond to smaller singular values would be dominant in reconstructing the image, as the coefficient $\frac{\underline{\underline{u}}_i^T \underline{\underline{b}}}{\sigma_i}$ would increase, therefore during the reconstruction process, $\underline{\underline{v}}_i$ vectors that correspond to smaller σ_i can be truncated as a regulation.

There are two commonly used methods in order to regulate the effect of noisy SVD components. First one is the *Selective SVD (SSVD) Method*, which chooses to include SVD components, which are consistent with the system and each other, not as small as the noisy level [21]. In this study, a threshold value was chosen according to the Picard plot, that will be explained in the next section.

Second method is the *Truncated SVD (TSVD) Method*. Likewise in Selective SVD Method, the aim of TSVD is to eliminate the negative effect of noisy SVD components. In order to do so, in TSVD, components that correspond to larger singular values were included. This means to 'truncate' SVD components at a certain value [21].

The mathematical expressions of the solution for SSVD method is

$$\underline{x} = \underline{\underline{A}}^{-1} \underline{b} = \sum_{|\underline{u}_i^T \underline{b}| > k_s} \frac{\underline{u}_i^T \underline{b}}{\sigma_i} \underline{v}_i \quad (2.55)$$

The mathematical expressions of the solution for TSVD method is

$$\underline{x} = \underline{\underline{A}}^{-1} \underline{b} = \sum_{i=1}^{k_t} \frac{\underline{u}_i^T \underline{b}}{\sigma_i} \underline{v}_i \quad (2.56)$$

2.5 Results and Conclusions

In order to test the system performance, a phantom was created as in Fig 2.30. Then, System Matrix reconstruction techniques were applied both with and without noise effects. Results are given in figures 2.31, 2.32, 2.34, 2.35, 2.36 and 2.37

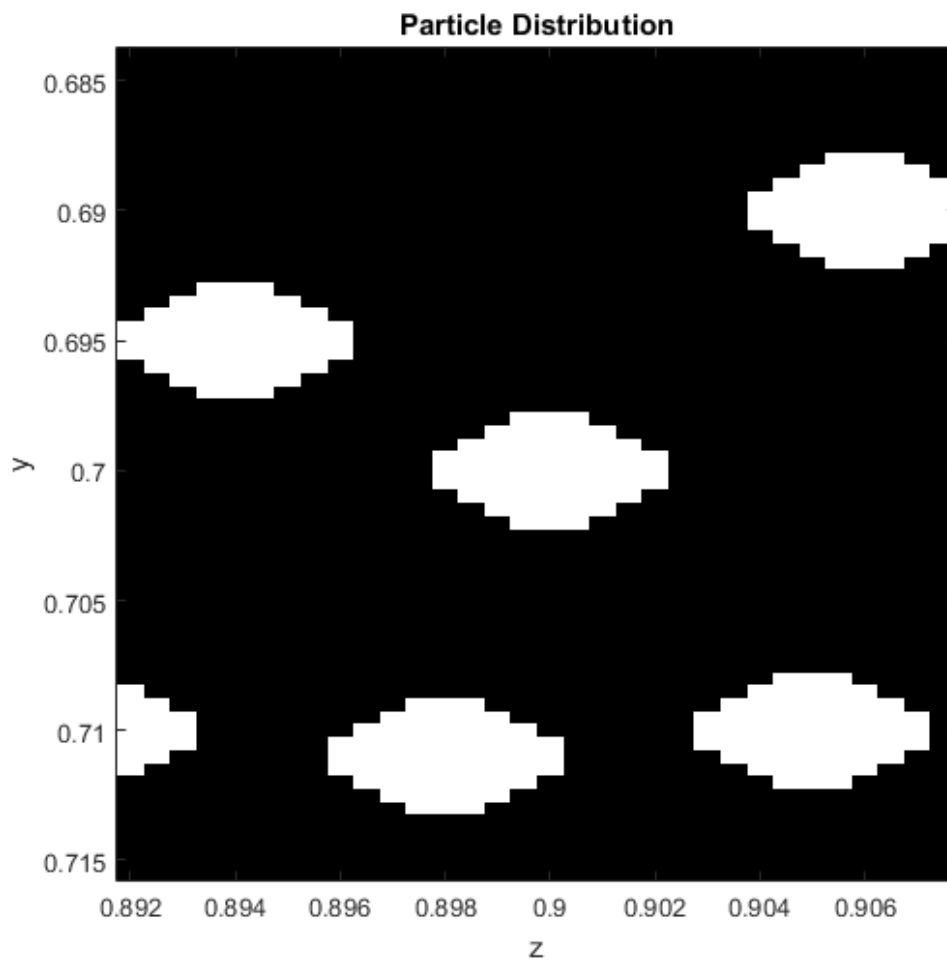


Figure 2.30: 2D cross-section of the particle distribution that had been used as the *phantom* in this simulation. For simplicity, magnetic core concentration for all nanoparticles in this distribution of the phantom was chosen to be equal..

The results were compared using Peak Signal-to-Noise Ratio (PSNR) which gives the ratio between the maximum possible value of the original signal, which is the particle distribution in this case and the power of the disrupting noise. PSNR value can be calculated by using the Mean Square Error (MSE), formulated as

$$MSE = \frac{1}{2048} \sum_{j=1}^{64} \sum_{k=1}^{32} [I(j, k) - R(j, k)]^2 \quad (2.57)$$

where j and k are indices in the imaging space, I is the original image matrix and R is the reconstructed image matrix. Then by using MSE, PSNR value can be found as

$$PSNR = 10 \log_{10} \left(\frac{MAX_I^2}{MSE} \right) \quad (2.58)$$

where MAX_I is the maximum pixel value of the original image.

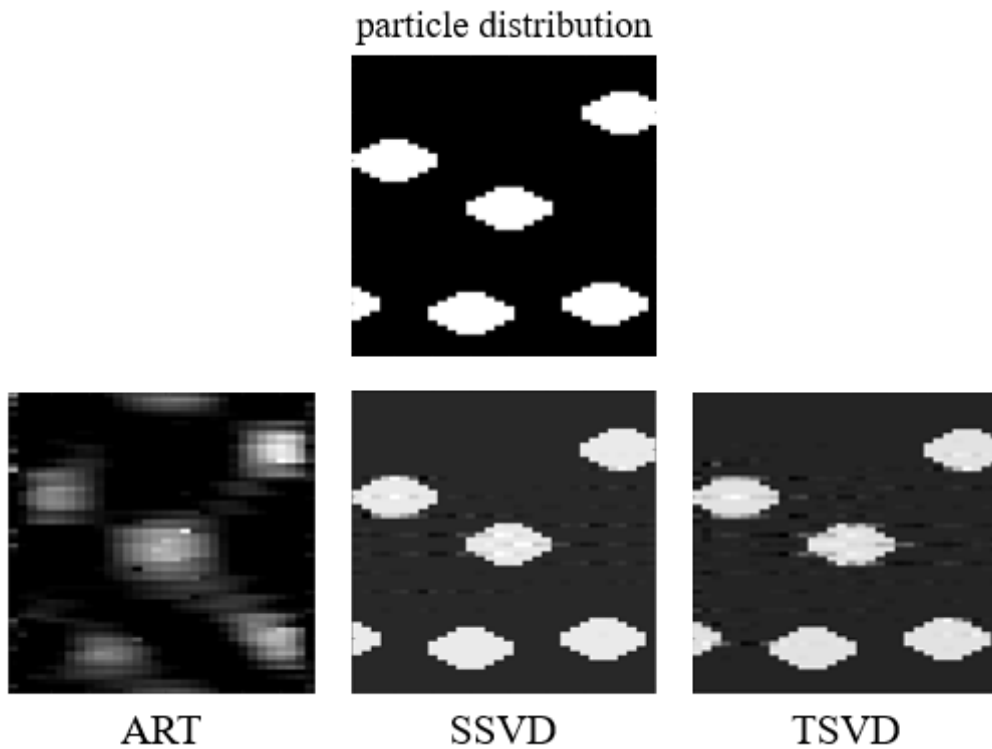


Figure 2.31: Results for Cartesian Scanning Trajectory, without any additional noise. PSNR values for ART, SSVD and TSVD are 9.23, 54.31, 47.68 respectively.

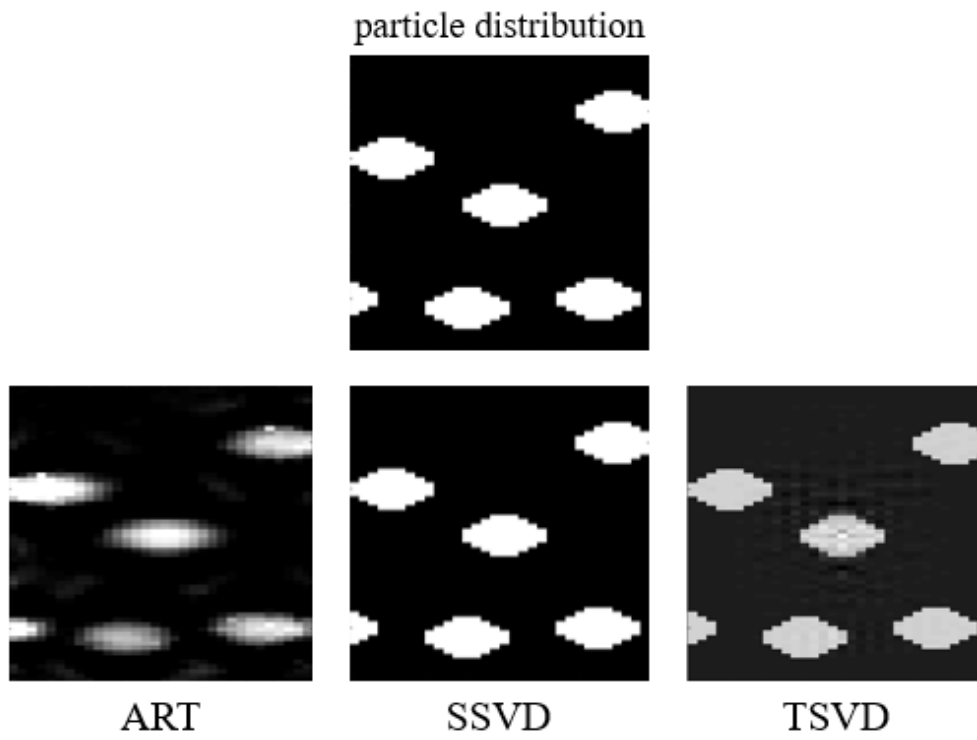


Figure 2.32: Results for Lissajous Scanning Trajectory, without any additional noise. PSNR values for ART, SSVD and TSVD are 8.38, 283.55, 57.95 respectively.

Noise addition was made by using MATLAB function 'awgn', which generates random numbers with Gaussian distribution. This function calculates the variance for the Gaussian distribution as the noise power, with the desired SNR value, using the original signal. In this model, SNR values were compared to realistic data that are presented in Buzug et al.[3].

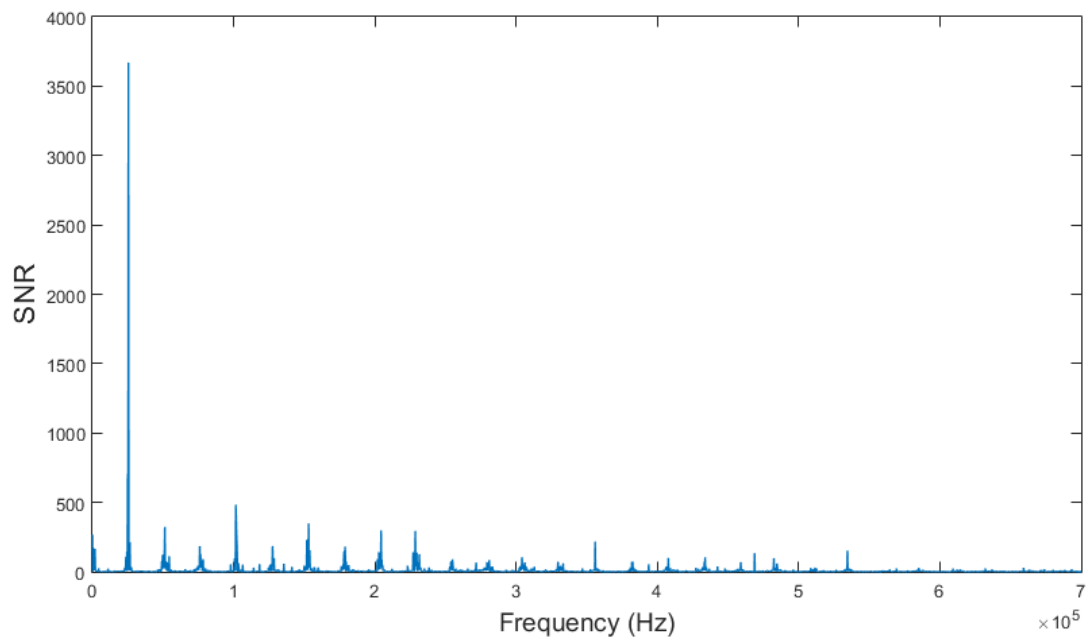


Figure 2.33: SNR values for different frequencies. Maximum SNR value is found to be approximately 34 dB and it can be seen that SNR value increases at signal harmonics. Comparing these results with experimental data given in [3], it can be concluded that 34 dB SNR level is acceptable as 40dB SNR was observed experimentally for 200 averages.

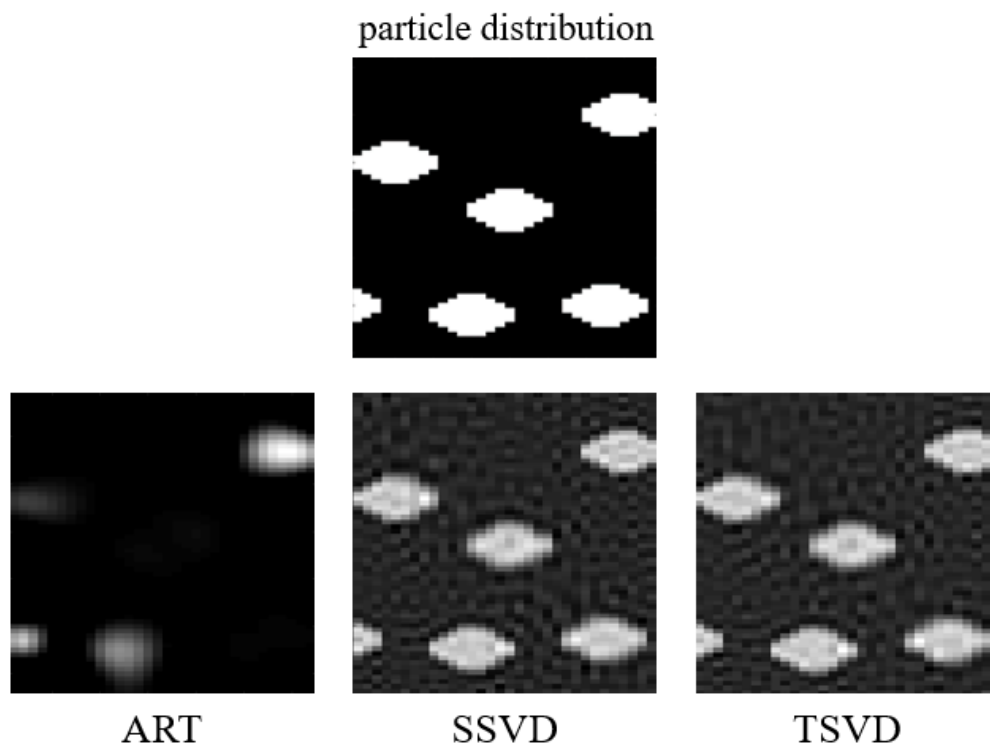


Figure 2.34: Results for Cartesian Scanning Trajectory, with $SNR = 50 \text{ dB}$ additional noise. PSNR values for ART, SSVD and TSVD are 8.07, 19.3686, 19.5740 respectively.

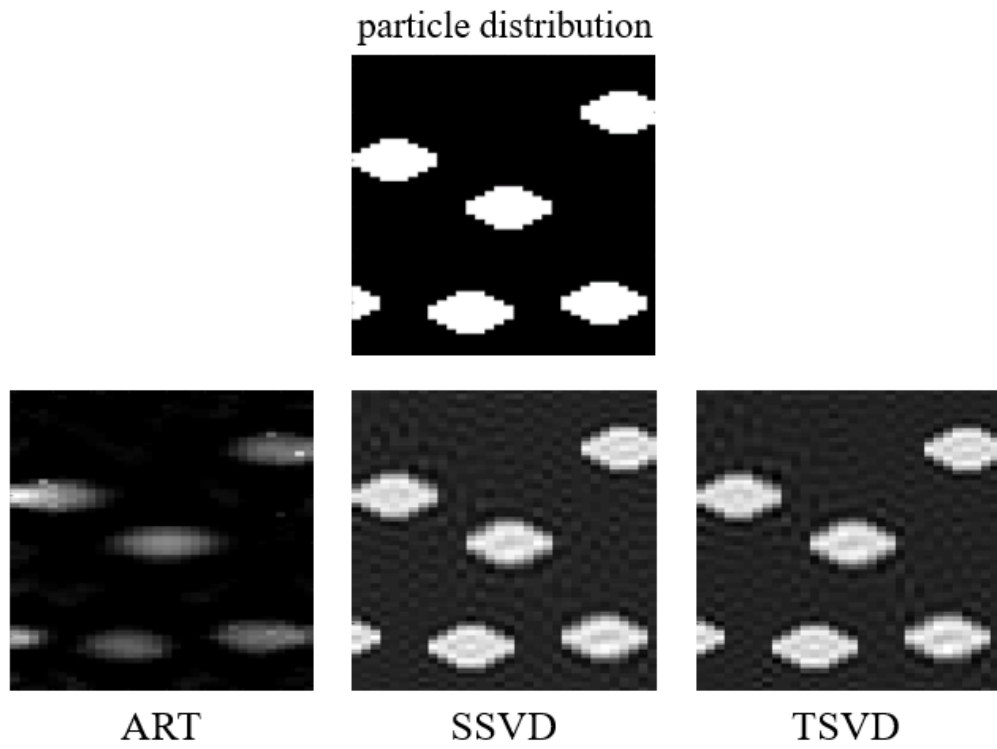


Figure 2.35: Results for Lissajous Scanning Trajectory, with $SNR = 50 \text{ dB}$ additional noise. PSNR values for ART, SSVD and TSVD are 8.07, 21.2961, 21.3319 respectively.

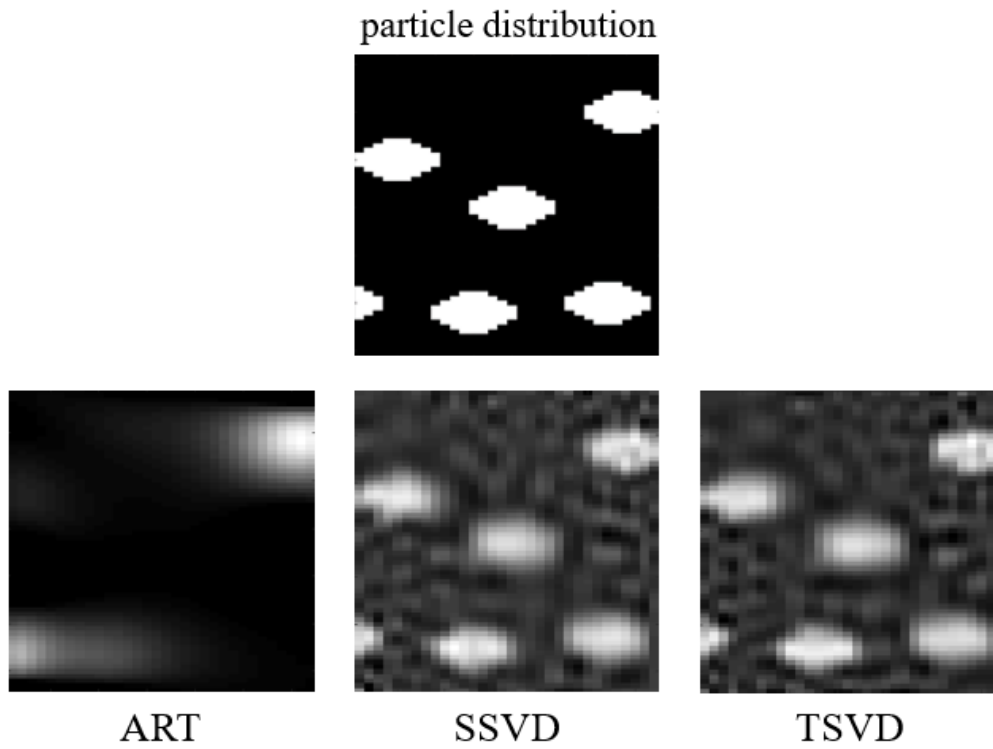


Figure 2.36: Results for Cartesian Scanning Trajectory, with $SNR = 34$ dB additional noise. PSNR values for ART, SSVD and TSVD are 7.13, 17.2133, 16.0055 respectively.

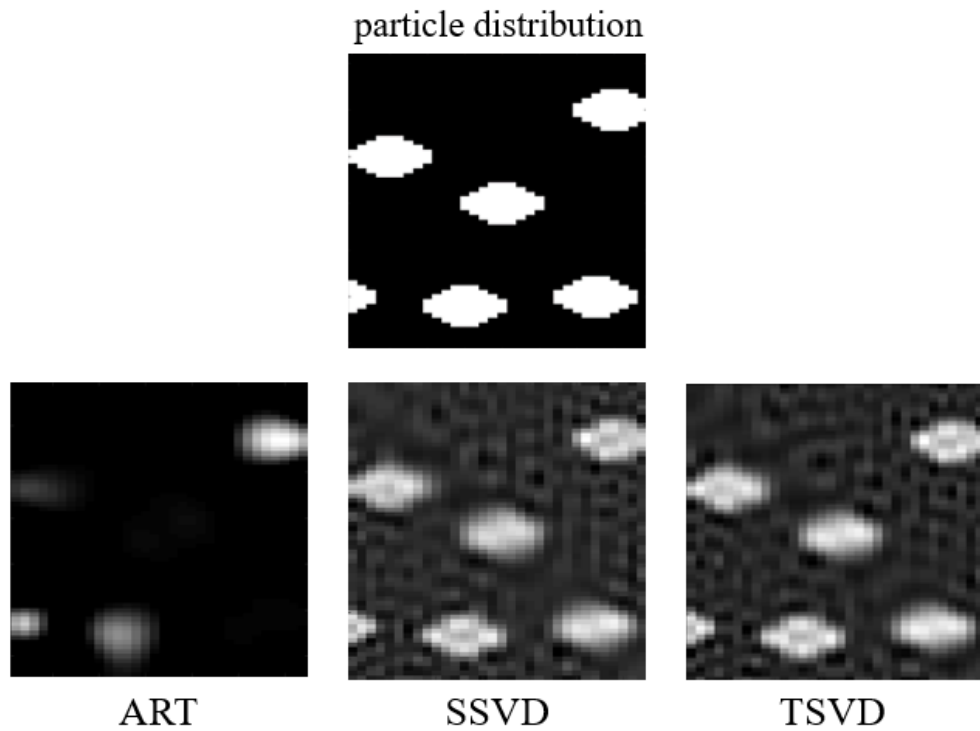


Figure 2.37: Results for Lissajous Scanning Trajectory, with $SNR = 34 \text{ dB}$ additional noise. PSNR values for ART, SSVD and TSVD are 8.07, 17.2133, 17.4243 respectively.

In this chapter, details of the modelled MPI system were given and three different reconstruction techniques were used in order to obtain images. When the results are compared, it can be seen that the highest PSNR vales were found for SSVD method, when Lissajous scanning trajectory was used. ART reconstructed images, on the other hand, have the least PSNR values and mostly effected by the noise.

CHAPTER 3

SIMULATIONS ON TEMPERATURE DISTRIBUTION FOR HARMONIC MOTION MICROWAVE DOPPLER IMAGING AND TEMPERATURE MAPPING USING MPI

3.1 Introduction

In the previous chapter, a 3D MPI system was modelled with its main components and the parameters that effect the output signal. With the aim of obtaining solutions on temperature estimation, it was decided to insert a temperature distribution in the simulation, which was computed using *Pennes' Bioheat Equations* [22][23].

A healthy, homogeneous breast tissue model was chosen as the medium characteristics of where the heat transfer process took place. Characteristic parameters for the medium were inserted into the bioheat equation [24][25].

3.2 Finite Difference Time Domain Solution for Pennes Bioheat Equations

Most commonly used and accepted theoretical analysis of the heat transfer process between the blood vessels and surrounding tissues were proposed in 1948 and referred as *Pennes' Bioheat Equations* [22].

Basic form is given in equations (3.1) and (3.2) for 1D bioheat transfer analysis.

$$\rho_t c_t \frac{\partial T(x, t)}{\partial t} = k_t \frac{\partial^2 T(x, t)}{\partial^2 x} + w_b c_b (T_a - T(x, t)) + Q_{ultrasound} + Q_{metabolic} \quad (3.1)$$

$$\frac{\partial T(x, t)}{\partial t} = \frac{k_t}{\rho_t c_t} \frac{\partial^2 T(x, t)}{\partial^2 x} + \frac{w_b c_b}{\rho_t c_t} (T_a - T(x, t)) + \frac{Q_{ultrasound} + Q_{metabolic}}{\rho_t c_t} \quad (3.2)$$

where $\rho_t c_t$ is the breast tissue density, c_t is the breast tissue specific heat, k_t is the breast tissue thermal conductivity, c_b is the blood specific heat, w_b is the blood perfusion rate, T_a is the arterial blood temperature, and lastly, Q_m is the metabolic heat and, $Q_{ultrasound}$ is the ultrasound heating.

For simplicity, let $\frac{k_t}{\rho_t c_t} = C_1$ and $\frac{w_b c_b}{\rho_t c_t} = C_2$. The Bioheat Equation for 2D imaging space on z-y plane would then become

$$\begin{aligned} \frac{\partial T(y, z, t)}{\partial t} &= C_1 \frac{\partial^2 T(y, z, t)}{\partial^2 y} + C_1 \frac{\partial^2 T(y, z, t)}{\partial^2 z} \\ &+ C_2 (T_a - T(y, z, t)) + \frac{Q_{ultrasound} + Q_{metabolic}}{\rho_t c_t} \end{aligned} \quad (3.3)$$

The Finite Difference Time Domain (FDTD) method provides approximate solutions for differential equations, especially while implementing a continuous differential function in a simulation. In this study, while using FDTD in discretization, dt , dy and dz notations were used to represent the stepsize in time, in y-axis and z-axis respectively. Partial derivatives in the equation can be written as

$$\frac{\partial T(y, z, t)}{\partial t} = \frac{T_{j,k,t+1} - T_{j,k,t}}{dt} \quad (3.4)$$

$$\frac{\partial^2 T(y, z, t)}{\partial^2 y} = \frac{T_{j+1,k,t} - 2T_{j,k,t} + T_{j-1,k,t}}{(dy)^2} \quad (3.5)$$

$$\frac{\partial^2 T(y, z, t)}{\partial^2 z} = \frac{T_{j,k+1,t} - 2T_{j,k,t} + T_{j,k-1,t}}{(dz)^2} \quad (3.6)$$

In this study, step-size that define the grids of the medium in each direction were taken equal, hence, $dz = dy$. Recall equation(3.3) and for simplicity, let $dz = dy = d$ and $\frac{Q_{ultrasound}+Q_{metabolic}}{\rho_t c_t} = Q^*$. The discretized equation will take the form

$$\begin{aligned} \frac{T_{j,k,t+1} - T_{j,k,t}}{dt} = & C_1 \frac{T_{j+1,k,t} - 2T_{j,k,t} + T_{j-1,k,t}}{(d)^2} \\ & + C_1 \frac{T_{j,k+1,t} - 2T_{j,k,t} + T_{j,k-1,t}}{(d)^2} \\ & + C_2(T_a - T_{j,k,t}) + Q^* \end{aligned} \quad (3.7)$$

The last step is to write the equation in FDTD form in order to explicitly show the time iteration

$$\begin{aligned} T_{j,k,t+1} = & \frac{dt}{d^2} C_1 (T_{j+1,k,t} + T_{j-1,k,t} + T_{j,k+1,t} + T_{j,k-1,t} - 4T_{j,k,t}) \\ & + (1 - C_2 dt) T_{j,k,t} + C_2 dt T_a + dt Q^* \end{aligned} \quad (3.8)$$

3.3 Realistic Numerical Simulations for Focused Ultrasound Heating

3.3.1 Introduction

In the simulation model, energy of a focused ultrasound beam was used as the heat source and the change in temperature distribution was examined. The problem geometry is given schematically in Fig. 3.1. The initial value for the ambient temperature was defined as 310 Kelvin. This value was also assigned as the boundary condition. Table 3.1 show numerical values that were used in the model [24].

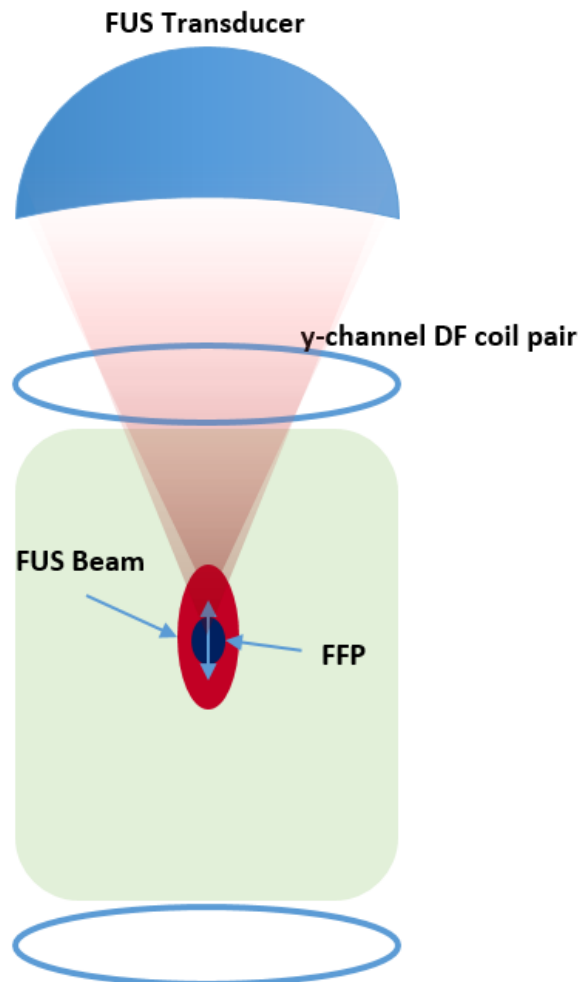


Figure 3.1: Schematical illustration for the setup that has been modelled in this study. Focused ultrasound was modelled to be applied in y-direction in the imaging plane.

Table 3.1: Numerical values used for Bioheat Equation.

healthy breast tissue density (kg/m^3)	ρ_t	1020
healthy breast tissue specific heat ($J/(kg.K)$)	c_t	3000
healthy breast tissue thermal conductivity ($W/(m.K)$)	k_t	0.42
blood specific heat ($J/(kg.K)$)	c_b	4200
blood perfusion rate ($1/s$)	w_b	0.0018
arterial blood temperature (K)	T_a	310.15
metabolic heat (W/m^3)	Q_m	450

The initial condition that defines the temperature everywhere in the imaging space was set as $T_{j,k,1} = 310 \text{ Kelvin}$ at the beginning, where $t = 0 \text{ sec}$, just before the focused ultrasound excitation. Space domain boundary conditions for the temperature, were set to be constant (Dirichlet boundary condition) as $T_{1,k,t} = 310 \text{ Kelvin}$ and $T_{j,1,t} = 310 \text{ Kelvin}$, during the excitation.

Two heat sources were considered in this model. First one is generated from the total metabolical activity and it was assumed to be uniform everywhere in the imaging space. Metabolism-generated heat was included in the model as Q_m , the metabolic heat per volume. The second source is the energy of a focused ultrasound beam with the intensity that is measured and recorded in Electrical and Electronics Faculty laboratories at Middle East Technical University during the HMMDI project [9]. The heat generated by the focused ultrasound beam power was calculated using this intensity and applied as a distributed heat source with the symbol $Q_{ultrasound}$. 3-D illustration of the setup is given in Fig. 3.2. In order to examine the heat distribution, and the temperature changes in the whole imaging area, a cross section on y-z plane was chosen, at the center of x-axis. An illustration for the boundary condition and heat distributions is given in Fig. 3.3 and 2-D cross section of the actual 3-D focused ultrasound intensity distribution is given in Fig. 3.4.

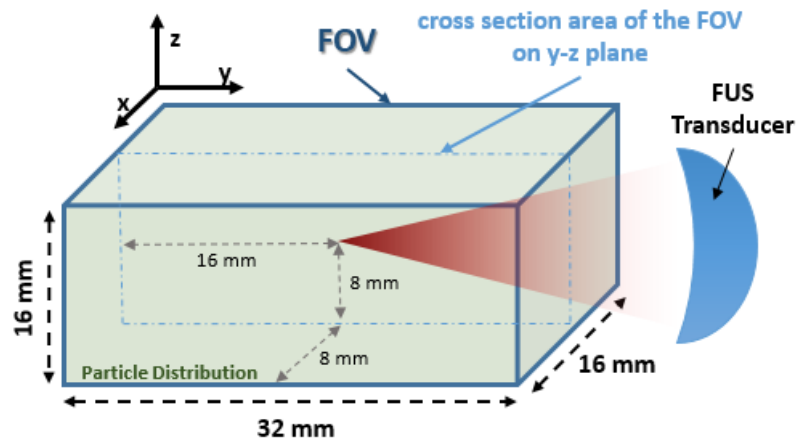


Figure 3.2: Illustration of the 3-D setup. The limits of FOV is shown with blue solid lines that forms a rectangular volume. Focused Ultrasound Transducer is modelled such that it excites along y-direction and the focus point is set to be at the center of the volume. The cross section area is shown with the dashed, blue lines.

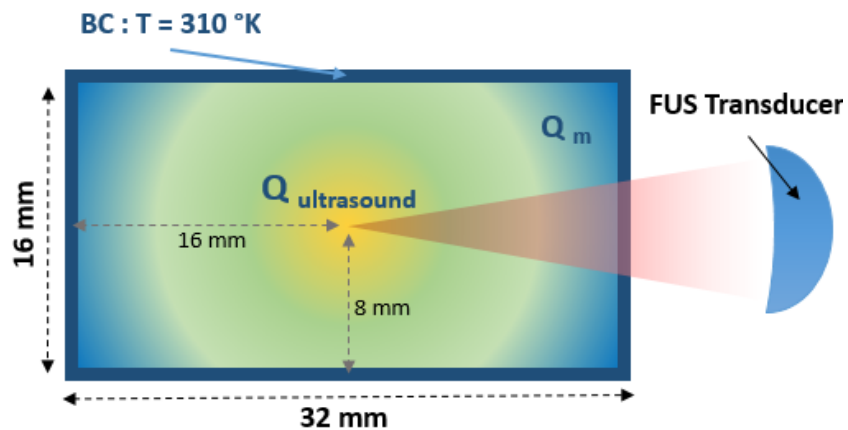


Figure 3.3: Illustration that shows the boundary condition and heat distributions. Q_m is uniform everywhere in the area.

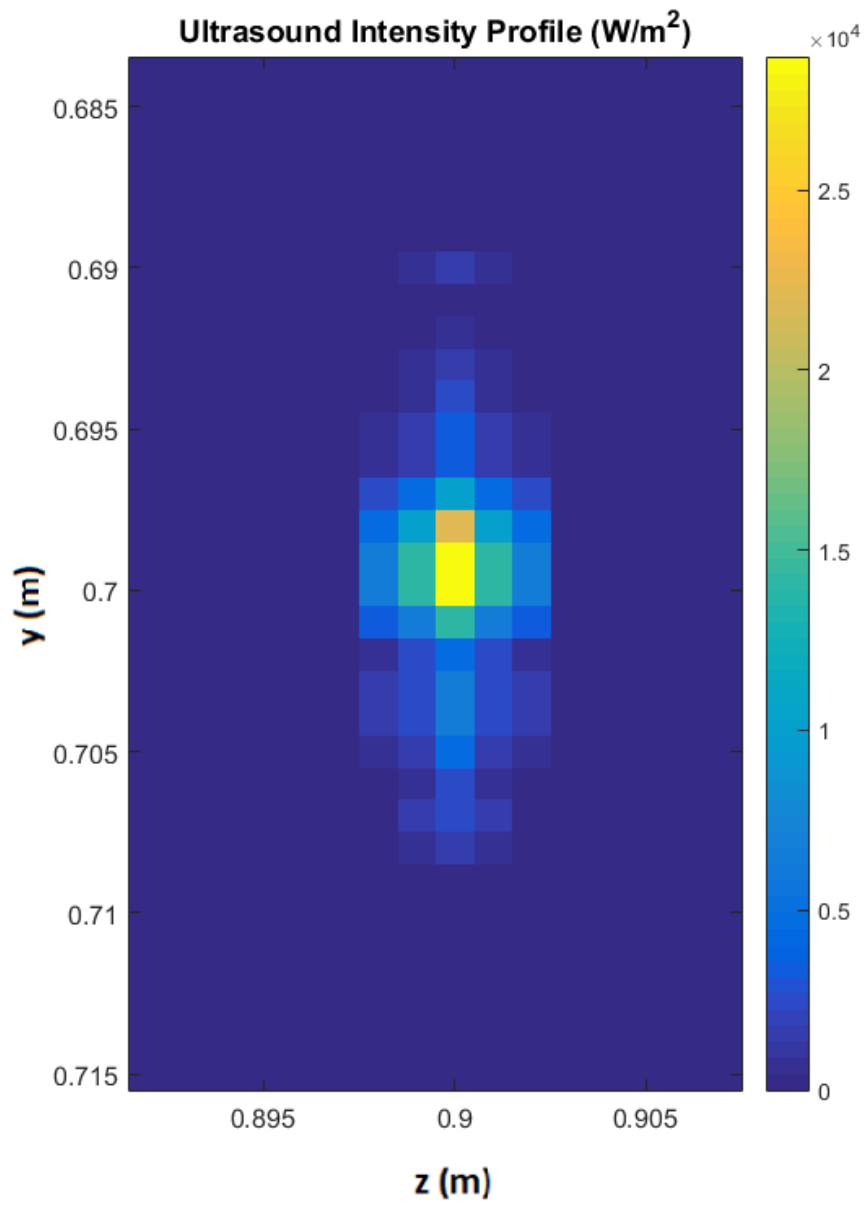


Figure 3.4: Cross section of the actual 3-D focused ultrasound intensity distribution.

3.3.2 Temperature Distribution Results of the Pennes Bioheat Model

Fig. 3.5 shows the change in temperature distribution during FUS excitation.

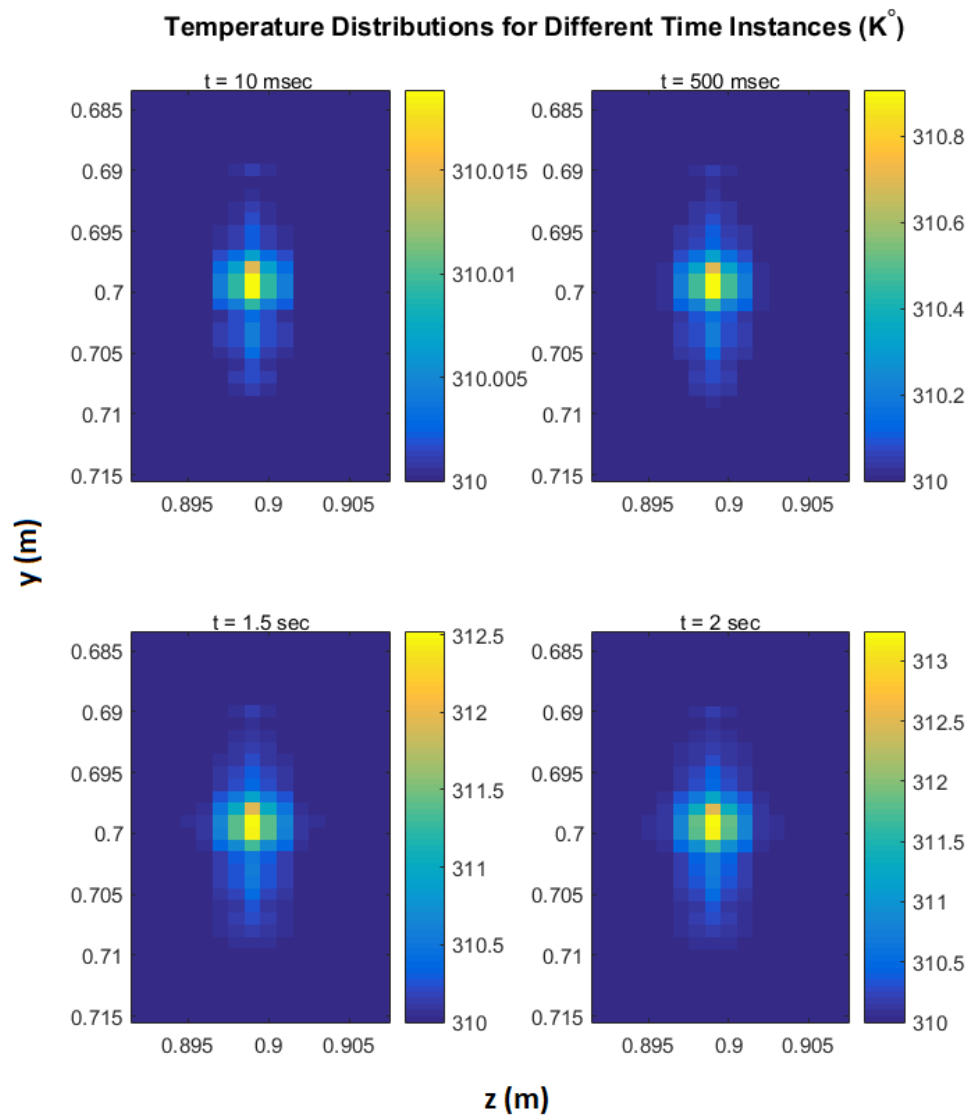


Figure 3.5: Change in temperature distribution when focused ultrasound applied in the imaging area for different durations between 10 ms and 2 seconds, along y-direction.

3.4 Temperature Estimation Method Using Magnetic Nanoparticles

3.4.1 Introduction

In this thesis study, in order to propose a method for temperature estimation using the MNPs, Weaver et al.[26] was considered as a starting point. Article proposes a method for estimating the temperature in 0-D, which is independent of the variations in magnetic core concentration and the size distribution of MNPs.

Characteristic Magnetization Signal of MNPs depends on the ambient temperature as recalled in equation (3.9).

$$M(r, t) = M_{SAT} \times V_{particle} \times \left[\coth(\beta B(r, t)) - \frac{1}{\beta B(r, t)} \right] \quad (3.9)$$

Investigating the simple mathematical expression given for the Magnetization, some variables cause complications while obtaining a model[26]. For instance, unlike the ideal case, volume-size characteristics of nanoparticles that were produced in an experimental setup and placed in a phantom, shows a large variety. Therefore, harmonics of the induced signal in the Receive coils is actually being produced as a sum of different harmonics of mixed signals, generated by nanoparticles with varying sizes. Secondly, the constant M_{SAT} which represents the saturation magnetization of MNPs, actually is dependent on the temperature itself. These two facts should be considered while obtaining realistic and accurate solutions for temperature estimation algorithms.

The signal generated by a spatial distribution of MNPs with varying volume characteristics is nothing but a sum of individual Langevin Functions that correspond to nanoparticles with different volumes.

Changing the notation for the total magnetic field as $\vec{B}(\vec{r}, t) = H_0 \cos(\omega t)$ and assuming it as the sum of Drive and Selection Fields, equation (3.9) becomes

$$\vec{M}(\vec{r}, t) = \sum_i n_i M_{SAT} V_i \left[\coth(A_L^i \cos(\omega t)) - \frac{1}{A_L^i \cos(\omega t)} \right] \quad (3.10)$$

where

$$V_i = \pi \frac{d_i^3}{6} \quad (3.11)$$

$$A_L^i = \frac{\mu_0 M_{SAT} V_i H_0}{k_B T} \quad (3.12)$$

In equation (3.10), variable n_i is the number of MNPs that have the same volume. Likewise in equations (3.11) and (3.12), i represents an arbitrary variable value for an arbitrary particle volume. Additionally, considering equation (3.12), A_L^i appears to reflect changes both in the temperature, T and the Magnetic Field Strength H_0 which is advantageous in proposing a method for temperature estimation.

3.4.2 Calibration Curves Obtained from MPI Relaxometer and 1D Scanning

It was mentioned that the variable M_{SAT} is also dependent on the temperature. The relation can be modelled by the mathematical expression in equation (3.13)

$$M_{SAT}(T) = M_0(1 - bT^a) \quad (3.13)$$

where M_0 is the Magnetization Signal that is generated at zero Kelvin temperature. In Weaver's article, constant values for a and b are as follows: $a = 1.65, b = 2.8 \times 10^{-5} K^{\frac{3}{2}}$. A_L^i appears to change proportionally with $B/(T/(1 - bT^a))$.

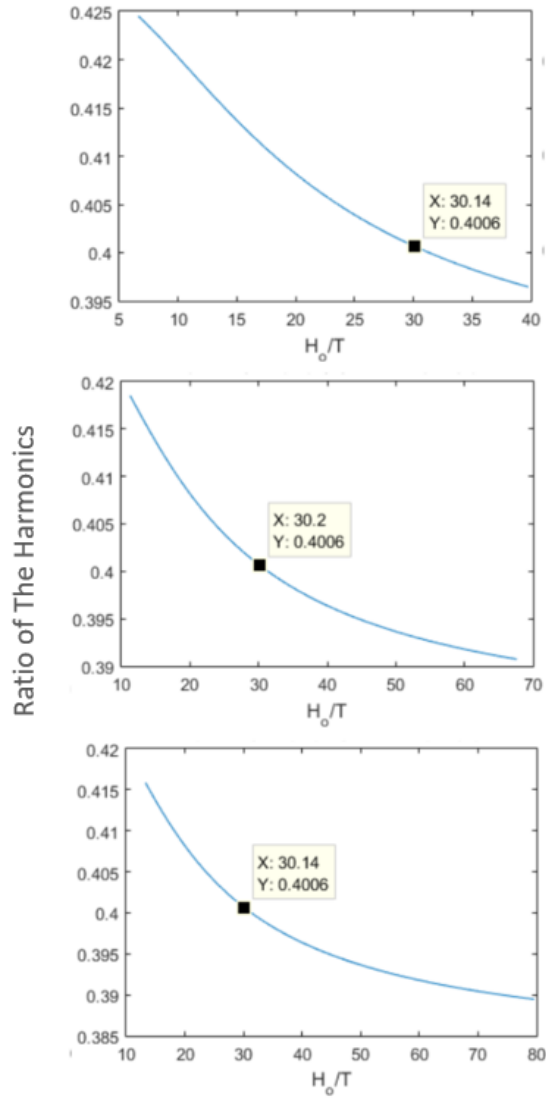


Figure 3.6: Plots showing changes in the Ratio of Harmonics with respect to H_0/T . All of the three plots were obtained from 0-D simulations with only one excitation field with frequency 1470Hz. From upper to the lower graphs, the amplitude of the applied field increases.

Fig.3.6 shows that for the same value of H_0/T , the ratio of the fifth and the third harmonics are the same. This means that, when temperature is held constant and the applied magnetic field strength is changed; without changing the particle distribution, a *Calibration Curve* can be obtained via recording the ratio of the fifth and the third harmonics. This leads to a conclusion that, if this calibration curve is obtained and the magnetization signal is decomposed to its harmonics, temperature value corresponding to the known applied field strength can be found.

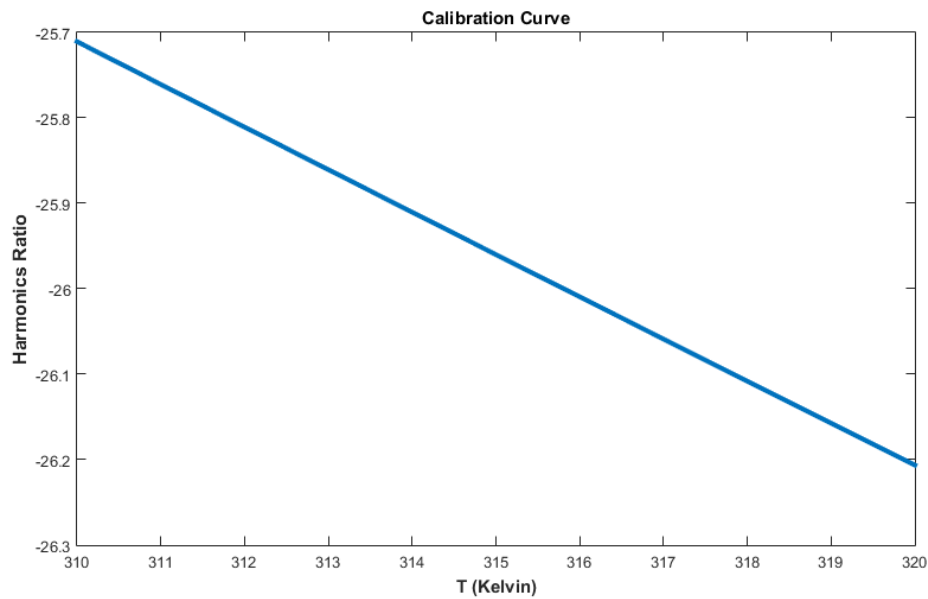


Figure 3.7: Calibration Curve obtained from MPI relaxometer by changing the temperature from 310 to 320 Kelvin, under applied magnetic field with 1mT strength and 20kHz frequency.

The calibration curve shown in Fig. 3.7 was obtained from a model of single nanoparticle that is excited with a sinusoidal drive field, in other words, without a particle distribution or a scanning process. In this study, as the next step, 1D MPI scanning results were obtained to form a calibration curve of a line scan. In order to do so, different calibration curves were obtained using different Drive Field frequencies and field strengths in order to find the most sensitive parameters for temperature changes by comparing the slopes of the obtained calibration curves. Comparison table is given in table (3.2).

Table 3.2: Slopes of calibration curves, obtained by using different parameters for the applied field strength and frequency.

	5 kHz	10 kHz	20kHz
1 mT	1,768	1,768	1,768
2 mT	1,346	1,346	1,346
3 mT	0,993	0,993	0,993
4 mT	0,748	0,748	0,748
5 mT	0,583	0,583	0,583

Examining the comparison table, one can conclude that the most sensitive parameters are when 1 mT drive field strength applied and the ratio of 5th to 3rd harmonics were used. It can be seen that the frequency changes does not effect the slopes of the calibration curves. The resultant calibration curve is given below in Fig. 3.8.

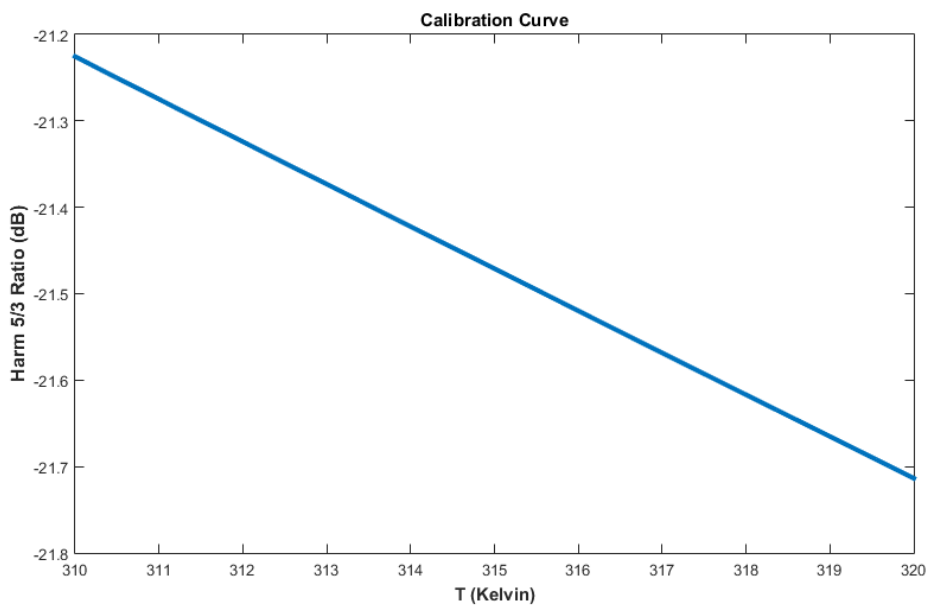


Figure 3.8: Calibration Curve obtained from 1D Line scanning by changing the temperature from 310 to 320 Kelvin, under applied magnetic field with 1mT strength and 20kHz frequency and an additional 2 T/m Selection Field .

3.4.3 Results and Conclusions

It was explained that the aim in this study is to estimate the temperature distribution in a certain region, which is specifically the focal region of the focused ultrasound probe, after ultrasound excitation. For simplicity, it was assumed that FOV is fully covered with particles in each point, in other words, magnetization signal was collected from all over the imaging area. The scanning and the estimation were done only around the ultrasound focus area, which is the region of maximum temperature rise. The Selection field was set to have 2 T/m amplitude in z-direction, and 1 mT Drive Field with 20 kHz Drive Field frequency was given additionally in the y-direction. In order to scan each pixel, the center of the FFP was shifted at each pixel center and temperature was estimated using the calibration curve at each center location. 2D temperature estimation results and estimation error are given below in figures 3.9 and 3.10.

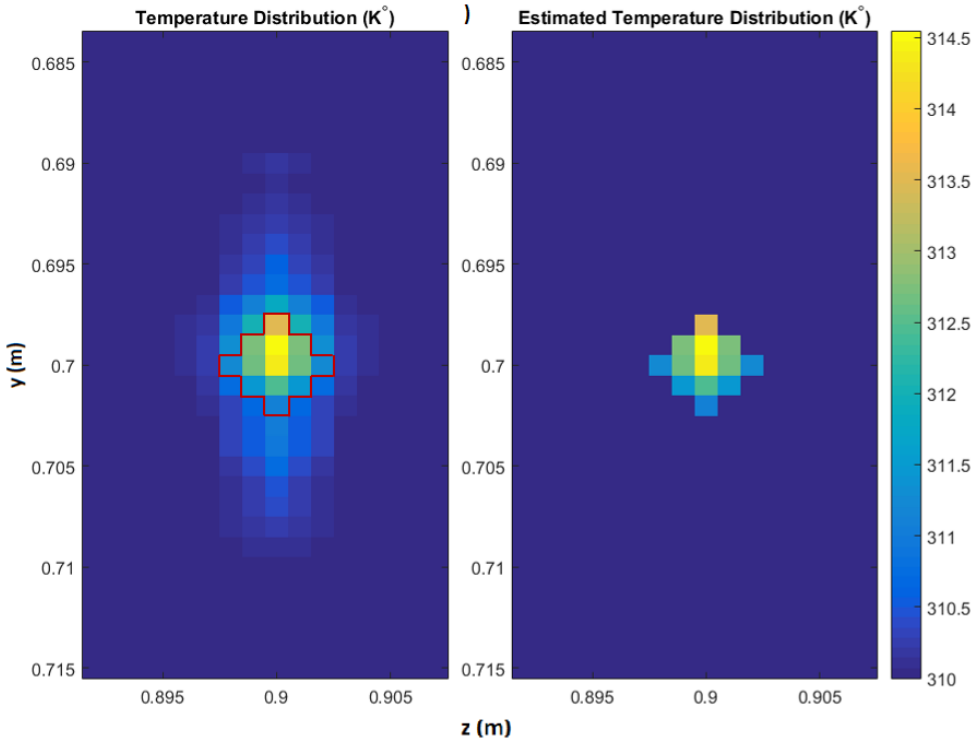


Figure 3.9: Estimated temperature distribution around the ultrasound focus area (limits were marked with red lines) and the actual temperature distribution in the imaging space, after the ultrasound was applied for 3 seconds. Maximum relative error was calculated as 0.003%, approximately.

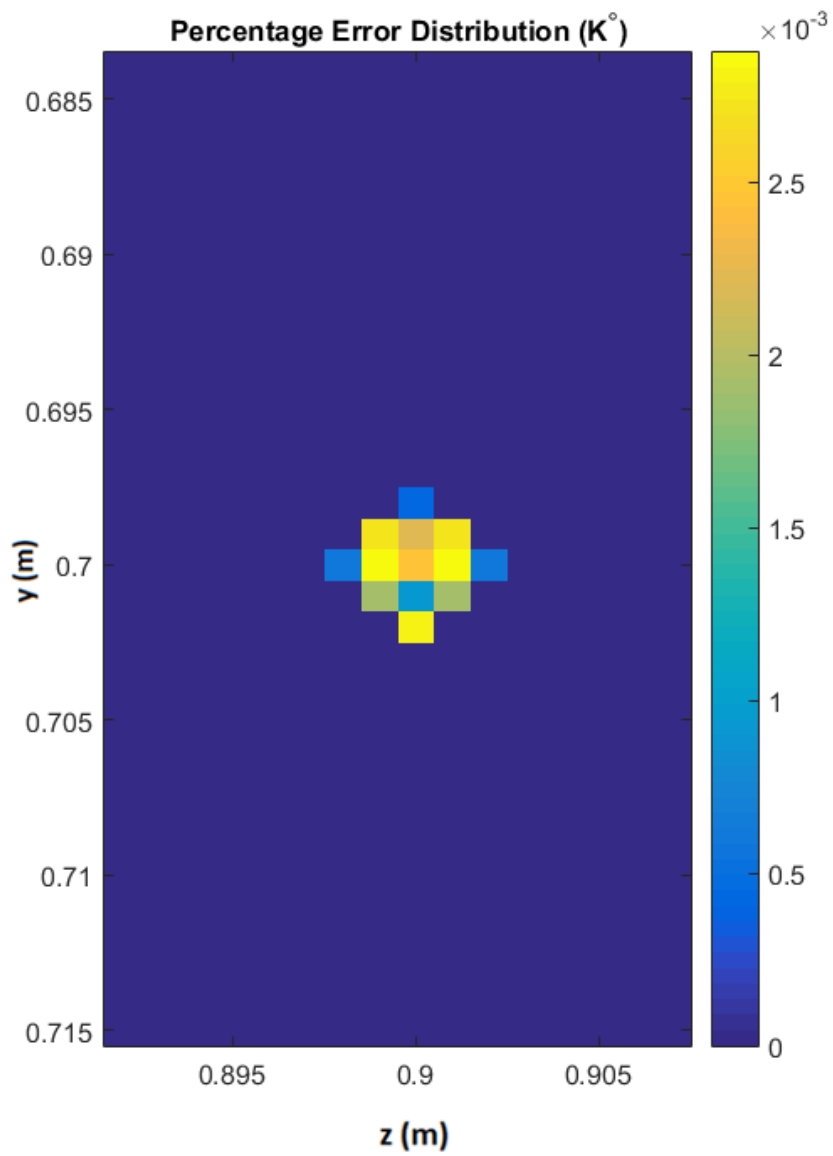


Figure 3.10: Error Distribution between the original temperature distribution and the estimated temperature distribution.

While proposing a temperature estimation method, it is important to consider any parameter in an actual setup that would affect the results, as the actual aim is to track the temperature changes that may occur in an imaging technique, the HMMDI method. Therefore, the method should also be tested after noise addition. In order to do so, calibration curves were firstly examined for different noise levels, as it is given in Fig. 3.11, and the difference between the calibration data that was found for noise free case and noise added cases, given in Fig. 3.12. In addition to this, difference in the signal spectrum was analyzed for ambient temperatures 310 and 311 K and values at the first five harmonics were examined Fig. 3.13.

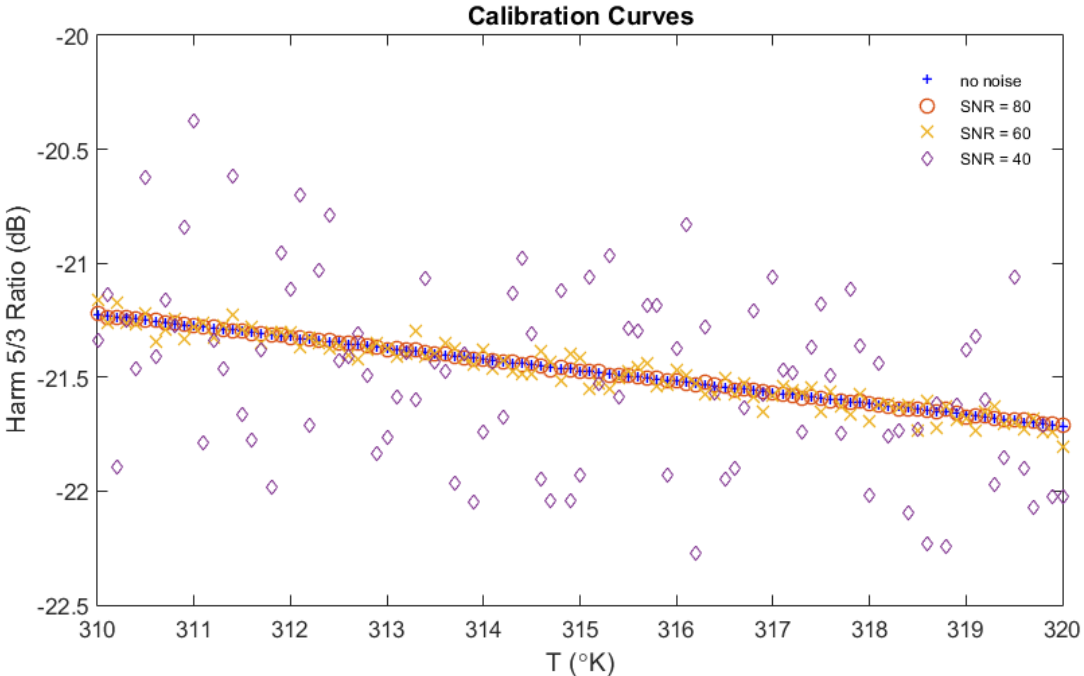


Figure 3.11: Four different calibration curve data, obtained for noise free case and noise added cases when SNR is 80, 60 and 40 dB, respectively. It can be seen that as SNR decreases, data become more dispersed and lose the linear structure. For this reason, one can conclude that the error in temperature estimation would increase as SNR decreases.

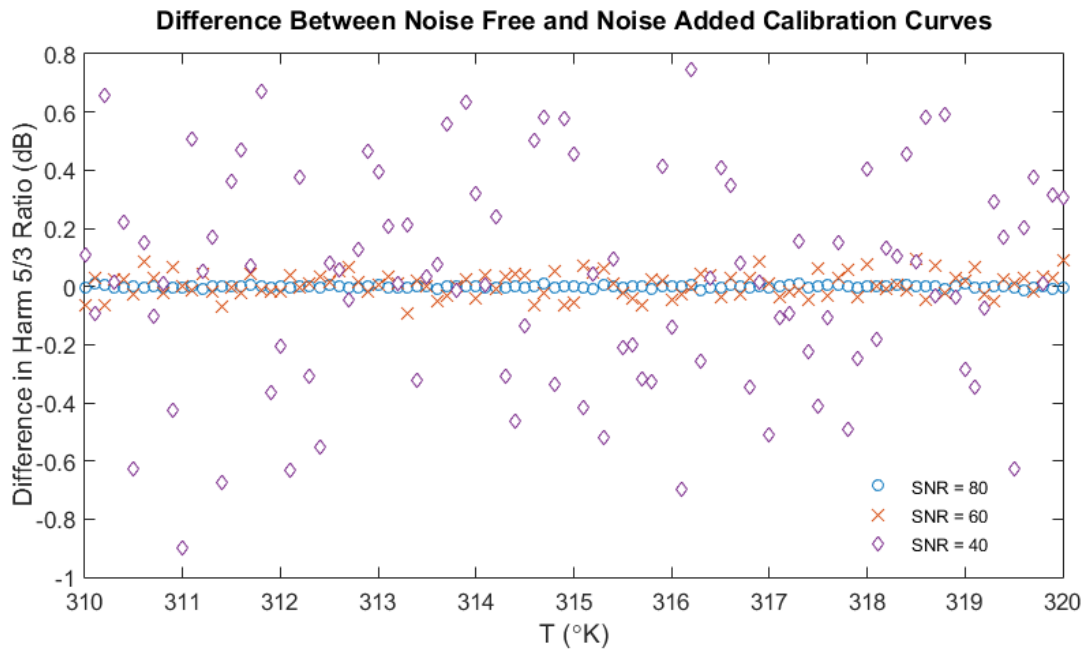


Figure 3.12: Difference between the calibration curve data, obtained for noise free case and noise added cases when SNR is 80, 60 and 40 dB, respectively.

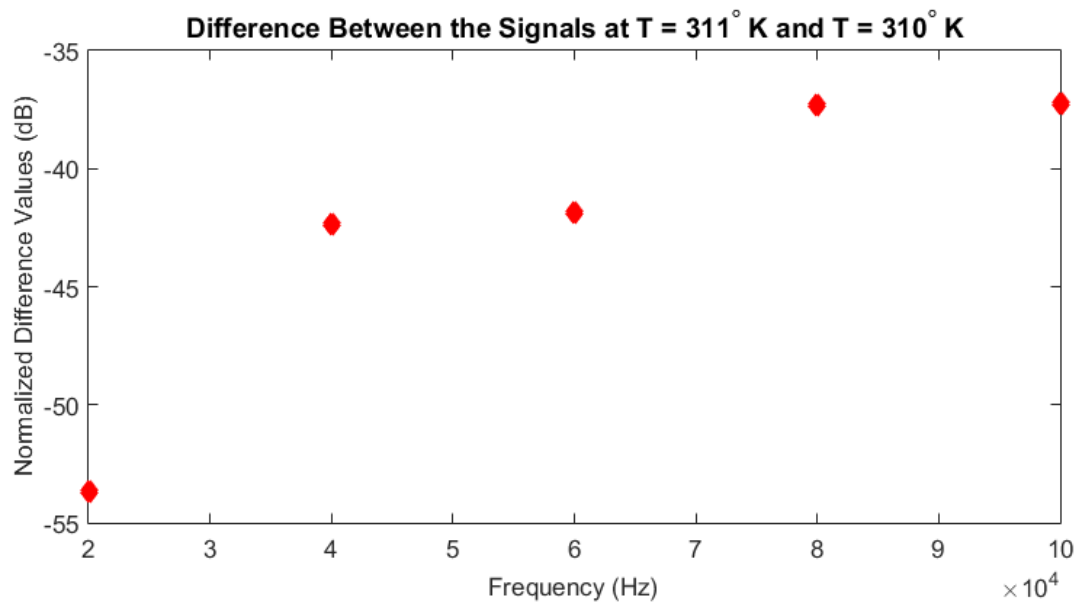


Figure 3.13: Difference data in the signal spectrum. It can be seen that the signal levels at the 3rd and 5th harmonics changes about -40 dB, for 1 K alteration in the ambient temperature.

3.5 Linearization Method for Temperature Estimation Using Magnetic Nanoparticles

3.5.1 Introduction

Linearization is a way to approximate the output of a non-linear function validly in a small region and it is commonly used to transform a nonlinear problem into a linear one that can be solved using standard methods. It was explained that an MPI system takes the advantage of the non-linear behaviour of MNPs when they are exposed to an external magnetic field. Therefore in this study, the modelled MPI system can be considered non-linear, as the relation between the input excitations and the resultant output signal is defined with the non-linear Langevin Function as given in equation (2.2). In the previous section, it was explained that there is a relation between the medium temperature and the MNP magnetization, as given in equation (3.10). In this study, a linearization method using Taylor Series Expansion, is proposed to approximate the Langevin function and obtain a linear matrix equation for describing the relation between the temperature and the magnetization signal.

3.5.2 Linearization Method

In order to linearize the magnetization signal equation, Taylor Series Expansion is used. The Taylor expansion of a function around a real point x_0 is the representation of the map as sum of a polynomial of a certain degree and an infinitesimal function of order bigger than the degree [27]. Formulation for the Taylor expansion is given as

$$f(x) = f(x-x_0) + \frac{f'(x-x_0)}{1!}x + \frac{f''(x-x_0)}{2!}x^2 + \dots = \sum_{k=0}^{\infty} \frac{f^{(k)}(x-x_0)}{k!}x^k \quad (3.14)$$

For the proposed method, only the first and the second terms were used. As the aim is to find the temperature distribution, and as the magnetization signal is modelled with the temperature-dependent Langevin function; Taylor expansion above can be written using variable T , assuming that the function is linearized around the initial temperature T_0 . The resultant formulation can be written as

$$f(T) = f(T_0) + f'(T_0) (T - T_0) \quad (3.15)$$

Here, T represents the actual temperature value for a single point that will be estimated and T_0 is the initial temperature, which was set to be $310^\circ K$ and the function f represents the received signal at a time instance in the imaging space, therefore it can also be represented as u , like it was defined in equations (2.36) and (2.38). One can conclude that the temperature value T , can be estimated if the magnetization signal for T , T_0 and the partial derivative of the magnetization signal at T_0 are known.

In the previous chapter, it was explained that, the relation between the excitations and the output signal in MPI system can be described with a system matrix (2.42) and particle distribution can be found with a matrix equation (2.40). Using the fact that the system matrix entries are dependent on the Langevin function as previously given in equation (3.10), elements of the system matrix can be written as

$$s_{t,i,\tau} = K \frac{\partial L_{t,i,\tau}}{\partial t} = K \dot{L}_{t,i,\tau} \quad (3.16)$$

where K is a constant for representing the parameters that are related to MNP and medium characteristics, $s_{t,i,\tau}$ is the discretized form of system function and $L_{t,i,\tau}$ is the discretized form of the magnetization function. Like it was denoted in equation (2.38), t represents the index for the time instance and i represents the pixel number in FOV. Differently in this equation, τ represents the temperature value at pixel i , and $\frac{\partial L}{\partial t}$ is represented with $\dot{L}_{t,i,\tau}$.

Using equation (3.16) in (3.15), knowing that the f function is actually the system matrix entry, one can obtain

$$K \dot{L}_{t,i,T} = K \dot{L}_{t,i,T_0} + K \left. \frac{\partial \dot{L}_{t,i,\tau}}{\partial \tau} \right|_{\tau=T_0} (T - T_0) = K \dot{L}_{t,i,T_0} + K \dot{L}'_{t,i,T_0} (T - T_0) \quad (3.17)$$

where

$$\dot{L}'_{t,i,T_0} = \left. \frac{\partial \dot{L}_{t,i,\tau}}{\partial \tau} \right|_{\tau=T_0} \quad (3.18)$$

Using the consequent equations above, in an actual MPI system, it is possible to estimate the temperature distribution in the imaging space, using matrix equations.

Recalling equation (2.38), the discrete equation for defining the relation between the magnetization signal and the particle distribution can be rewritten as

$$u_t = \sum_{i=1}^{2048} s_{t,i,T_i} c_i \quad (3.19)$$

where u_t is the induced magnetization signal for certain temperature distribution and the notation T_i denotes the temperature value at pixel i .

Additionally, system matrix can be represented as

$$S = K \begin{bmatrix} \dot{L}_{1,1,T_1} & \dot{L}_{1,2,T_2} & \dots & \dot{L}_{1,2048,T_{2048}} \\ \dot{L}_{2,1,T_1} & \dots & \dots & \dot{L}_{2,2048,T_{2048}} \\ \dot{L}_{3,1,T_1} & \dots & \dots & \dot{L}_{3,2048,T_{2048}} \\ \vdots & \vdots & \vdots & \vdots \\ \dot{L}_{77601,1,T_1} & \dots & \dots & \dot{L}_{77601,2048,T_{2048}} \end{bmatrix} \quad (3.20)$$

and the system matrix equation in equation (2.40) would become

$$K \begin{bmatrix} \dot{L}_{1,1,T_1} & \dot{L}_{1,2,T_2} & \cdots & \dot{L}_{1,2048,T_{2048}} \\ \dot{L}_{2,1,T_1} & \cdots & \cdots & \dot{L}_{2,2048,T_{2048}} \\ \dot{L}_{3,1,T_1} & \cdots & \cdots & \dot{L}_{3,2048,T_{2048}} \\ \vdots & \vdots & \vdots & \vdots \\ \dot{L}_{77601,1,T_1} & \cdots & \cdots & \dot{L}_{77601,2048,T_{2048}} \end{bmatrix} \times \begin{bmatrix} c_1 \\ c_2 \\ \vdots \\ c_{2048} \end{bmatrix} = \begin{bmatrix} u_1 \\ u_2 \\ \vdots \\ u_{77601} \end{bmatrix} \quad (3.21)$$

Taking the magnetization signal as the function f in equation (3.15), one can obtain

$$\underline{u}_T - \underline{u}_{T_0} = \underline{\dot{u}}_{T_0} \underline{\Delta T} \quad (3.22)$$

where $\underline{\Delta T} = \underline{T} - T_0$ is actually the distribution of the change in temperature that is desired to be estimated and is a 1×2048 column matrix that represents the temperature value for each pixel. Here, \underline{u}_T is the magnetization signal vector that is obtained with the temperature distribution, \underline{T} , and \underline{u}_{T_0} is the magnetization signal vector that is obtained when each pixel is $310^\circ K$. These two signals are a priori data that can be collected before estimating the temperature distribution. Recalling the equation (3.18), $\underline{\dot{u}}_{T_0}$ can be shown as

$$\underline{\dot{u}}_{T_0} = K \begin{bmatrix} \dot{L}'_{1,1,T_0} & \dot{L}'_{1,2,T_0} & \cdots & \dot{L}'_{1,2048,T_0} \\ \dot{L}'_{2,1,T_0} & \cdots & \cdots & \dot{L}'_{2,2048,T_0} \\ \vdots & \vdots & \vdots & \vdots \\ \dot{L}'_{77601,1,T_0} & \cdots & \cdots & \dot{L}'_{77601,2048,T_0} \end{bmatrix} \times \begin{bmatrix} c_1 & \cdots & 0 \\ 0 & \ddots & 0 \\ 0 & \cdots & c_{2048} \end{bmatrix} \quad (3.23)$$

Equation (3.23) can be written in the form

$$\underline{\dot{u}}_{T_0} = K \underline{\dot{S}} \underline{c} \quad (3.24)$$

where

$$\underline{\dot{S}} = \begin{bmatrix} \dot{L}'_{1,1,T_0} & \dot{L}'_{1,2,T_0} & \cdots & \dot{L}'_{1,2048,T_0} \\ \dot{L}'_{2,1,T_0} & \cdots & \cdots & \dot{L}'_{2,2048,T_0} \\ \dot{L}'_{3,1,T_0} & \cdots & \cdots & \dot{L}'_{3,2048,T_0} \\ \vdots & \vdots & \vdots & \vdots \\ \dot{L}'_{77601,1,T_0} & \cdots & \cdots & \dot{L}'_{77601,2048,T_0} \end{bmatrix} \quad (3.25)$$

and, in order to use the correct notation in the matrix equation, the particle distribution data was converted to a 2048×2048 diagonal matrix \underline{c} which has the form

$$\underline{c} = \begin{bmatrix} c_1 & \cdots & 0 \\ 0 & \ddots & 0 \\ 0 & \cdots & c_{2048} \end{bmatrix} \quad (3.26)$$

For simplicity, let $\underline{u}_T - \underline{u}_{T_0} = \underline{u}_D$ and one can obtain

$$\underline{u}_D = K \underline{\dot{S}} \underline{c} \underline{\Delta T} \quad (3.27)$$

Similarly as it was explained, $\underline{\dot{S}}$ matrix can also be decomposed using SVD analysis in order to solve the equation (3.27) via left-multiplication of the inverse of the $\underline{\dot{S}}$ on each side. Additionally, the particle concentration \underline{c} can be estimated via methods that was discussed in the previous chapter and used as a-priori data while estimating the temperature distribution $\underline{\Delta T}$. The generalized solution to the matrix equation can be written as

$$\underline{c} \underline{\Delta T} = \frac{\underline{\dot{S}}^{-1} \underline{u}_D}{K} \quad (3.28)$$

Let $\underline{T}_c = \underline{c} \underline{\Delta T}$. As the particle distribution is known, $\underline{\Delta T}$ distribution can be found as

$$\underline{\Delta T} = \underline{c}^{-1} \underline{T}_c \quad (3.29)$$

3.5.3 Results and Conclusions

In figures 3.14, 3.15, 3.16, 3.17 the result of the temperature estimation is given together with the original temperature distribution. Additionally in figures 3.18, 3.19, 3.20, 3.21 error distribution between the original and estimated temperature is given. Maximum relative error for this method is calculated approximately as 0.0630%.

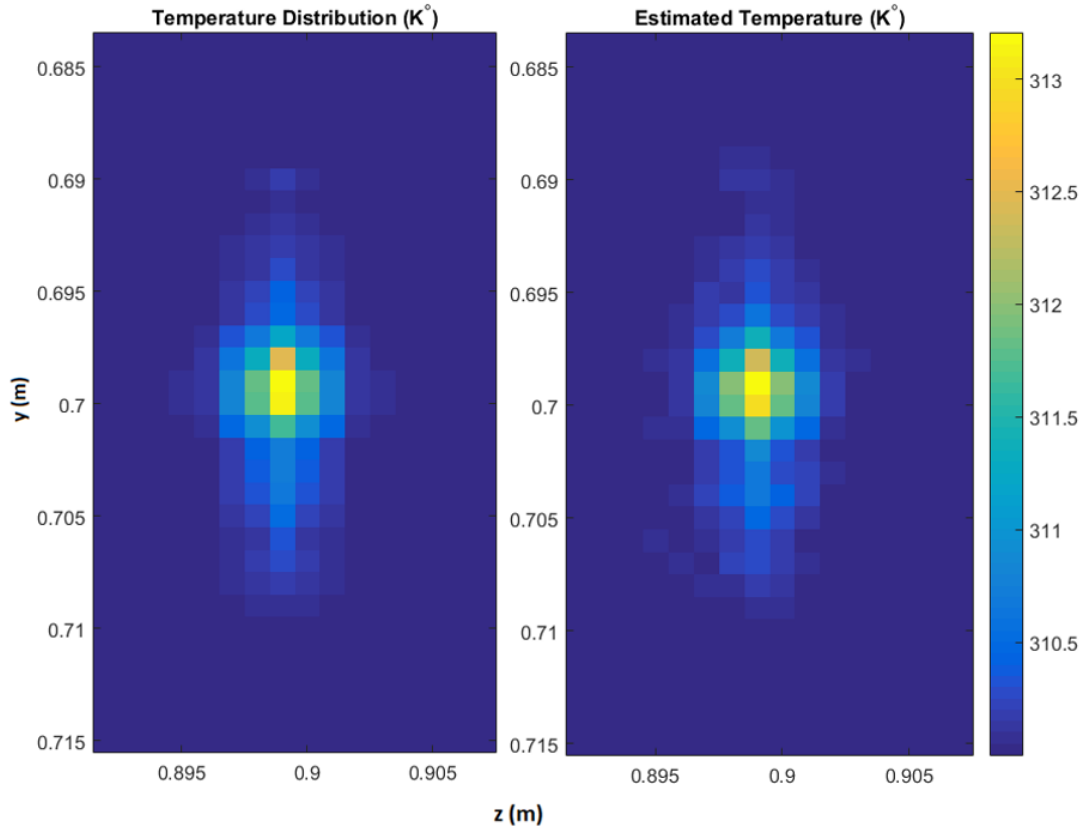


Figure 3.14: Estimated temperature distribution and the actual temperature distribution in the imaging space for the noise free case, after the ultrasound was applied for 2 seconds. For simplicity, it was assumed that the FOV is fully covered with uniform particle distribution. Maximum relative error is calculated approximately as 0.063%

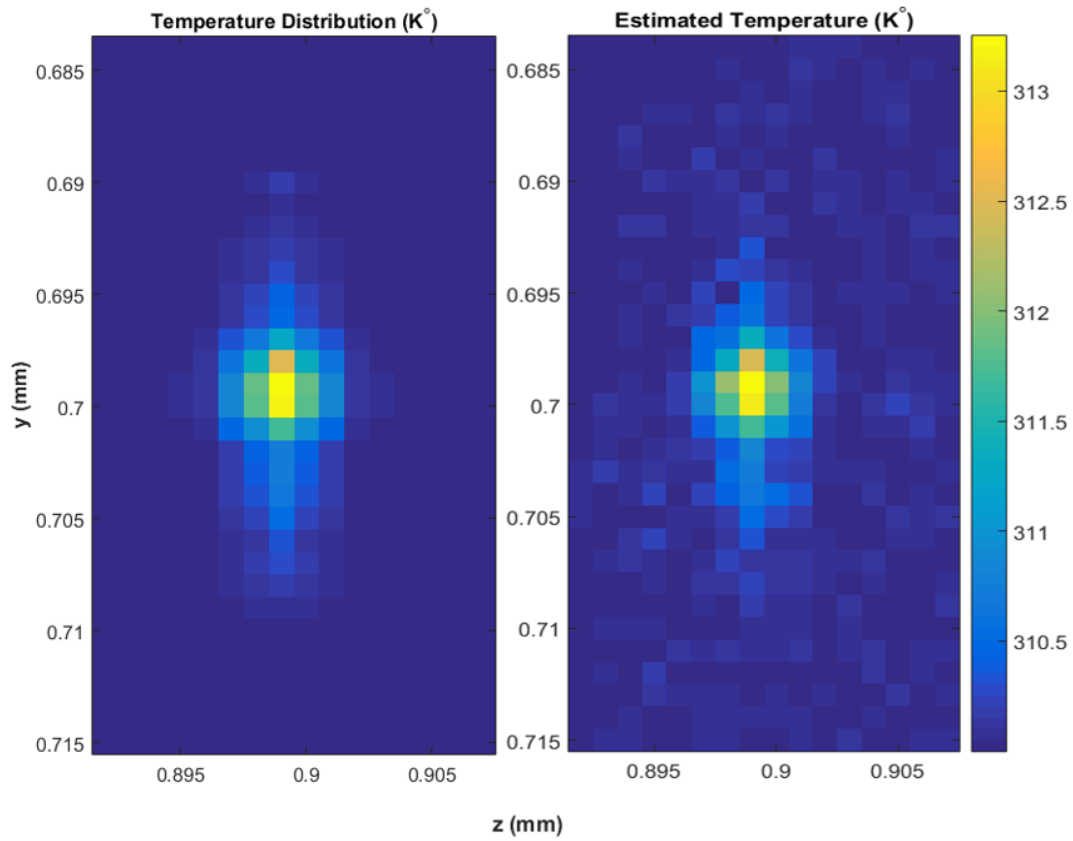


Figure 3.15: Temperature estimation results for noise added case. SNR is set to be 80 dB and FUS was applied for 2 seconds. Maximum relative error is calculated approximately as 0.0706%

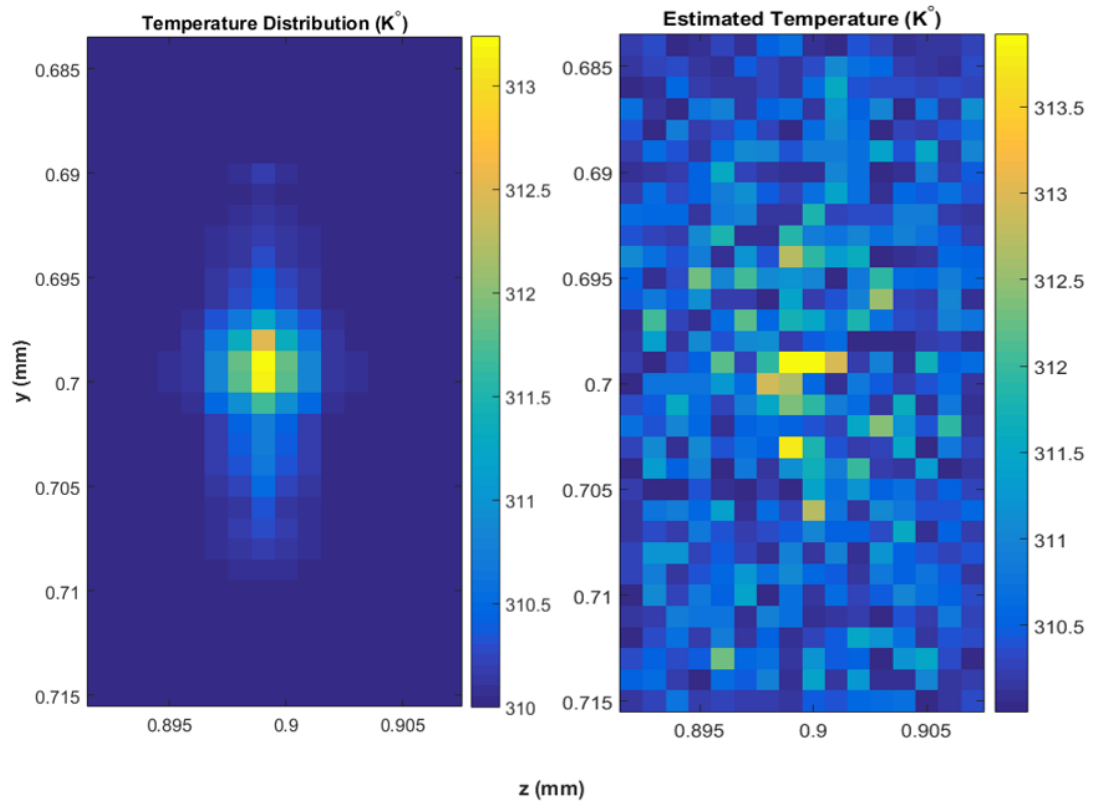


Figure 3.16: Temperature estimation results for noise added case. SNR is set to be 60 dB and FUS was applied for 2 seconds. Maximum relative error is calculated approximately as 0.9805%

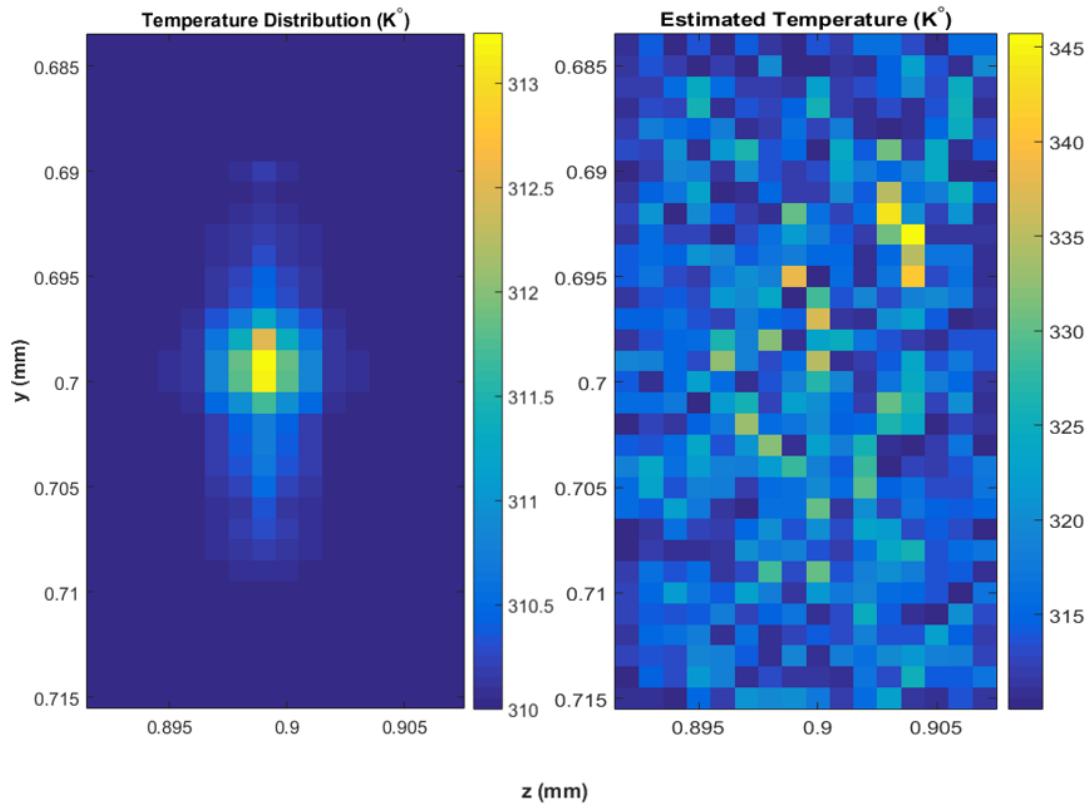


Figure 3.17: Temperature estimation results for noise added case. SNR is set to be 40 dB and FUS was applied for 2 seconds. Maximum relative error is calculated approximately as 11.5240%

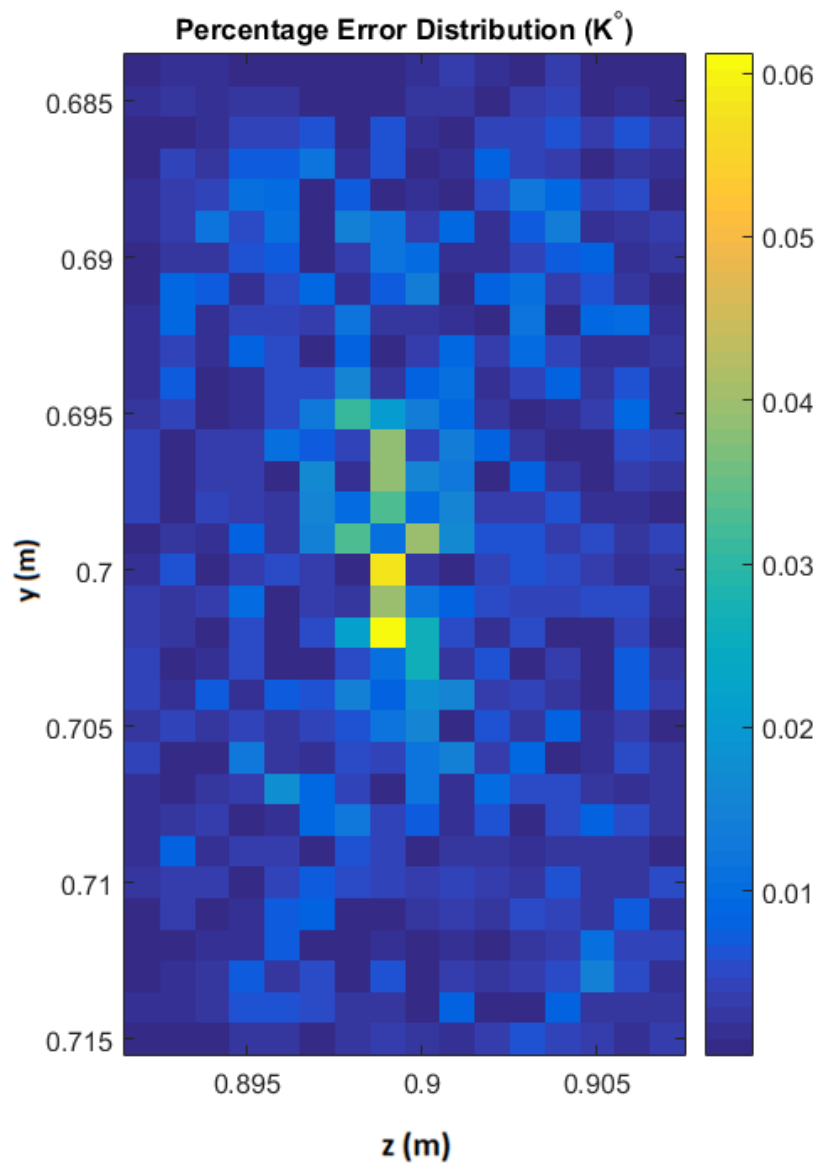


Figure 3.18: Error Distribution between the original temperature distribution and the estimated temperature distribution for the noise free case.

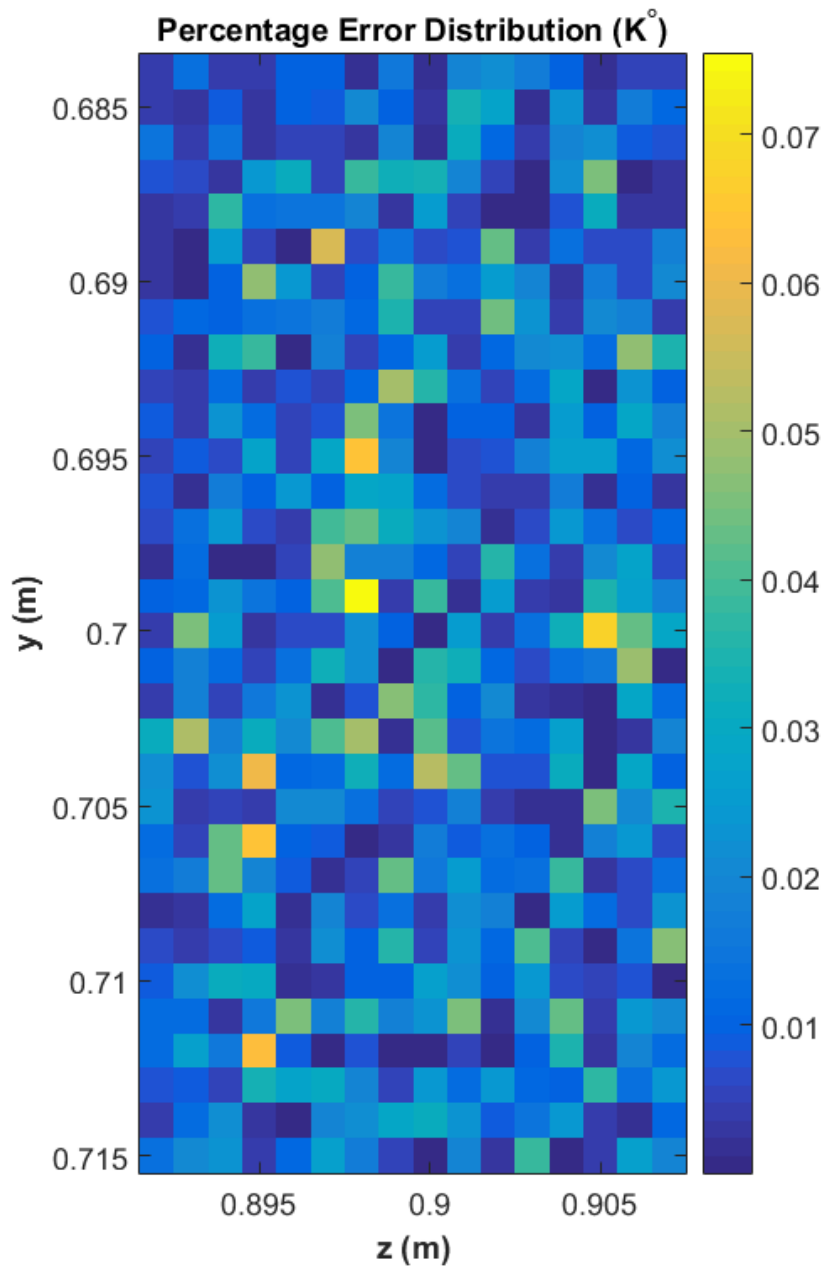


Figure 3.19: Error Distribution between the original temperature distribution and the estimated temperature distribution when SNR is 80 dB.

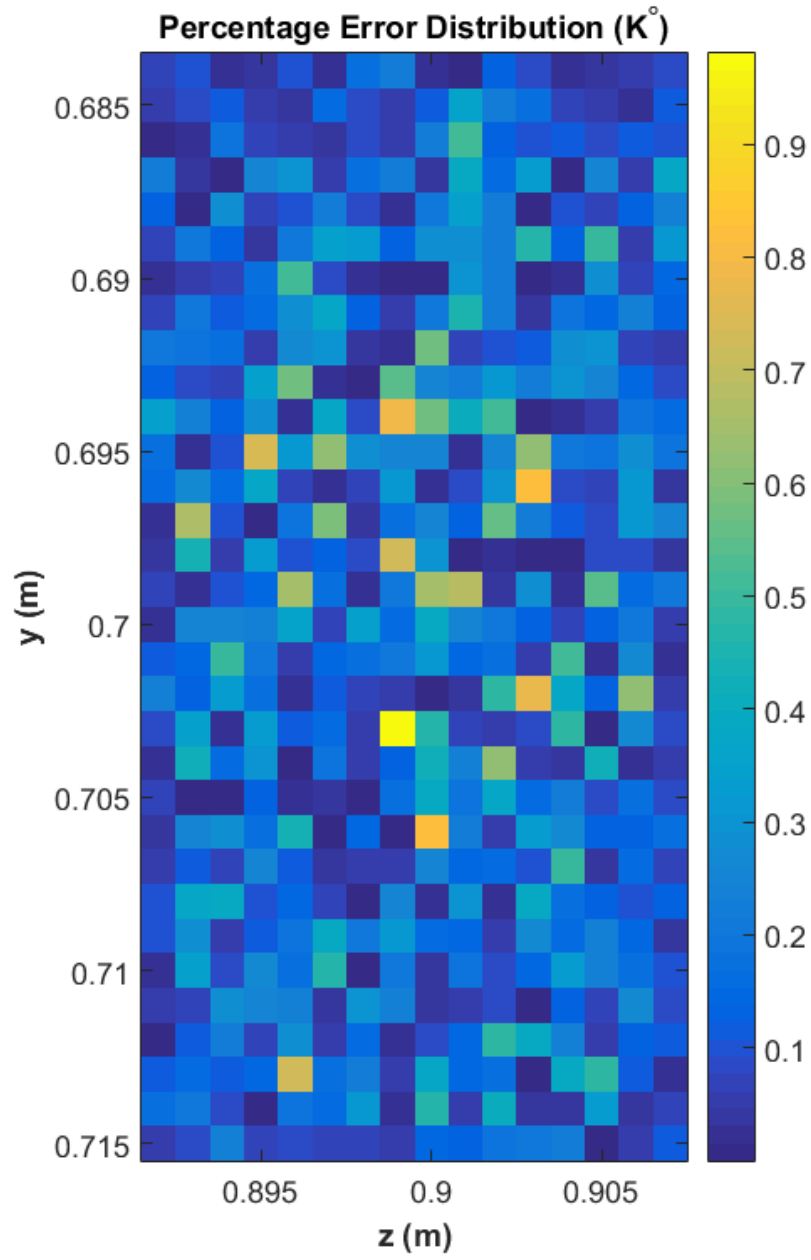


Figure 3.20: Error Distribution between the original temperature distribution and the estimated temperature distribution when SNR is 60 dB.

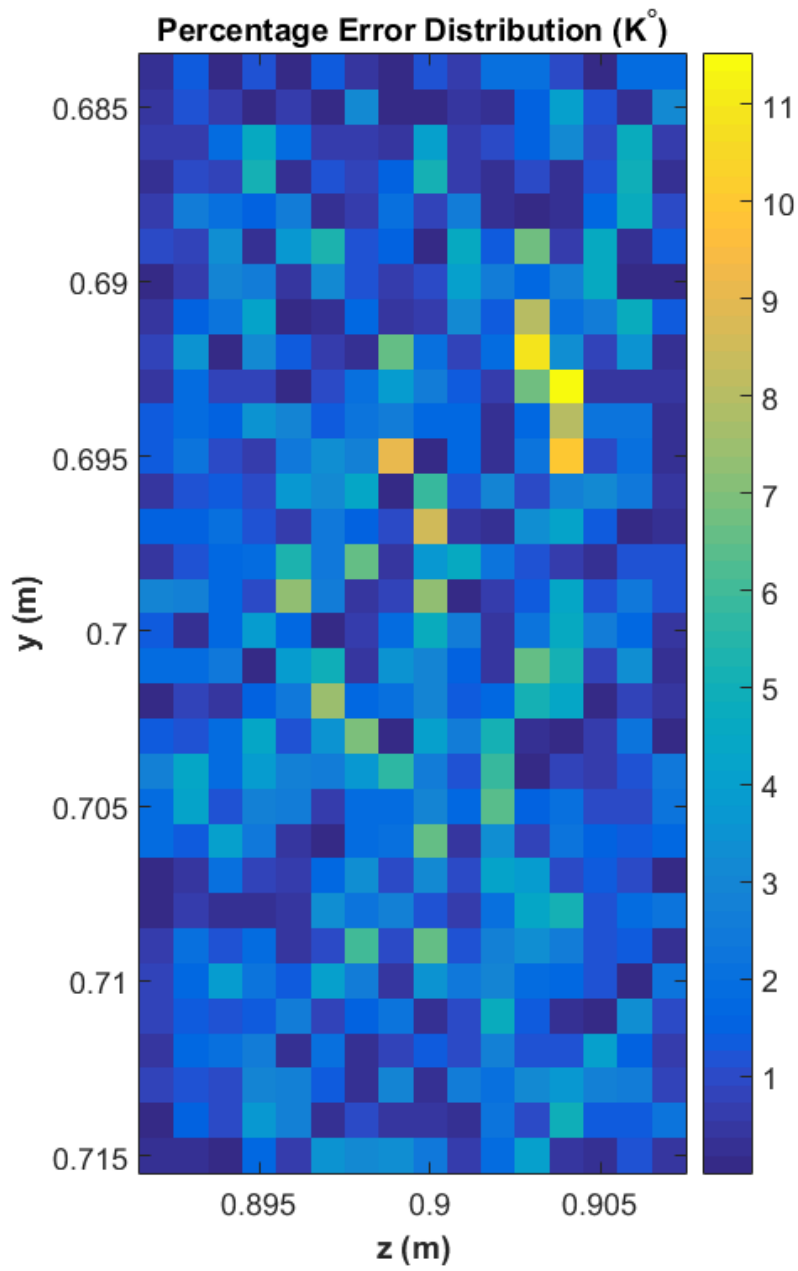


Figure 3.21: Error Distribution between the original temperature distribution and the estimated temperature distribution when SNR is 40 dB.

CHAPTER 4

CONCLUSION AND FUTURE WORK

The purpose of this thesis study was to develop a temperature estimation method that provides good thermal resolution and accurate mapping for monitoring temperature changes that may occur either during a medical imaging or thermal therapy. The method uses magnetic nanoparticles (MNPs) that can be introduced intravenously inside the body and take the advantage of temperature-dependent magnetic behavior they show when they are exposed to an external magnetic field. As the outcome of this study, two different methods were proposed and tested for noise free cases.

The MNPs inside the body can be directly imaged with the Magnetic Particle Imaging (MPI) modality. This method uses the field free region (FFR) concept that can be generated between two magnets with opposite polarity. The MNPs inside the FFR is responsive to an additional time varying field. The FFR generating field is called Selection Field, while the time-varying field(s) are called the Drive Field(s). MNPs outside the FFR region generate no response as they are magnetically saturated. The FFR is scanned throughout the field of view to generate magnetic particle distribution. The magnetization response of the MNPs depend on the micro-environmental temperature. It was previously shown that the temperature can be estimated by first generating a calibration curve for the MNP response at known temperature values. Then, this curve can be used to obtain the actual temperature during an experiment. Previous studies on temperature estimation with MNPs are mostly limited to spectrometric measurements for an MNP sample. Concurrent magnetic particle and temperature imaging is still an open problem in the field of MPI.

In this thesis, we aimed at imaging both the MNP distribution and their temperature distribution inside a volume of interest. We specifically focused on the application

of the developed methods for Harmonic Motion Microwave Doppler Imaging (HMMDI). HMMDI, images the coupled microwave and elastic properties of tissues. An amplitude modulated focused ultrasound (FUS) beam is applied to the region of interest, creating local vibrations. Concurrently, a narrowband microwave signal is sent and received. Received signal spectrum includes a Doppler component due to local vibrations. This component depends both on the electrical and the elastic properties of the vibrating region. The simulations and experiments showed promising results for breast tumor detection with HMMDI [9]. The previous studies on this method didn't investigate the local temperature rise at the FUS focus. Therefore, we investigated the application of MPI temperature imaging for the HMMDI problem using simulations in thesis study.

This thesis study can be divided into three phases. In the first phase, we developed a MATLAB simulation tool for MPI, where characteristics of the applied fields, coil geometries and sensitivities, shape and volume of MNPs and characteristics of data acquisition sequences were considered as the main parameters. Using this simulator, system matrices were obtained for image reconstruction and were analyzed in terms of their condition numbers, energy distributions, singular values and spatial frequencies. Then, for a certain MNP distribution in the imaging space, different techniques were used for image reconstruction and resultant images had resolution ranged in sub-millimeter level. In the second phase, we developed a thermal Finite Difference Time Domain solver, which uses Pennes Bioheat Equations. We analyzed the resultant temperature distribution for the experimentally measured FUS beam distribution as a function of applied power and time. In the third phase, we proposed two novel temperature imaging methods using MPI. In the first method, a 1-D calibration curve is obtained from linear MPI scan in a single pixel. The FFR is scanned pixel by pixel, and temperature of each pixel is determined using the measured data and the calibration curve. In the second method, the temperature and MNP density dependent MPI signal equation is linearized around normal body temperature (310 K) using Taylor Series Expansion. A two-step procedure was used to estimate the temperature distribution. First, MPI data is gathered without FUS application, which assumes 310 K uniform temperature distribution. Using this data, MNP distribution inside the FOV is obtained. Then, FUS is applied, and another MPI data is acquired from the same

FOV. Using the MNP distribution and linearized model, temperature distribution is obtained. The following sections summarize the work done, results, and conclusions for each phase of this study.

4.1 Magnetic Particle Imaging Simulations

In the developed MPI simulation model, selection field, drive field and receive coil geometries, MNP properties (temperature, magnetic saturation field, volume) and spatial distribution can be defined. The currents applied to the coils can be input as a time series. Coil generated magnetic field strengths were computed using Biot-Savart Law, and the maximum relative error calculated between the analytical and the discrete solutions was approximately 0.6%. The time domain received MPI signal is the output of the simulator.

In the scope of the thesis we modelled drive field coil pair, selection field coil pair and two receive coils as circular conductors. Selection and Drive field coils had 25 cm radius, whereas the Receive coils had 10 cm radius. Drive field coil pairs and the receive coils were placed in the y and z directions. Selection field coil pair was placed in the z-direction. Receive coil centers were 15 cm away from the imaging center. Drive and Selection field coil pairs were placed 1 meter apart from each other. Current amplitudes of the Drive field coil pairs were set to generate a Magnetic Field strength of 20 mT both in z and y direction. The Selection field coil generated a gradient strength of 2.5 T/m in the z-direction. With these characteristics, Field of View (FOV) covered 16 mm in z-direction and 32 mm in y-direction, which was modelled using 2048 pixels in the MPI simulator. Two different scanning trajectories, Lissajous and Cartesian Trajectory were used for data acquisition. System matrix reconstruction method was used for image reconstruction in both time and frequency domain using both trajectories. In the frequency domain case, noise dominated frequency components were not used for image reconstruction. Cartesian Trajectory was obtained by defining Drive field frequencies in z and y direction as, $f_z = 2.525kHz$ and $f_y = 126.250kHz$. And in case of the Lissajous Trajectory, the Drive field frequency in z and y directions were set to be $f_z = 25.25kHz$ and $f_y = 25.51kHz$ respectively.

4.1.1 System Matrix Analysis

In total, four different system matrices (time and frequency domain for both Lissajous and Cartesian trajectories) were obtained for image reconstruction, and were analyzed in terms of their condition numbers, energy distributions, singular values and spatial frequencies.

For the spatial sensitivity distributions, resolution increases with increasing harmonic frequency. Nevertheless, the signal power decreases with increasing harmonic number. In practice, beyond a certain frequency point noise dominates over the signal. Conventionally MPI systems use frequency domain data with truncating the frequency components that does not carry information for image reconstruction. This provides computational efficiency to handle the data allowing real time image reconstruction. Generally, SVD is applied on the frequency domain data, and components below a determined threshold is not used.

The image basis vectors that were obtained by the SVD analysis were examined. Each pixel was distinguishable for the noise free case, since each frequency component carries useful information. Especially, the frequencies between the harmonics carry high resolution information. The amplitude of these components are very small and practically dominated by noise. Consequently, a decrease both in the resolution and PSNR values of the reconstructed images are observed for noise-added cases.

The condition number was found to be the smallest for the time domain Lissajous trajectory case, which is 30.38 and highest for the frequency domain Cartesian trajectory case, which is 6.855×10^5 meaning that the system matrix was more ill-conditioned in the latter one. First reason for this result is the characteristic of the Cartesian trajectory that the scanning frequency in one direction is very much lower than in the other direction. Since inductive coil receive coils were used for data acquisition, induced signal level is smaller in the low frequency direction. Second reason is that time domain data preserves all information in the received signal, exhibiting a smaller condition number compared to the frequency domain case that omits noisy frequency components.

4.1.2 Image Reconstruction Analysis

Three different techniques were used for image reconstruction: Algebraic Reconstruction Technique (ART), Selective Singular Value Decomposition (SSVD), and Truncated Singular Value Decomposition (TSVD). The reconstructed images by scanning a Lissajous trajectory had larger Peak Signal-to-Noise Ratio (PSNR) values than the resultant images that used Cartesian trajectory scanning. This result is expected since Lissajous trajectory yields smaller system matrix condition number compared to the Cartesian trajectory. SSVD and TSVD methods provided better image reconstruction results compared to ART with similar PSNR values. For 34 dB data SNR, image PNSR was calculated as 8.07, 17.21, and 17.42 for ART, SSVD, and TSVD, respectively. SVD analysis and the use of largest SV components is, therefore, an essential step for MPI image reconstruction. It can be concluded that SSVD or TSVD reconstruction is preferable over ART reconstruction, and Lissajous trajectory should be preferred over Cartesian trajectory. These results are consistent with the previous studies in the MPI literature [2].

4.2 Thermal Simulations

To obtain the resultant temperature distribution after FUS sonication, Penne's Bioheat Equations were solved using the three-dimensional FDTD method. The simulator was implemented in MATLAB. A healthy, homogeneous breast fat tissue model was used as the medium where heat transfer occurred. The breast tissue density, specific heat, and thermal conductivity; blood specific heat, perfusion rate, arterial blood temperature, and metabolic heat parameters were input parameters of the simulator. A focused ultrasound beam was used as the external heat source in the model, since the motivation of temperature estimation in this thesis study is to track the temperature for the HMMDI method. The heat generated by the focused ultrasound beam power was calculated using an intensity data that is measured and recorded in Electrical and Electronics Faculty laboratories at Middle East Technical University [9]. The initial value for the medium temperature, for each pixel in FOV was defined as 310 K, just before the focused ultrasound excitation. Dirichlet boundary conditions with

310 K were used for the numerical boundary truncation. The results showing the temperature distribution for different durations of focused ultrasound heating were analyzed. 0.015, 0.8, 2.5, and 3 K peak temperature rise was obtained for a continuous FUS excitation duration of 0.01, 0.5, 1.5, and 2 seconds, respectively. The peak FUS intensity in these simulations were $2.8 \times 10^4 W/m^2$. The resultant temperature distributions were consistent with the applied FUS intensity.

4.3 Novel MPI Temperature Imaging Methods

In this thesis, two different methods were proposed for temperature imaging using MNPs. The methods were applied only for noise free case and uniform particle distribution inside the FOV.

4.3.1 Pixel - Wise Linear Scanning (PWLS)

In the PWLS method, firstly, a 1-D calibration curve from linear single pixel MPI scans is obtained. The FFR is scanned over each pixel and the calibration curve is used to estimate the temperature inside each pixel. To demonstrate our hypothesis, we first generated calibration curves for drive fields frequencies 5 kHz, 10 kHz, and 20 kHz, and drive field amplitudes between 1 mT and 5 mT. The curves were obtained by dividing the amplitude ratio of 5^{th} and 3^{rd} harmonics in the temperature range between 310 K and 320 K. The slopes of the curves were calculated to select the drive field parameters for best temperature sensitivity. The frequency did not change the calibration curve slope. Noting that the sole temperature dependence in our MPI signal model is Langevin function, this is an expected result. In practice, magnetic particles respond to an external magnetic field by Neel and Brownian relaxation mechanisms that depend on drive frequency and temperature. These effects were not taken into account in the scope of this thesis. The highest slope was achieved for 1 mT drive field amplitude. Resultantly, in the simulations, drive field with 20 kHz frequency and 1 mT amplitude in the y-direction, and 2 T/m Selection field in the z-direction was used. For the noise free case, temperature estimation results had 0.01 K resolution and the maximum relative error was calculated as 0.003 %. The effect

of noise on both calibration measurements and temperature estimation was analyzed. To obtain a reliable calibration curve, more than 60 dB SNR was required, to have an error smaller than 1% compared to the noise free case. In order to comment on the required SNR for accurate temperature estimation, difference in the signal spectrum was analyzed for a 1 K increase in temperature. The signal levels at the 3rd and 5th harmonics changed about -40 dB. Therefore, assuming a 10 dB margin for accurate temperature estimation, SNR values larger than 50 dB is required at these frequency components. Single pixel temperature scans with different noise levels were also in agreement with this result. We obtained 1.782, 0.033, and 0.0075 % maximum temperature estimation errors for 40, 60 and 80 dB SNR levels, respectively.

4.3.2 Model Based Linearization (MBL)

In the MBL method, a linear relation between the temperature and the recorded magnetization signal is obtained by using Taylor Series Expansion of the MPI signal model. The signal equation is expanded around 310 K, and high order terms are discarded. A linear equation system is obtained. The temperature changes in all pixels can be obtained by solving this equation. This method requires the system matrix as in conventional MPI. MPI data is acquired at the initial body temperature. Then, the standard MPI imaging procedure is run, revealing the MNP distribution inside the field of view. The MPI data is acquired again, after FUS excitation. Using the first and second acquisitions and the MNP distribution, temperature variations in all pixels can be solved.

Although this method can be applied for the same trajectory of the PWLS method (1-D, single pixel scan), we used a Lissajous scan trajectory to cover a 16 mm x 32 mm FOV with uniform particle distribution. Drive field amplitude was 20 mT both in z and y direction with frequencies 25.25 kHz and 25.51 kHz, respectively. Selection field was 2.5 T/m in the z-direction. The assumptions on relaxation in the PWLS method is also valid in this study. For the noise free case, MBL method provided results with 0.001 K resolution, and the maximum relative error was calculated as 0.063%. The effect of noise on temperature estimation was analyzed. Maximum temperature estimation error in the FOV errors for Temperature scans with different

noise levels were in agreement with this result. We obtained 11.5, 0.98, and 0.07 % maximum temperature estimation error inside the FOV for 40, 60, and 80 dB SNR levels, respectively.

4.4 Future Work

Relaxation is an important characteristic of the MNP behavior that also depends on the temperature. Particles suffer from Néel and Brownian relaxation effects, which means that the particles react on a field variation only after a certain amount of time. This puts a limit on the applicable frequency of the applied oscillating magnetic field and, in turn, the signal-to-noise ratio (SNR) of the measurement signal [2]. Although this effect may be negligible for the case when the Drive field frequency is small enough and the magnetization can follow the change in applied field, this effect was not included in this thesis study. In addition, MPI simulator also ignored MNP relaxation behavior. Consequently, this effect should be included in further studies.

In this study, we assumed a uniform MNP distribution in the temperature estimation analyses with FUS application. Proposed methods should be analyzed for realistic MNP distributions in the future studies.

Although we used a large Lissajous trajectory, MBL method can also be used for other trajectories such as the one in PWLS. Therefore, the performance of the MBL method should be further analyzed for other trajectories and FOV sizes.

An experimental study should also be done in order to analyze the limitations of the temperature estimation methods experimentally. By establishing an experimental setup, the relaxation effect can be examined under different ambient temperatures. To this end, tissue mimicking phantoms that mimic the electrical and thermal properties of the body can be developed. Using a heat source, a temperature distribution inside the phantom can be generated. This distribution can be measured using temperature probes. MPI and temperature distribution reconstruction methods can be applied and compared with the measurements from the probes. Noise equivalent temperature differences can be determined using these measurements.

REFERENCES

- [1] C. B. Top, A. K. Tafreshi, and N. G. Gençer, “Harmonic motion microwave doppler imaging method for breast tumor detection,” in *2014 36th Annual International Conference of the IEEE Engineering in Medicine and Biology Society*, pp. 6072–6075, Aug 2014.
- [2] T. Knopp and T. Buzug, *Magnetic Particle Imaging: An Introduction to Imaging Principles and Scanner Instrumentation*. Springer Berlin Heidelberg, 2012.
- [3] X. Chen, M. Graeser, A. Behrends, A. von Gladiss, and T. Buzug, “First measurement and snr results of a 3d magnetic particle spectrometer,” *International Journal on Magnetic Particle Imaging*, vol. 4, no. 1, 2018.
- [4] R. Habash, R. Bansal, D. Krewski, and H. T Alhafid, “Thermal therapy, part 2: Hyperthermia techniques,” *Critical reviews in biomedical engineering*, vol. 34, pp. 491–542, 02 2006.
- [5] M. Lewis, R. Staruch, and R. Chopra, “Thermometry and ablation monitoring with ultrasound,” *International Journal of Hyperthermia*, vol. 31, pp. 1–19, 03 2015.
- [6] F. Fani, E. Schena, P. Saccomandi, and S. Silvestri, “Ct-based thermometry: An overview,” *International Journal of Hyperthermia*, vol. 30, no. 4, pp. 219–227, 2014.
- [7] V. Salgaonkar, S. Datta, C. Holland, and T. D. Mast, “Passive cavitation imaging with ultrasound arrays,” *The Journal of the Acoustical Society of America*, vol. 126, pp. 3071–83, 12 2009.
- [8] B. Gleich and J. Weizenecker, “Tomographic imaging using the nonlinear response of magnetic particles,” *Nature*, vol. 435, pp. 1214–7, 07 2005.
- [9] C. Top and N. Gencer, “Harmonic motion microwave doppler imaging: A simu-

- lation study using a simple breast model,” *IEEE transactions on medical imaging*, vol. 33, 10 2013.
- [10] P. W. Goodwill and S. M. Conolly, “The x-space formulation of the magnetic particle imaging process: 1-d signal, resolution, bandwidth, snr, sar, and magnetostimulation,” *IEEE Transactions on Medical Imaging*, vol. 29, pp. 1851–1859, Nov 2010.
- [11] E. Saritas, P. W Goodwill, L. R Croft, J. J Konkle, K. Lu, B. Zheng, and S. M Conolly, “Magnetic particle imaging (mpi) for nmr and mri researchers,” *Journal of magnetic resonance (San Diego, Calif. : 1997)*, vol. 229, 12 2012.
- [12] J. Weizenecker, J. Borgert, and B. Gleich, “A simulation study on the resolution and sensitivity of magnetic particle imaging,” *Physics in Medicine and Biology*, vol. 52, pp. 6363–6374, oct 2007.
- [13] MATLAB, *version 8.5.0 (R2015a)*. Natick, Massachusetts: The MathWorks Inc., 2015.
- [14] G. H. Golub and C. Reinsch, *Singular Value Decomposition and Least Squares Solutions*, pp. 134–151. Berlin, Heidelberg: Springer Berlin Heidelberg, 1971.
- [15] A. Pyzara, B. Bylina, and J. Bylina, “The influence of a matrix condition number on iterative methods’ convergence,” pp. 459–464, 01 2011.
- [16] P. W. Goodwill, “Narrowband and x-space magnetic particle imaging,” 2010.
- [17] P. W. Goodwill and S. M. Conolly, “Multidimensional x-space magnetic particle imaging,” *IEEE Transactions on Medical Imaging*, vol. 30, pp. 1581–1590, Sep. 2011.
- [18] R. Gordon, R. Bender, and G. T. Herman, “Algebraic reconstruction techniques (art) for three-dimensional electron microscopy and x-ray photography,” *Journal of Theoretical Biology*, vol. 29, no. 3, pp. 471 – 481, 1970.
- [19] R. Gordon, “A tutorial on art (algebraic reconstruction techniques),” *Nuclear Science, IEEE Transactions on*, vol. 21, pp. 78–93, 06 1974.
- [20] R. Sznajder, K. Algorithm, R. Jeszcze, and O. Kaczmarza, “Kaczmarz algorithm revisited,” *Technical Transactions*, vol. 2, pp. 247–254, 04 2016.

- [21] P. C. Hansen, *Discrete Inverse Problems: Insight and Algorithms*. Philadelphia, PA, USA: Society for Industrial and Applied Mathematics, 2010.
- [22] H. H. Pennes, “Analysis of tissue and arterial blood temperatures in the resting human forearm.,” *Journal of applied physiology*, vol. 1 2, pp. 93–122, 1948.
- [23] E. Wissler, “Pennes’ 1948 paper revisited.,” *Journal of applied physiology*, vol. 85 1, pp. 35–41, 1998.
- [24] F. Carlak, N. Gencer, and C. Besikci, “Simulations of electrically stimulated thermal imaging using a 3d breast model,” 01 2010.
- [25] H. F. Carlak, N. G. Gençer, and C. Beşikçi, “Medical thermal imaging of electrically stimulated woman breast: A simulation study,” in *2011 Annual International Conference of the IEEE Engineering in Medicine and Biology Society*, pp. 4905–4908, Aug 2011.
- [26] J. JB Weaver, A. M Rauwerdink, and E. Hansen, “Magnetic nanoparticle temperature estimation,” *Medical physics*, vol. 36, pp. 1822–9, 06 2009.
- [27] *Taylor expansions and applications*, pp. 223–255. Milano: Springer Milan, 2008.
- [28] L. R. Croft, P. W. Goodwill, and S. M. Conolly, “Relaxation in x-space magnetic particle imaging,” *IEEE Transactions on Medical Imaging*, vol. 31, pp. 2335–2342, Dec 2012.